NAVAL POSTGRADUATE SCHOOL

MONTEREY, CALIFORNIA

THESIS

INVESTIGATION OF AN EXPLICITLY MODELED SOLID OCEAN FLOOR ON A SHALLOW WATER UNDEX EVENT

by

Adam P. Walters

September 2011

Thesis Advisor:	Young W. Kwon
Co-Advisor:	Jarema M. Didoszak

Approved for public release; distribution is unlimited

THIS PAGE INTENTIONALLY LEFT BLANK

REPORT DOCUMENTATION PAGE		Form Approved OMB No. 0704-0188

1. AGENCY USE ONLY *(Leave blank)*	2. REPORT DATE	3. REPORT TYPE AND DATES COVERED
	September 2011	Master's Thesis

4. TITLE AND SUBTITLE Investigation of an Explicitly Modeled Solid Ocean Floor on a Shallow Water UNDEX Event	5. FUNDING NUMBERS
6. AUTHOR(S) Adam P. Walters	
7. PERFORMING ORGANIZATION NAME(S) AND ADDRESS(ES) Naval Postgraduate School Monterey, CA 93943-5000	8. PERFORMING ORGANIZATION REPORT NUMBER
9. SPONSORING /MONITORING AGENCY NAME(S) AND ADDRESS(ES) N/A	10. SPONSORING/MONITORING AGENCY REPORT NUMBER

11. SUPPLEMENTARY NOTES The views expressed in this thesis are those of the author and do not reflect the official policy or position of the Department of Defense or the U.S. Government. IRB Protocol number _____NA_____.

12a. DISTRIBUTION / AVAILABILITY STATEMENT	12b. DISTRIBUTION CODE
Approved for public release; distribution is unlimited	A

13. ABSTRACT (maximum 200 words)

Current practices for modeling the ocean floor in underwater explosion simulations call for application of an inviscid fluid with soil properties. A method for modeling the ocean floor as a Lagrangian solid, vice an Eulerian fluid, was developed in order to determine its effects on underwater explosions in shallow water using the DYSMAS solver. The Lagrangian solid bottom model utilized transmitting boundary segments, exterior nodal forces acting as constraints, and the application of prestress to minimize any distortions into the fluid domain. Elastic materials were used, though multiple constitutive soil models can be applied to improve the accuracy. This method is unable to account for soil cratering effects, however it provides the distinct advantage of modeling contoured ocean floors such as dredged channels and sloped bottoms absent in Eulerian formulations. The dynamic loading effects of the investigated bottom contours were found to be negligible in the analyzed cases as a result of the bulk cavitation zone which dominates the chosen fluid field and serves as a buffer to the target. In addition to its utility in bottom modeling, implementation of the non-reflecting boundary along with realistic material models can be used to drastically reduce the size of current fluid domains.

14. SUBJECT TERMS Underwater Explosion, Shallow Water, DYSMAS, Dyna_N(3D), Gemini, Ocean Bottom Modeling, Transmitting Boundary	15. NUMBER OF PAGES 134
	16. PRICE CODE

17. SECURITY CLASSIFICATION OF REPORT	18. SECURITY CLASSIFICATION OF THIS PAGE	19. SECURITY CLASSIFICATION OF ABSTRACT	20. LIMITATION OF ABSTRACT
Unclassified	Unclassified	Unclassified	UU

NSN 7540-01-280-5500 Standard Form 298 (Rev. 2-89)
Prescribed by ANSI Std. 239-18

THIS PAGE INTENTIONALLY LEFT BLANK

Approved for public release; distribution is unlimited

INVESTIGATION OF AN EXPLICITLY MODELED SOLID OCEAN FLOOR ON A SHALLOW WATER UNDEX EVENT

Adam P. Walters
Lieutenant, United States Navy
B.S., Purdue University, 2005

Submitted in partial fulfillment of the
requirements for the degree of

MASTER OF SCIENCE IN MECHANICAL ENGINEERING

from the

NAVAL POSTGRADUATE SCHOOL
September 2011

Author: Adam P. Walters

Approved by: Young W. Kwon
Thesis Advisor

Jarema M. Didoszak
Co-Advisor

Knox T. Millsaps
Chair, Department of Mechanical and
Aerospace Engineering

THIS PAGE INTENTIONALLY LEFT BLANK

ABSTRACT

Current practices for modeling the ocean floor in underwater explosion simulations call for application of an inviscid fluid with soil properties. A method for modeling the ocean floor as a Lagrangian solid, vice an Eulerian fluid, was developed in order to determine its effects on underwater explosions in shallow water using the DYSMAS solver. The Lagrangian solid bottom model utilized transmitting boundary segments, exterior nodal forces acting as constraints, and the application of prestress to minimize any distortions into the fluid domain. Elastic materials were used, though multiple constitutive soil models can be applied to improve the accuracy. This method is unable to account for soil cratering effects, however it provides the distinct advantage of modeling contoured ocean floors such as dredged channels and sloped bottoms absent in Eulerian formulations. The dynamic loading effects of the investigated bottom contours were found to be negligible in the analyzed cases as a result of the bulk cavitation zone which dominates the chosen fluid field and serves as a buffer to the target. In addition to its utility in bottom modeling, implementation of the non-reflecting boundary along with realistic material models can be used to drastically reduce the size of current fluid domains.

THIS PAGE INTENTIONALLY LEFT BLANK

TABLE OF CONTENTS

THIS PAGE INTENTIONALLY LEFT BLANK

LIST OF FIGURES

LIST OF TABLES

THIS PAGE INTENTIONALLY LEFT BLANK

LIST OF ACRONYMS AND ABBREVIATIONS

DYSMAS – Dynamic System Mechanics Advanced Simulation

EOS – Equation of States

FSI – Fluid-Structure Interface

FSP – Floating Shock Platform

IABG - Industrieanlagen-Betriegsgesellschaft mbH

NRB – Nonreflecting Boundary

NSWC – Naval Surface Warfare Center

SCI – Standard Coupler Interface

SWI – Singly-Wetted Interface

TNT – Trinitrotoluene

UNDEX - Underwater Explosion

THIS PAGE INTENTIONALLY LEFT BLANK

ACKNOWLEDGMENTS

I would like to first thank my wife, Sarah. Without her love, support, and patience, I would never have completed a fraction of this thesis.

From the Naval Postgraduate School's Shock and Vibration Computational Laboratory, Professor Jarema Didoszak's personal enthusiasm in the field of Underwater Explosion research provided the guidance and inspiration I needed to complete this research.

From the Naval Postgraduate School's Mechanical Engineering Department, Professor Young Kwon's encouragement and fundamentals based approach to research helped to keep me focused during the more challenging aspects of my research.

From NSWC Indian Head, the technical expertise and vast experience in the field of Underwater Explosions research and the DYSMAS software of Mr. Roger Ilamni and Mr. Reid McKeown were absolutely critical during the development of a method of Lagrangian solid bottom modeling which the software was not originally designed to accommodate.

Mr. Roman Koltinuik of the United States Bureau of Reclamation and Mr. Jerry Lin of Lawrence-Livermore National Laboratory provided essential methodology, which was required to fully realize the Lagrangian solid bottom modeling method that was developed in this research.

THIS PAGE INTENTIONALLY LEFT BLANK

I. INTRODUCTION

A. BACKGROUND

Research into the phenomena of underwater explosions (UNDEX) and their effects on ship structure and equipment was conducted in earnest following World War II. The motivation was that numerous ships experienced extensive damage not only from direct hits, but also from near misses during the war. The foundation of the field of study is based in the works of Arons [1], Cole [2], Snay [3], and Taylor [4]. These researchers provided extensive theoretical and empirical relationships describing the various phenomena of underwater explosions. Their research led to the development of shock design and testing parameters by the U.S. Navy. The most recent set of these requirements are delineated in MIL-S-901D [5], NAVSEA 0908-LP-000-3010A [6], and OPNAVINST 9072.2 [7].

With the growth in high performance computing power and rising costs of live-fire testing for full ship shock trials, the U.S. Navy has pushed for the development of computer simulation techniques to supplement and enhance the shock testing of new platforms. Working in conjunction with a German Defense Contractor, Industrieanlagen-Betriegsgesellschaft mbH (IABG), and Lawrence-Livermore National Laboratory the U.S. Navy developed, fielded, and validated the Dynamic System Mechanics Advanced Simulation (DYSMAS) hydrocode to model the fully-coupled, fluid-structure interaction problem of an UNDEX event on a ship.

The recent focus on naval operations in littoral waters, coupled with the delivery of the Littoral Combat

Ship (LCS), presents unique challenges to the field of shock testing and simulation. As nearly all UNDEX testing has been conducted in deep water, the effect a shallow water environment has on the UNDEX response of a ship has not been extensively investigated. The sinking of the Ex-Lütjens in the Baltic Sea in is one of the few documented tests in littoral waters in which DYSMAS was used to simulate the UNDEX event. The simulation took into account the effect of the ocean bottom through the application of an equation of state in the fluid solver of DYSMAS, which was used to represent the bottom soil [8]. This method of bottom modeling utilizing a fluid with representative properties and behavior of soils has been thoroughly tested and validated [9], [10], [11].

B. SCOPE OF RESEARCH

At its most fundamental level, the accepted bottom modeling method used in DYSMAS treats the soil as an inviscid fluid. This research will develop an alternative approach that utilizes the structural solver of DYSMAS to model the bottom as a solid, finite element structure. This Lagrangian solid bottom modeling approach will be compared to the current bottom modeling technique to determine its validity and potential benefits. The Lagrangian solid bottom modeling method provides the capability to model contoured bottom profiles, while the current method can only create horizontal surfaces. A parametric study of this capability will be conducted to determine the effect that contoured bottom profiles have on the response of a ship subjected to an UNDEX event in littoral waters.

II. UNDERWATER EXPLOSION THEORY

A. SHOCKWAVE OF INITIAL EXPLOSION

The first of two major aspects of an underwater explosion (UNDEX) is the high pressure "shock" wave caused by the detonation of a high explosive, such as trinitrotoluene (TNT). In the case of TNT, the pressure difference between the explosive and the surrounding water is on the order of 2×10^6 psi (≈15 GPa). This large pressure difference causes the water to compress and the wave initially propagates approximately five times faster than the acoustic speed in water (≈5,000 ft/sec). The pressure wave as a function of time passing through an arbitrary point is steep-fronted, with a backside that decays exponentially over a few milliseconds.

1. Acoustic Wave Assumption

The initial wave velocity can be five times larger than the acoustic speed. Researchers have shown that the wave quickly slows to acoustic speed as the wave front pressure difference decreases radially outward. Therefore the shockwaves are approximated as acoustic plane waves with small compressions and speeds. This assumption allows the derivation of the Equation (2.1), which relates added fluid pressure (P) from the shockwave to the wave velocity (u) [2].

$$P = \rho_o C_o u \tag{2.1}$$

The mass density (ρ_o) and the acoustic wave speed (C_o) of the fluid are assumed to be constant properties. This

relationship assumes the fluid is uniform, compressible, and nonviscous. The acoustic wave assumption validation is demonstrated in Figure 1.

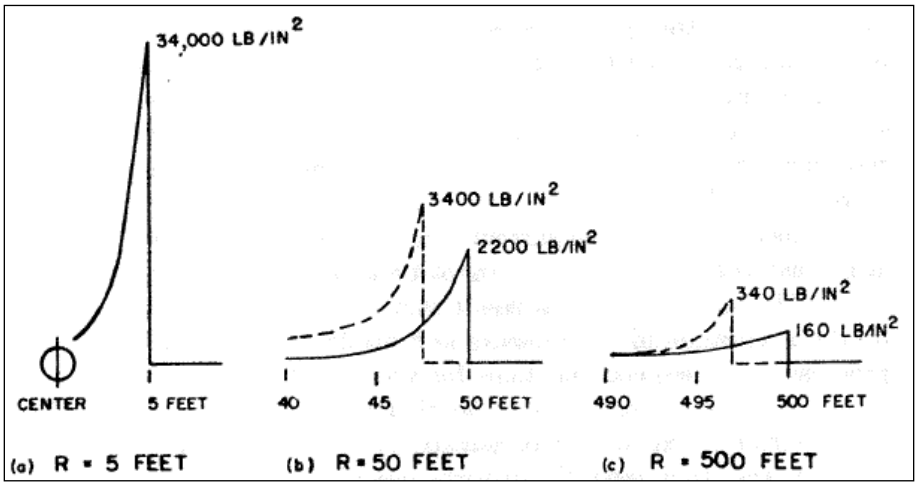

Figure 1. Shock Wave Pressure Distribution of 300 lbf TNT Charge at Three Times. From [2]

Figure 1 shows the magnitude of the pressure wave as it passes through three distances (R) from the epicenter of the explosion. The solid lines represent the empirical shockwave values. The dashed lines, which lag the shock wave by less than five feet in Figures 1(b) and 1(c), are the acoustic approximations taken at the same time as the associated solid line shockwave. With the acoustic speed in water at five feet per millisecond, it is thus safe to make the acoustic wave assumption. Cole has shown this approximation to be valid for radii from the charge that are between 10 and 100 times the radius of the charge.

2. Behavior at Interfaces

Shockwave behavior at an interface such as the water-seabed or the air-water is governed by a combination of Snell's law and the continuity of pressure and velocity at

the interface. An arbitrary fluid interface is diagramed in Figure 2 and will be the basis of the equations that follow.

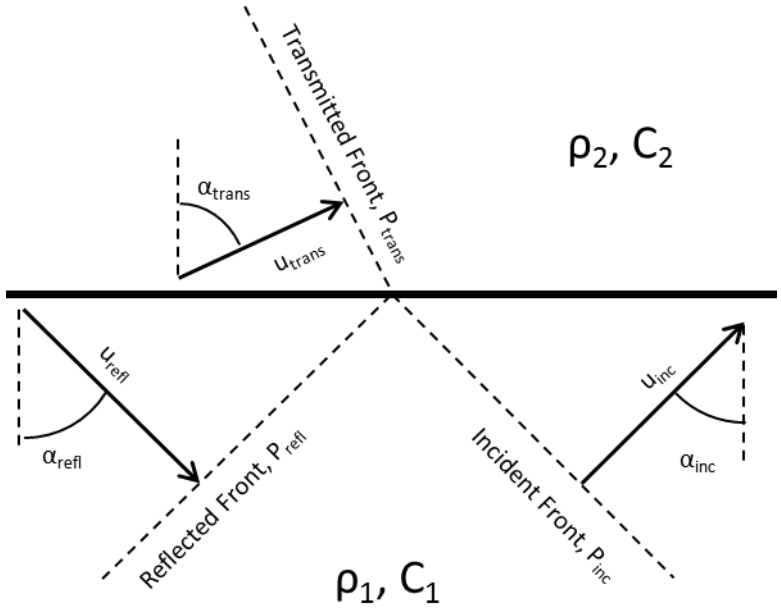

Figure 2. Arbitrary Interface Geometry

Snell's Law demonstrates the relationship of each medium's acoustic wave speed (C) and each wave's angle of incidence with reference to a normal vector of the interface (α) to one another.

$$\frac{C_1}{\sin \alpha_{inc}} = \frac{C_1}{\sin \alpha_{refl}} = \frac{C_2}{\sin \alpha_{trans}} \tag{2.2}$$

Applying continuity of pressure and velocity, along with Equations (2.1) and (2.2), to the interface yields the following relationship between the pressure and velocity of the incident, reflected, and transmitted shockwaves.

$$\frac{P_{refl}}{P_{inc}} = \frac{\rho_2 C_2 \cos \alpha_{inc} - \rho_1 C_1 \cos \alpha_{trans}}{\rho_2 C_2 \cos \alpha_{inc} + \rho_1 C_1 \cos \alpha_{trans}} = \frac{u_{refl}}{u_{inc}} \tag{2.3}$$

$$\frac{P_{trans}}{P_{inc}} = \frac{2\rho_2 C_2 \cos \alpha_{inc}}{\rho_2 C_2 \cos \alpha_{inc} + \rho_1 C_1 \cos \alpha_{trans}} = \frac{\rho_2 C_2}{\rho_1 C_1} \frac{u_{trans}}{u_{inc}} \tag{2.4}$$

Applying these relationships at a rigid boundary ($\rho_2 C_2 >> \rho_1 C_1$) yields a compressive wave reflection with the magnitudes of both the incident and reflected waves pressure and velocity being equal. By definition the velocity of a rigid boundary is zero.

Alternatively, the shockwave behavior at a free surface, such as the air-water interface, ($\rho_2 C_2 << \rho_1 C_1$) causes the creation of a tensile reflection or rarefaction wave. It is referred to as a tensile wave because Equation (2.3) gives the result that P_{refl} equals the negative of P_{inc}. The subsequent interactions of the incident (compressive) and rarefaction (tensile) waves can lead to the phenomenon of bulk cavitation, which will be further discussed later in this chapter. Whether or not bulk cavitation occurs, the passage of a compressive and tensile wave through a point at different times causes a unique effect called the pressure cutoff. This effect is demonstrated in the pressure-time history in Figure 3. The time between the passing of the two waves is called the cut-off time. The net effect of the cut-off on a point is an abrupt halt to the impulse on a structure at that point. Figure 4 provides a visual depiction of the UNDEX environment with its associated waves.

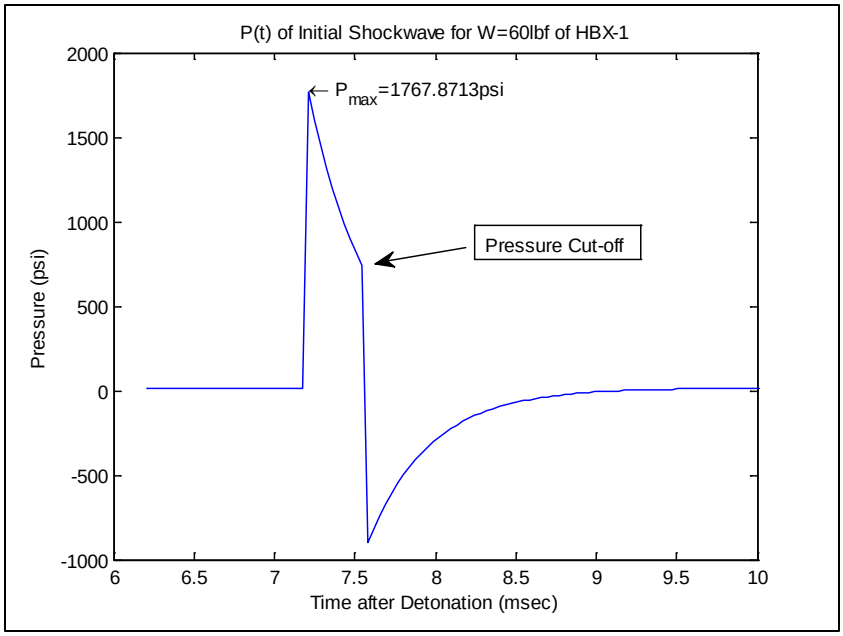

Figure 3. MATLAB Figure of Pressure History

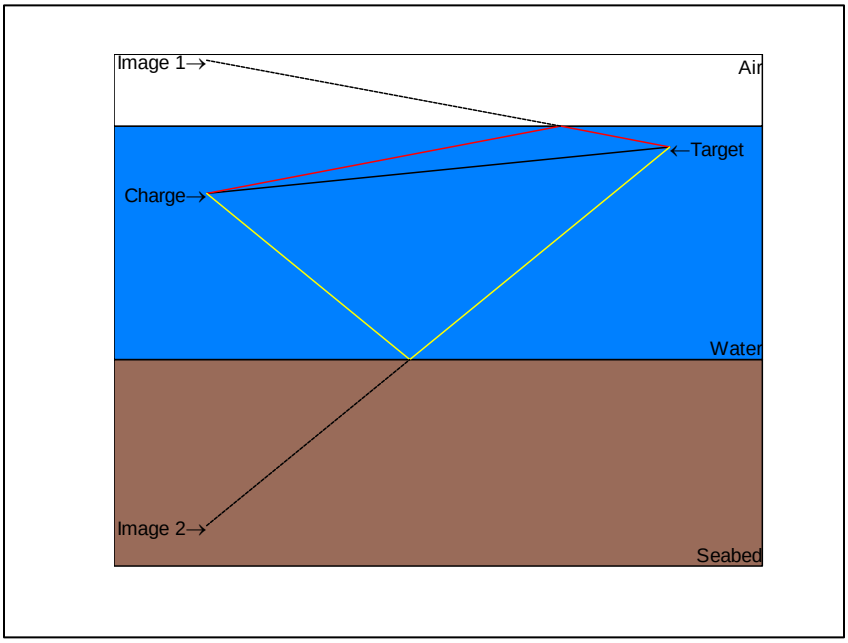

Figure 4. UNDEX Geometry

3. Empirical Formulas

Empirical formulas to approximate several important properties of UNDEX events have been developed by Cole and others. These equations were fit from the interdependence of charge weight (W) in pounds and wave propagation distance (R) in feet for a spherical charge. The two most important formulas are for the peak pressure (P_{max}) in pounds per square inch (psi) and the decay constant (θ) in milliseconds. K_1, A_1, K_2, and A_2 are experimental constants, which depend on the explosive material type [2].

$$P_{\max} = K_1 \left(\frac{W^{1/3}}{R} \right)^{A_1} \tag{2.5}$$

$$\theta = K_2 W^{1/3} \left(\frac{W^{1/3}}{R} \right)^{A_2} \tag{2.6}$$

B. GAS BUBBLE

After the emission of the shockwave, the remains of the exploded and unexploded gas are contained within a high pressure gas bubble whose behavior dominates the fluid environment following the dissipation of the initial shock wave.

1. Bubble Motion

With the pressure of the bubble much greater than the surrounding hydrostatic pressure, the bubble expands rapidly in a roughly spherical shape. The expansion continues past the point at which bubble pressure equals the hydrostatic pressure. This is due to the outward momentum of the water. Once the bubble reaches its maximum size, the surrounding water pressure begins to collapse the bubble. At a certain point, the gas products inside the

bubble are compressed to the point of igniting the unexploded gas. This second explosion emits a shockwave known as the first bubble pulse. This process of expansion and contraction continues until the energy of the bubble is expended or the bubble "vents" to the atmosphere.

Buoyancy and drag forces act upon an oscillating bubble as it rises in the water. The speed at which the bubble rises is inversely proportional to the bubble's diameter. When the bubble diameter is at a maximum the drag surface area is at its maximum. When the bubble contracts its vertical velocity increases until it begins to expand again. While it is apparent that due to the gas' buoyancy the bubble must rise, the proximity to underwater structures can significantly impair this movement [3]. Figure 5 details the timing relationship between bubble size and pulses.

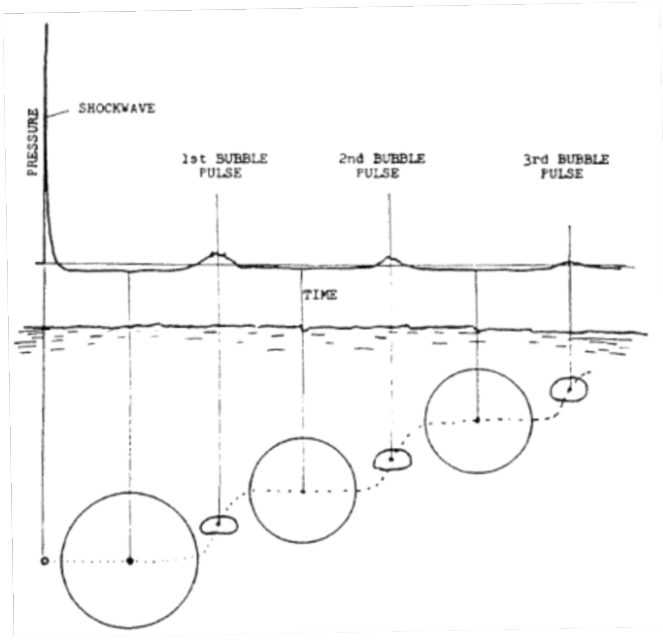

Figure 5. Bubble Phenomena of UNDEX. From [3]

2. Bubble Effects

The two major effects of the bubble on ships are follow-on pulses and the inducement of hull whipping. Hull whipping occurs when the period of the bubble pulse coincides with the ship's lowest natural frequency. The effect of the pulse shockwaves is significantly lower than that of the initial explosion. Figure 6 is a summary of Aron's energy partition of an UNDEX event. Within the percentage for each shockwave, roughly half is imparted as the acoustic wave. The remainder is spent through flow dissipation and other losses [1].

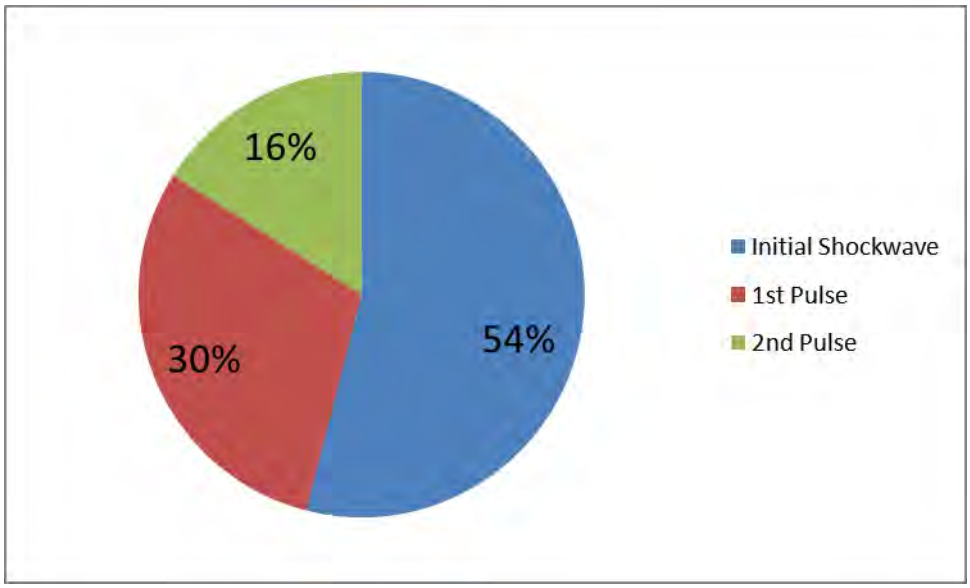

Figure 6. Energy Partition of Bubble Shockwaves

3. Bubble Formulas and Correction Factors

While there are various empirical methods of modeling gas bubble oscillations, this work's focus on shallow waters will limit the scope bubble analysis. In order to accurately model the extent and duration of impact the bubble will have on the simulations, an approximation of

the bubble's maximum radius and period of the first pulse is necessary. Due to the proximity of the air-water and water-seabed interfaces in shallow waters, a correction factor must be taken into account.

Following the same parameters for weight and distance as Equations (2.5) and (2.6), the maximum bubble radius (A_{max}) in feet is [2]:

$$A_{max} = K_6 \left(\frac{W}{D + 33} \right)^{1/3} \tag{2.7}$$

Equation (2.8) is used to determine the bubble period (T) in seconds with a correction factor for surface proximity. The numerical constant (α) is equal to 0.1 when A_{max}/D is less than 0.5. When A_{max}/D is greater than 0.5, then α is approximated between 0.1 and 0.2 [12].

$$T = K_5 \frac{W^{1/3}}{(D + 33)^{5/6}} \left(1 - \alpha \frac{A_{max}}{D} \right) \tag{2.8}$$

C. CAVITATION

Cavitation is the creation and subsequent collapse of vapor bubbles in a fluid, which is the result of the pressure dropping below the fluid's vapor pressure. UNDEX events provide the possibility for two distinct areas of cavitation.

1. Bulk Cavitation Zone

As discussed previously, bulk cavitation occurs when a tensile wave lowers the total pressure at a point below the vapor pressure of the fluid. The result is a random distribution of small bubble formation throughout the cavitation region. The horizontal extent of the cavitation zone is typically an order of magnitude larger than the

depth to which it extends. The bulk cavitation zone subsequently collapses or "zips up" shortly after the initial shock wave has diminished. This collapse emits a shockwave of its own, which is much less than the initial shockwave, but is noticeable in the structural response. Figure 7 depicts the radial and vertical dimensions of the bulk cavitation zone for a 60 pound charge of HBX-1 at a depth of 32.8 feet. Equations (2.9) and (2.10), along with the variables listed in Table 1, are the empirical formulas used to determine the upper and lower bounds, respectively, of the bulk cavitation zone [13].

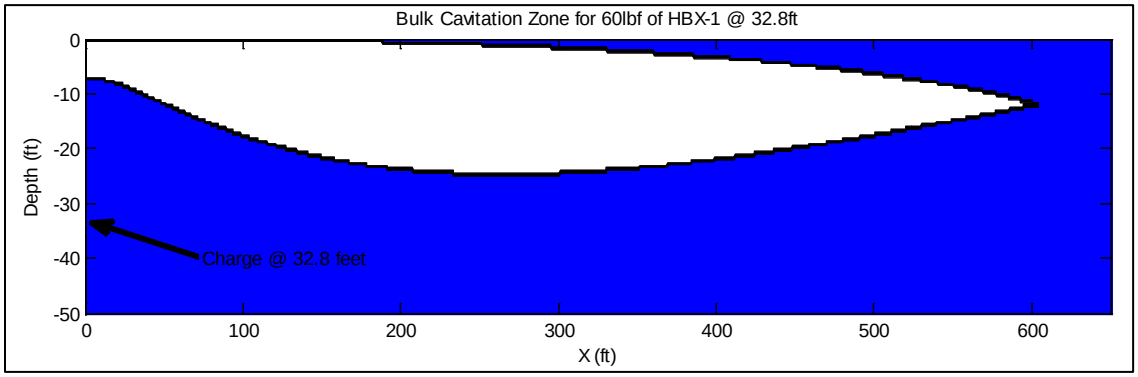

Figure 7. Bulk Cavitation Zone for 60 lbf of HBX-1

$$F(x,y) = K_1 W^{A_1/3}\left(r_1^{-A_1} e^{\frac{-(r_2-r_1)}{C\theta}} - r_2^{-A_1}\right) + P_{atm} + \gamma y \equiv 0 \qquad (2.9)$$

$$G(x,y) = \frac{P_{inc}}{C\theta}\left\{1 + \left[\frac{r_2 - 2D\left(\frac{D+y}{r_2}\right)}{r_1}\right]\left[\frac{A_2 r_2}{r_1} - A_2 - 1\right]\right\} - \frac{A_1 P_{inc}}{r_1^{\,2}}\left[r_2 - 2D\left(\frac{D+y}{r_2}\right)\right] + \gamma\left(\frac{D+y}{r_2}\right) + \frac{A_1}{r_2}\left(P_{inc} + P_a + \gamma y\right) \equiv 0 \qquad (2.10)$$

Table 1. Bulk Cavitation Variables

Symbol	Variable	Units
X	Lateral distance of position from Charge	ft
Y	Depth of position from free surface	ft
D	Depth of Charge from free surface	ft
$r_1 = \left[\left(D - y \right)^2 + x^2 \right]^{0.5}$	Path from Charge to position	ft
$r_2 = \left[\left(D + y \right)^2 + x^2 \right]^{0.5}$	Path from Image Charge to position	ft
W	Weight of Charge	lbf
C	Acoustic Velocity of Fluid	ft/msec
θ	Decay Constant from Equation (2.6)	msec
γ	Specific Weight of Fluid	lbf/ft^3
P_{inc}	Pressure of Incident Wave	lbf/ft^2
K_1, A_1, K_2, A_2	Coefficients of Charge Material	N/A

2. Local/Hull Cavitation

In addition to bulk cavitation, localized cavitation occurs in the area immediately surrounding a ship's hull. This effect is best described in its initial stages by Taylor Plate Theory.

a. Taylor Plate Theory

This theory is a 1-D examination of a fluid-plate interface in order to understand the structural response of the plate due to pressure wave impact through the water. A depiction of the interface is illustrated in Figure 8.

Equation (2.11) is the equation of motion for the plate. The primary assumption of this derivation is that the fluid-structure interface (FSI) is maintained at all times.

$$m\ddot{w}(t) + \left[b + \rho_o C_o\right]\dot{w}(t) + kw(t) = q(t) - 2P_{inc}(0, t) \qquad (2.11)$$

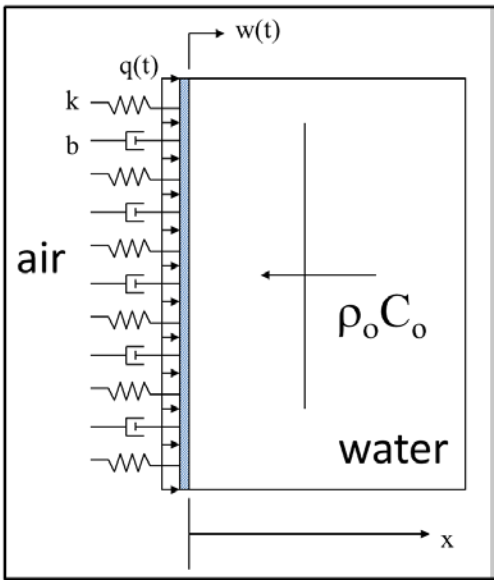

Figure 8. Taylor Plate Geometry. From [14]

b. Separation

At some time after the impact of the pressure wave, depending on the density of the plate, the plate may be moving at a speed faster than the water can maintain. These differences in speed create a tensile pull on the fluid at the FSI. At some point the pressure may drop at the FSI below vapor pressure of the fluid and local cavitation will occur.

Throughout the simulations, as the structure is vibrating, the presence of local cavitation in the areas immediately around the hull is expected. Additionally, since the intent of this research is to model the soil

bottom as a structure, which can vibrate depending on the material selected, local cavitation might be possible at the soil-water interface.

D. SHOCKWAVE-BOTTOM SEDIMENT INTERACTION

As discussed in Section II.A.2, a pressure wave incident on a rigid interface will be reflected as a compressive wave of equal pressure and speed. If the ocean bottom were assumed to be a rigid body, it would simplify the modeling requirements. However, the ocean bottom can be composed of a range of materials yielding multiple shock responses. For example, highly-porous, bottom sediment can reflect a tensile (or rarefaction) wave instead of a compressive wave [10].

The two aspects of waves in soils that have been well researched and tested are the response of dry, porous soil undergoing air-blast events and the properties of submerged, porous soil with respect to their reflection, transmission, and attenuation properties when subjected to acoustic waves at pressure levels significantly lower than UNDEX shockwaves. As a result, most available soil material models used are focused on these two aspects. The particular shortcoming is the lack of bottom sediment experimental data, which is fitted to already established material models.

1. Soil Properties

All naturally occurring soil is a three-phase system consisting of solid particles, water, and air. The solid particles form structures of varying degrees of order. The voids within this structure are filled either by air or

water. Additionally, there is a distinct difference in behavior between cohesive (clay) and non-cohesive (sand) soils [15]. In general, the tensile strength of all soils is orders of magnitude smaller than it's compressive and shear strengths [16].

2. In-Situ Stresses of Saturated Soils

The definition of a saturated soil is one in which water has filled all of the voids in the solid structure. An understanding of the static stresses in the soil is necessary in order to effectively model boundary conditions on the bottom model. The total static stress at any point in the soil column can be found by applying Equation (2.12). The equation is based upon the assumption that the water in the soil is not flowing vertically through the soil. Equation (2.12) determines the total stress (σ) at a depth below the air-water interface using the unit weights of water (γ_w) and saturated soil (γ_{sat}), the depth from the air-water interface to the water-soil interface (H), and the depth from the water-soil interface to the position of interest (H_A) [15].

$$\sigma = H\gamma_w + \left(H_A - H\right)\gamma_{sat} \tag{2.12}$$

III. MODELING AND SIMULATION USING DYSMAS

A. SOFTWARE SUITE

The software package that was used for this research is the Dynamic System Mechanics Advanced Simulation (DYSMAS) code. DYSMAS is a fully coupled, six degree-of-freedom, hydrocode that is designed to simulate three-dimensional, UNDEX events. The software consists of three major components. The Gemini software is an Eulerian solver for the fluid environment. The structural solver, Dyna_N(3D), evaluates the structural response using a Lagrange method. While several other structural solvers can be used with DYSMAS, only Dyna_N(3D) was used for this research. The final and most important component is the Standard Coupler Interface (SCI), which passes information between the two solvers at the end of each Eulerian time step to maintain the fully coupled interface.

B. GEMINI

The Gemini code is a finite-difference, Euler equation solver. It was specifically designed to simulate the UNDEX phenomena of shockwaves and bubble jetting. It is capable of solving flow fields involving several fluid types.

1. Theory

Gemini solves the fluid mesh by running a higher order Godunov method algorithm to solve the fluid domain at each time step. This algorithm is applied to each Euler cell in a one-dimensional approach through each principal direction at a time solving the Euler equations for conservation of mass, momentum, and energy. A major assumption of the Euler

equations is that the flow is frictionless or inviscid. This assumption of an inviscid fluid limits Gemini's capability to fully model a Lagrangian solid bottom as most soils can support shear loading [17].

2. Components

There are several additional components to the Gemini code. GemGrid, PreGemini, Float, and Prestress are preprocesses. GemGrid allows the user to setup up the three-dimensional, Euler cell grid. This allows for grid refinement around specific areas of interest in the flow field, specifically the fluid bubble and the ship hull. PreGemini fills the Euler cell grid with the user-defined material equations of state and their initial properties (energy, density, etc.). The Float and Prestress processes allow the user to accurately position and prestress the Dyna_N structure in the fluid domain prior to the transient analysis. Following the completion of the simulation by the Gemini solver, the postprocessing of the data is completed by GemHis and GemField. GemHis processes the recorded data at specific points of interest throughout the fluid for analysis. GemField generates contour plots of the flow field at specified times for the fluid domain and interface segments. The relationship of each Gemini component to the overall code is diagramed in Figure 9. The light blue boxes indicate the various user-defined input files that are required [18].

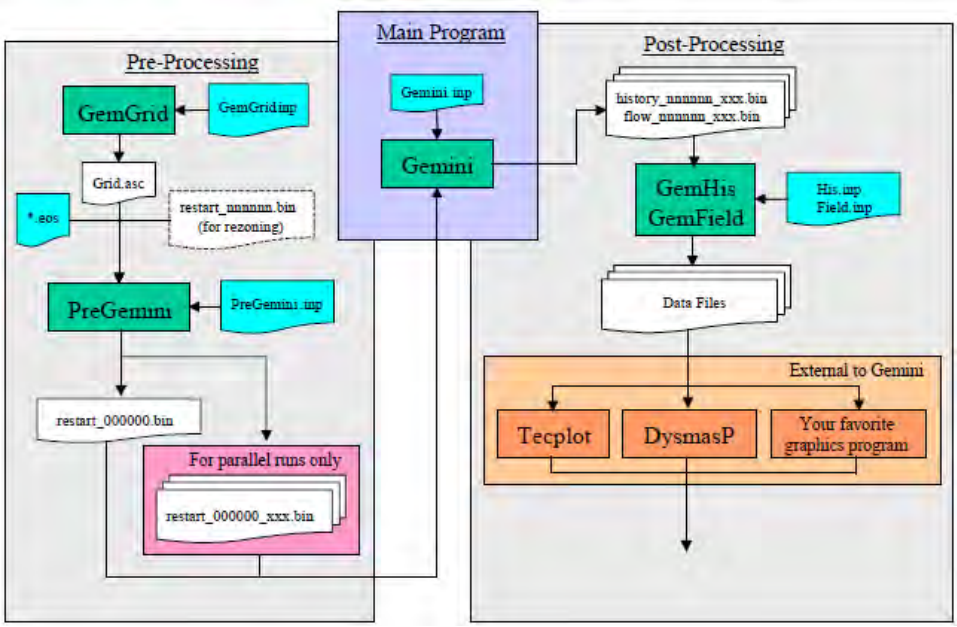

Figure 9. Gemini Data Flow Chart. From [18]

C. DYNA_N(3D)

Dyna_N is a nonlinear, explicit, three-dimensional finite element code that analyzes dynamic structural responses.

1. Theory

The software solves a discrete formulation of the linear second order differential equation of motion:

$$m\ddot{x} + c\dot{x} + kx = p(t) \tag{3.1}$$

It can also accommodate non-linearity in the structure with the following equation:

$$m\ddot{x} + c\dot{x} + f_{\text{int}} = p(t) \tag{3.2}$$

Dyna_N solves the combination of these two equations, which has a form of:

$$[M]\{\ddot{x}\} + \{F\} - \{P\} = 0 \tag{3.3}$$

where {P} represents the body forces and external loads, {x} is the displacement vector, {x''} is the acceleration vector, [M] is the structure's mass matrix, and {F} handles the internal non-linearity [19].

The solver then utilizes an explicit central differencing scheme to step through each time. The use of the explicit time step integration dictates that the solution is only stable when the time step is kept below a certain value, commonly known as the Courant number. Essentially, this means that the time step must be kept small enough to allow a wave to propagate through the space discretization. For example, if the wave speed is 5000 ft/sec and the discretized length is only one foot, the time it takes the wave to pass through the element is 0.2 milliseconds. If the time step were any larger, the wave would pass through the element without the solver having the opportunity to account for it. In the end, this means that the maximum time step is driven by the smallest element in the structure. The standard coupler interface will choose the smaller of the two time steps between Gemini and Dyna_N.

2. Pre-/Post-Processing

The preprocessing of all finite element models was done using the DYSMAS Pre-Processor 2010. The software allows for the creation of the model's structure, assignment of material properties, boundary conditions, body forces, motions, and fluid-structure interface segment definitions. The structural model is then written into the specific input cards required Dyna_N [20].

The use of the preprocessor in generating the ocean bottom structure proved problematic as it did not have the ability to define several different material models, boundary conditions, and functions that were tested. These features were present in Dyna_N, but no user-interface in the preprocessor had been created. As a result, several features of each model had to be tediously entered into the Dyna_N input cards after the preprocessor had been run.

The DYSMAS postprocessor allows the user to visualize the entire fluid-structure dynamic response. It contained features that allowed for the extraction and analysis of a wide range of response data from both the fluid domain and the structure.

D. STANDARD COUPLER INTERFACE (SCI)

The SCI is the key component in the DYSMAS software suite that allows the simulations to be fully coupled. The SCI is required because in order to pass information between the fixed Euler grid and a finite element model whose structural nodes and interfaces move. Figure 10 depicts this link as well as the type of information passed. The main functions the SCI accomplishes are [17]:

- Build a grid representation of the structural interface into the Euler mesh
- Enforce boundary conditions at the FSI
- Activate/De-activate cells as the FSI passes through the Euler mesh
- Calculate nodal loads.

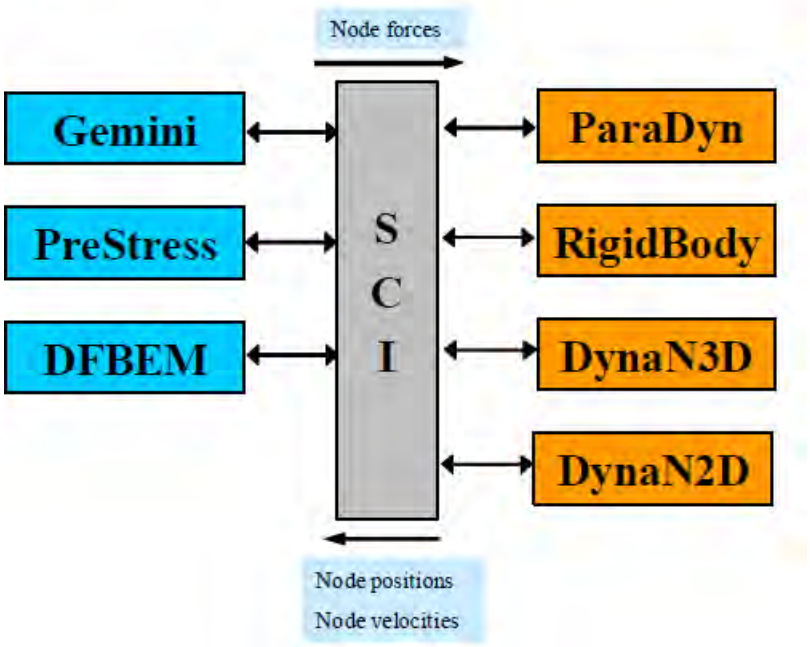

Figure 10. SCI Block Diagram. From [18]

E. BASIC DYSMAS SIMULATION SETUP

The creation of each DYSMAS simulation used in this research involved nearly all the same basic steps. These included generating the Euler grid, filling the fluid domain with the correct hydrostatic conditions, and developing the finite element model. For each of these steps several different sources of best practices were utilized as decision-making tools.

1. Euler Grid Generation

When defining the Euler grid, the most important determination was the grid refinement immediately surrounding the gas bubble and the ship structure. According to Prendergast, DYSMAS simulations are highly sensitive to the mesh size surrounding the explosion. The smaller the mesh size, the closer in accuracy the

simulation is to both empirical predictions and experimental data in maximum pressure, bubble radius, and bubble period. Additional simulations demonstrated that Gemini's free boundary conditions did not adequately allow fluid to flow out of and back into the fluid domain quickly enough if the fluid domain was too small in comparison to the maximum bubble diameter. This finding was particularly applicable to the shallow water simulations where the overall fluid depth was restricted. Based on Prendergast's findings and discussions of best practices with Didoszak, the parameters in Table 2 were used to determine the size of both the fine mesh and also overall extent of the fluid domain [21], [22].

Table 2. GemGrid Decision Matrix

2-D Mesh Size	2 cm (x,z)
3-D Fine Mesh Size	< Minimum length of smallest interface element (Default = 10cm)
Extent of Bubble Fine Mesh	> 1.71 x Max. Bubble Radius in (x,y,z)
Extent of Ship Fine Mesh	>= 100cm on each side
Distance from Charge to Fluid Boundary	= 10 x Max. Bubble Radius in (x,y)
Thickness of Air Layer	= 1,000cm

2. Fluid Domain Setup

The fluid domain was initialized through the Pregemini input file. The critical step in this procedure was the seeding of the fluid domain with the correct materials at the appropriate states. In order to simulate the different materials such as explosives, air, water, etc. Gemini utilizes various Equations of State (EOS). These EOSs are used to relate the pressure, energy, and density through the solution of the fluid environment. The EOSs used in this research are provided in Tables 3 through 7 [18].

Table 3. Gemini EOS for Air

Material:	Air			
EOS:	Gamma-Law			
Form:	$p = (\gamma - 1)\rho e$			
Properties	Cavitation Pressure	p_{cav}	0.	dynes/cm^2
	Reference Density	ρ_o	0.0013	g/cm^3
	Reference Specific Energy	e_o	1.9230769e+9	erg/g
	Speed of Sound in Cavitation Region	c_{cav}	3.28e+4	cm/s
	Minimum Density	ρ_{floor}	1.D-06	g/cm^3
	Minimum Specific Energy	e_{floor}	1.D-4	erg/g
	Gamma	γ	1.4	N/A

Table 4. Gemini EOS for HBX-1 (Unburned)

Material:	HBX-1 Unburned			
EOS:	Tait for Unburned Explosive			
Form:	$p = p_o + B\left(\left(\frac{\rho}{\rho_o}\right)^{\gamma} - 1\right)$			
Properties	Cavitation Pressure	p_{cav}	0.	dynes/cm^2
	Reference Density	ρ_o	1.720	g/cm^3
	Reference Specific Energy	e_o	6.520E+10	erg/g
	Speed of Sound in Cavitation Region	c_{cav}	4.06e+5	cm/s
	Minimum Density	ρ_{floor}	1.E-06	g/cm^3
	Minimum Specific Energy	e_{floor}	1.E-4	erg/g
	Gamma	γ	1	N/A
	Ambient Pressure	p_o	1.E+6	dynes/cm^2
	Unburned Explosive Density	ρ_o	1.72	g/cm^3
	CJ Density	ρ_{CJ}	2.25567	g/cm^3
	CJ Specific Energy	e_{CJ}	7.455692E+10	erg/g
	CJ Pressure	p_{CJ}	1.355396E+11	dynes/cm^2
	Detonation Velocity	D	5.75045E+05	cm/s
	Factor	F	0.95	N/A

Table 5. Gemini EOS for HBX-1 (Exploded)

Material:	HBX-1 (Exploded)			
EOS:	JWL			
Form:	$p = A\left(1 - \frac{\omega\rho}{R_1\rho_o}\right)e^{-R_1\frac{\rho_o}{\rho}} + B\left(1 - \frac{\omega\rho}{R_2\rho_o}\right)e^{-R_2\frac{\rho_o}{\rho}} + \omega\rho e$			
Properties	Cavitation Pressure	p_{cav}	0.	dynes/cm^2
	Reference Density	ρ_o	1.720	g/cm^3
	Reference Specific Energy	e_o	6.520E+10	erg/g
	Speed of Sound in Cavitation Region	c_{cav}	4.06e+5	cm/s
	Minimum Density	ρ_{floor}	1.E-06	g/cm^3
	Minimum Specific Energy	e_{floor}	1.E-4	erg/g
	constant	A	5.183E+12	N/A
	constant	B	4.39E+9	N/A
	constant	R_1	5.183	N/A
	constant	R_2	3.5E-1	N/A
	γ - 1	ω	0.25	N/A

Table 6. Gemini EOS for Water

Material:	Water			
EOS:	Tillotson			
Form:	$p = p_o + \omega\rho\left(e - e_o\right) + A\left(\frac{\rho}{\rho_o} - 1\right) + B\left(\frac{\rho}{\rho_o} - 1\right)^2 + C\left(\frac{\rho}{\rho_o} - 1\right)^3$			
Properties	Cavitation Pressure	p_{cav}	50000.	dynes/cm^2
	Reference Density	ρ_o	1.0	g/cm^3
	Reference Specific Energy	e_o	3.5420001E+9	erg/g
	Speed of Sound in Cavitation Region	c_{cav}	147600.0	cm/s
	Minimum Density	ρ_{floor}	9.999998E-03	g/cm^3
	Minimum Specific Energy	e_{floor}	-9.99998E+10	erg/g
	γ - 1	ω	.28000000119	N/A
	Ambient Pressure	p_o	1.E+6	dynes/cm^2
	constant	A	2.200000E+10	N/A
	constant	B	9.540000E+10	N/A
	constant	C	1.457E+11	N/A

Table 7. Gemini EOS for Clay

Material:	Clay			
EOS:	Mie-Grüneisen			
Form:	$p = \Gamma_o\rho_o\left[e - \left(e_o + \mu\frac{p_o}{\rho_o} + \frac{C_s^{\,2}}{(1 - S\mu)}Y\right)\right] + \rho_o\frac{d}{d\mu}\left(\frac{C_s^{\,2}Y}{(1 - S\mu)}\right) + p_o$ with: $\mu \equiv 1 - \frac{\rho_o}{\rho}$ and $Y = \sum_{k=0}^{5} a_k\mu^k$			
Properties	Cavitation Pressure	p_{cav}	20000.	dynes/cm^2
	Reference Density	ρ_o	2.023	g/cm^3
	Reference Specific Energy	e_o	0.	erg/g
	Speed of Sound in Cavitation Region	c_{cav}	260000.0	cm/s
	Minimum Density	ρ_{floor}	1.0E-02	g/cm^3
	Minimum Specific Energy	e_{floor}	-9.99998E+99	erg/g
	Gamma	Γ_o	0.97	N/A
	Slope of Shock Speed – Particle Velocity Plot	S	1.86	N/A
	Square of Reference Sound Speed	$C_s^{\,2}$	4.048E+10	cm^2/s^2

3. Charge Parameters

In all simulations, except where specifically noted, a standard charge of HBX-1 was used. The charge weight was 60 pounds or 27.215 kilograms. It was placed at a depth of 32.8 feet or ten meters. As noted in Section II.A.3, by keeping the charge weight and depth constant, the resulting shockwave and bubble parameters remain constant. This allows the effects of the presence and properties of the Lagrangian solid bottom to be determined.

4. Structural Finite Element Model

The Floating Shock Platform (FSP) finite element model was used for all simulations involving a floating structure. The FSP is a well-defined model whose properties and behaviors under shock loading have been thoroughly tested and validated. Additionally, its relatively small number of elements (12,792) and total size (approximately 9m x 5m x 2.5m) allowed for quick simulation times. The particular FSP model used has been slightly modified from the true structure. A thin, lightweight, highly flexible, elastic roof has been attached over the open-topped FSP. This was done in order to be able to define the entire FSP as a one singly-wetted interface on all six sides.

In order to accurately model the Lagrangian solid bottom, the selection of the appropriate constitutive equation for the material is important. The most applicable soil models available in Dyna_N are material types 16, 45, and 65. These models were created to model concrete and geologic materials. Due to the complexities of these soil models, in conjunction with the creation of a new method of Lagrangian solid bottom modeling, these material types were

not considered in this research. In order to ensure the fewest errors while testing new modeling methods, an elastic material model was utilized. The properties of the material used were developed from Bangash's research into explosion dynamics of numerous soil materials and are listed in Table 8 [23].

Table 8. Lagrangian Solid Bottom Elastic Soil Properties

Property	Value	Units
Density	2.0	g/cm^3
Elastic Modulus	2.0E+11	$dyne/cm^2$
Poisson's Ratio	0.3	N/A

5. Summary of Simulation Setup

All of the values, properties, and decisions made in the setup for each simulation started from the guidance set forth in this section. This basic construct was used to develop and test the initial Lagrangian solid bottom model. Various modifications were made as the model and its parameters were proven. Figure 11 provides a visualization of the fluid domain along with the FSP used in this standardized setup. A complete index of simulations that were conducted in this research can be found in the Appendix.

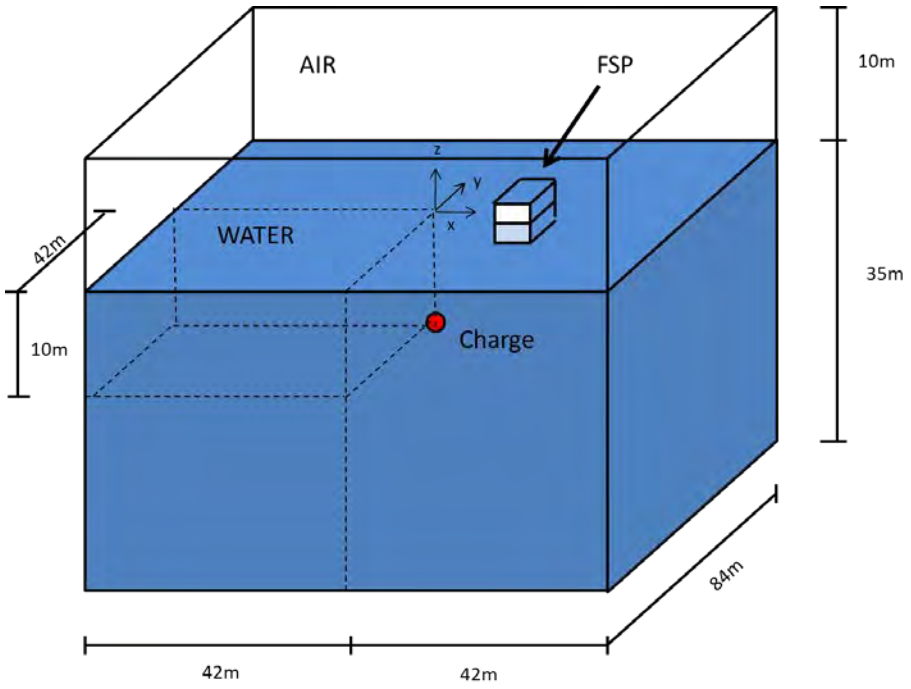

Figure 11. Standard DYSMAS Simulation Geometry

THIS PAGE INTENTIONALLY LEFT BLANK

IV. LAGRANGIAN SOLID BOTTOM MODELING IN DYSMAS

There are two fundamentally different approaches to modeling a Lagrangian solid bottom in DYSMAS. The first approach is depicted in Figure 12. This method places the entire structure within the bounds of the fluid domain. This approach closely resembles the placement of a ship's FEM in the fluid domain. As such, it would be relatively easy to implement. However, the constitutive equations that govern the behavior of the soil material in both Dyna_N and Gemini can never be perfectly matched.

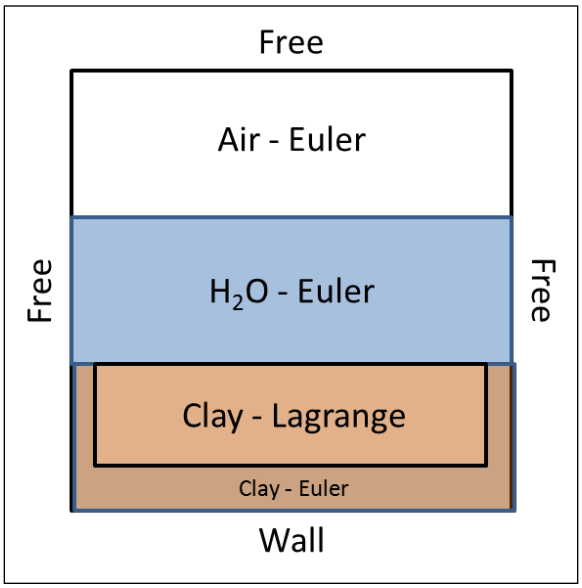

Figure 12. Bottom Fully Contained within Fluid

The second approach is to place the Lagrangian solid bottom only partially within the fluid domain as shown in Figure 13. This allows the soil to be treated as a semi-infinite domain and reduces the amount of cells in the fluid domain. The reduction in number of fluid cells in the Euler grid has the potential to decrease the computational

time and resources needed for each simulation. This approach requires the investigation of the parameters involved in implementing the first approach plus additional parameters unique only to this method. For this reason, the second approach was chosen as the primary method to Lagrangian solid bottom modeling in this research.

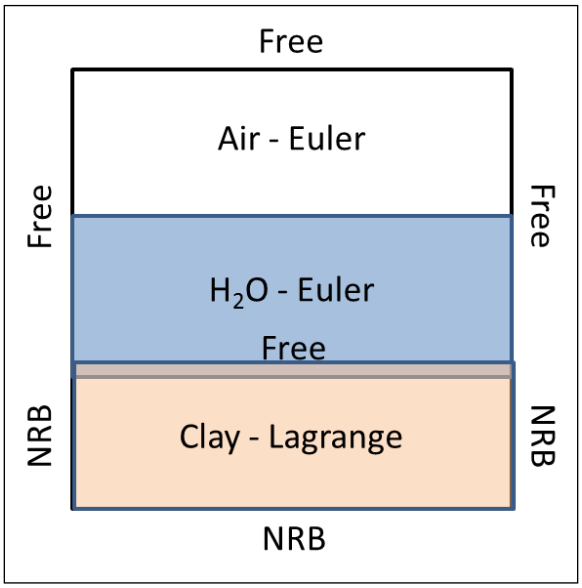

Figure 13. Bottom Outside the Fluid

A. SIZE AND POSITION OF LAGRANGIAN SOLID BOTTOM

The first consideration to be made when developing the ocean bottom model for Dyna_N is the size of the model. Both the overall size and individual element size have significant consequences for the simulation's outcome.

1. Lateral Dimensions and Position

The overall size is governed by two factors. The first is the coupling interface requirement of the fluid code, Gemini. Gemini allows nodes describing surface elements and their associated singly-wetted interfaces (SWI) to be

positioned on the boundary of the fluid domain. A SWI occurs when the element is only in contact with the fluid on one of its sides. The edges of the SWI cannot terminate within the fluid domain. They must entirely enclose the structure, or they must extend to or beyond the boundaries of the fluid domain. The degree of nodal position precision required by the interface requirement is within 10^{-6} centimeters. Most structural finite element pre-processors do not achieve that degree of precision. The result is that the Lagrangian solid bottom must be expanded in the lateral dimensions (X,Y) to a size just greater than the lateral dimensions of the fluid domain. In doing so, the only interface required is the top surface of the Lagrangian solid bottom. The size requirement places this approach at a disadvantage when compared with a Lagrangian solid bottom, which is wholly contained within the fluid, as shown in Figure 12 [18].

The portion of the initial shockwave that is reflected toward the target by the bottom only impacts the bottom in a finite area between the charge and the target. Leveraging this knowledge, a Lagrangian solid bottom entirely within the fluid could be sized to cover only the area that would reflect the shockwave. This approach would allow the Lagrangian solid bottom to be considerably smaller than the Lagrangian solid bottom, which extends past the lateral dimensions of the fluid domain. The reduction in resources required to solve the Lagrangian solid bottom response is significant. Given the example simulation parameters listed in Table 9, modeling the Lagrangian solid bottom only within the region of interest would reduce the number of Lagrange elements by 99.5%. This second approach would

require the addition of fluid cells to make up for the 99.5% decrease in volume. Thus the approach simply reduced the computational requirements of the structural solver at the expense of increased computational requirements of the fluid solver. If the bottom were made up of two different materials, an Euler and a Lagrange soil, the bottom reflection cannot be assumed to be accurate across the entire fluid domain. This is due to the fact that the equations of states for the fluid and the constitutive equations for the structure are not perfectly matched. Therefore, modeling the bottom only in the region of interest is unlikely to give a valid response when compared to empirical data.

Table 9. Bottom Modeling Approach Comparison

Charge		**Fluid**		**Target**	
Type	HBX-1	**X Width**	84 m	**Position**	Surface
Weight	60 lbf	**Y Width**	84 m	**Separation**	6 m
Depth	10 m	**Z Depth**	35 m		
Bottom Modeling Approach					
Large			**Focused**		
Shape	Parallelepiped		**Shape**	Parallelepiped	
X Width	84.02 m		**X Width**	6 m	
Y Width	84.02 m		**Y Width**	6 m	
Thickness	5 m		**Thickness**	5 m	
# Elements	35,280		**# Elements**	180	

2. Vertical Dimensions and Position

The vertical position of the Lagrangian solid bottom is obviously determined by the required bottom depth of the simulation. However, the top surface of the bottom cannot be simply joined to the bottom of the fluid domain. In Figure 13, with the Lagrangian solid bottom outside of the fluid, the slight overlap of the fluid domain and

Lagrangian solid bottom is required. The bottom is expected to deform under hydrostatic pressure, shockwave pressure, and its own self-weight. The deformation is assumed to be in the negative Z-direction. Remembering the SWI requirement that the interface cannot be more than 10^{-6} cm from the edge of the fluid domain, the requirement to overlap the fluid domain and the bottom becomes apparent. This overlap prevents the interface from leaving the fluid domain due to the deformation. The necessity to include gravity in the structural solver requires the application of vertical constraints on the bottom surface of the Lagrangian solid bottom. These constraints keep the structure from bodily translating out of the domain. In all simulations in this research the minimum overlap was one meter at the deepest point of the water-soil interface.

An understanding of the required thickness of the Lagrangian solid bottom was developed through the examination of wave propagation in the solid. When a shockwave is incident on an interface between dissimilar materials the wave behaves under Snell's law. The result is the possibility of a reflection and/or a transmission wave. The reflected wave is the sent back into the original material, while the transmitted wave propagates through the new material. When examining shallow water UNDEX, the properties and effect of the initial reflected wave are the primary interest. Conversely, the wave transmitted into the soil is of little consequence because it is assumed to have propagated through the seabed and dissipated over some distance. Due to the finite nature of the bottom model, this effect is not seen. As the transmitted wave propagates through the solid material, the nodal constraints that

prevent structural translation reflect this wave back up through the soil structure. Upon reaching the water-soil interface, a shockwave is transmitted into the fluid domain that follows close behind the initial bottom reflection. For the extent of this research, this artificial wave is referred to as the retransmission wave. The time delay between the bottom reflection and the retransmission is governed by the thickness of the soil structure. As the thickness increases so too does the delay. In order to decrease the effect of the retransmission, the thickness of the Lagrangian solid bottom must be increased to a relatively large size. The obvious limit to expanding the thickness is once again the limit of computational resources. Further discussion of the retransmission effect and methods to diminish it are discussed in greater detail in Section IV.B.2.

3. Element Size

There are no set restrictions on the size of individual solid elements within the Lagrangian solid bottom. All of the following suggested guidelines were formed through discussions with various subject matter experts and review of cautions located in the Dyna_N User's Manual.

The U.S. Bureau of Reclamation has done extensive simulations of UNDEX shock loading on dam structures utilizing the DYSMAS software package. The dam structure's finite element models were constructed mainly with solid elements with the material properties of concrete. An examination of the size of their solid elements provided a guide for the dimensions that were adopted in this

research. In the region of interest on the dam structure, the solid elements were approximately two to three feet on each side. The mesh expanded toward the bounds of the model with some elements reaching 20 to 30 feet on a side. This research adopted solid elements that were one meter in each lateral dimension. This lateral sizing was maintained for every Lagrangian solid bottom model used [24].

Several of the simulations used Lagrangian solid bottoms in which the profile changed vertically across the fluid domain. The vertical dimensions of the solid elements were allowed to expand and contract as necessary in order to create these contours. The only constraint placed upon the vertical dimensions was that it must be no more than three times as large or as small as the lateral dimensions. This allowed the vertical dimension to vary between three meters and one third of a meter [25].

B. BOUNDARY CONDITIONS AND CONSTRAINTS

Typical DYSMAS simulations of UNDEX events involve a buoyant ship's finite element model that is wholly contained within the fluid domain. As discussed in Section III.D, the linkage between the two is defined through the use of the interfaces and the SCI software. Through these interfaces the shock loading and the buoyant forces are applied to the structure. The buoyant forces on the structure serve as the boundary conditions for the structure.

Unlike the ship, the non-buoyant Lagrangian solid bottom requires the application of boundary conditions other than the Gemini interfaces. This requirement holds true no matter whether the model is wholly within the fluid

domain or not. If there were no boundary conditions on the Lagrangian solid bottom, the gravity loading and hydrostatic pressure loading would cause the bottom to "fall away" from the bottom of the fluid domain.

1. Fixed Nodal Displacements

The initial solution used was the application of Dirichlet, or fixed, boundary conditions to the model. All the nodes on the lateral and bottom faces of the structure were constrained in all six nodal degrees of freedom: translation in and rotation about the X, Y, and Z axes. Table 10 details the pertinent simulation and model data used to simulate the effect of the nodal constraints. These initial investigations all used a purely elastic bottom material to avoid any material-specific errors.

Table 10. Input Parameters for Run ID 4-01

Charge		**Fluid**		**Target**	
Type	HBX-1	**X Width**	84 m	**Position**	N/A
Weight	60 lbf	**Y Width**	84 m	**Separation**	N/A
Depth	10 m	**Z Depth**	35 m		
Bottom					
Dimensions			**Material**		
Shape	Parallelepiped		**Type**	Elastic	
X Width	84.02 m		**Density**	2.0 gram/cm^3	
Y Width	84.02 m		**Elastic Modulus**	2 x 10^{11} dyne/cm^2	
Thickness	5 m		**Poisson's Ratio**	0.3	
# Elements	35,280		**EOS Type**	None	
Boundary Conditions					
All nodes on lateral faces and underside of the Lagrangian solid bottom were constrained from translation and rotation in all three axes.					

This initial simulation using a Lagrangian solid bottom with nodal constraints was compared to a fluid-only simulation of the charge and fluid parameters that utilized a perfectly reflective bottom boundary. Figure 14 compares the pressure distributions through the fluid domain of each simulation at 30 milliseconds. Both simulations show a similar bottom reflection of the initial shockwave. The difference is the presence of a second pressure wave propagating from the bottom in Figure 14(B).

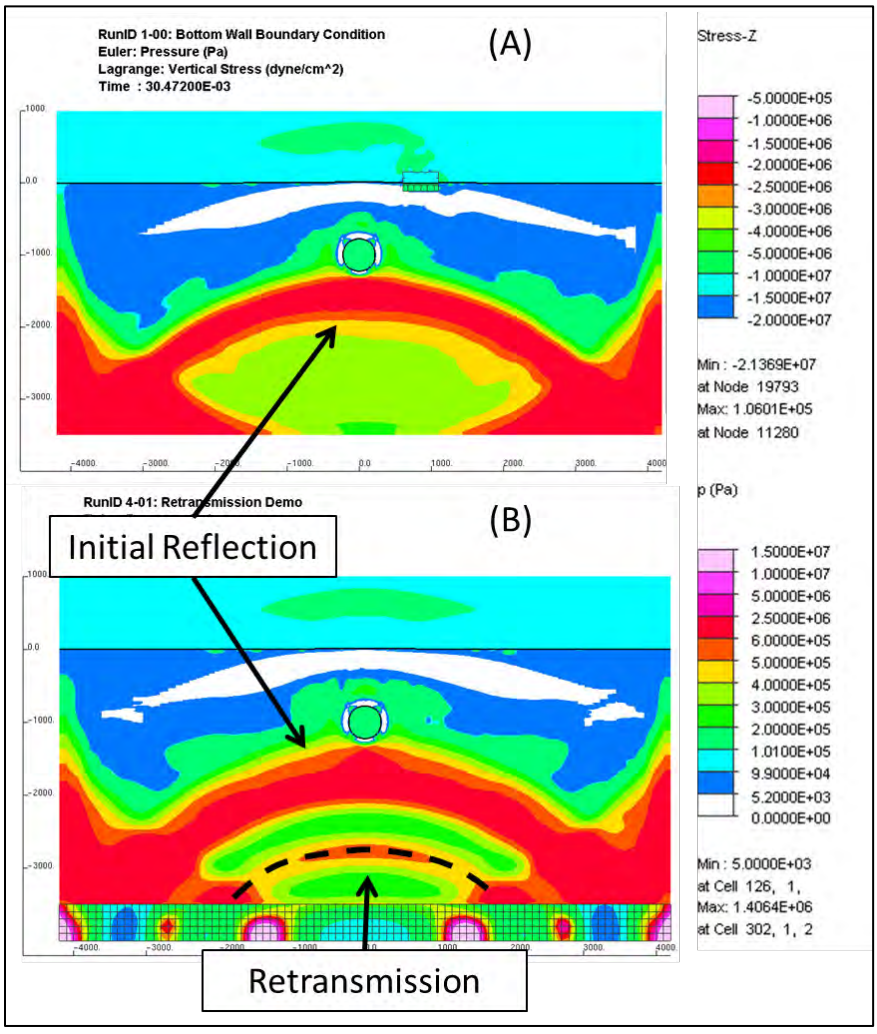

Figure 14. Pressure Distribution at t=30 msec for: (A) Perfectly Reflected Boundary & (B) Lagrangian Solid Bottom Boundary with Retransmission

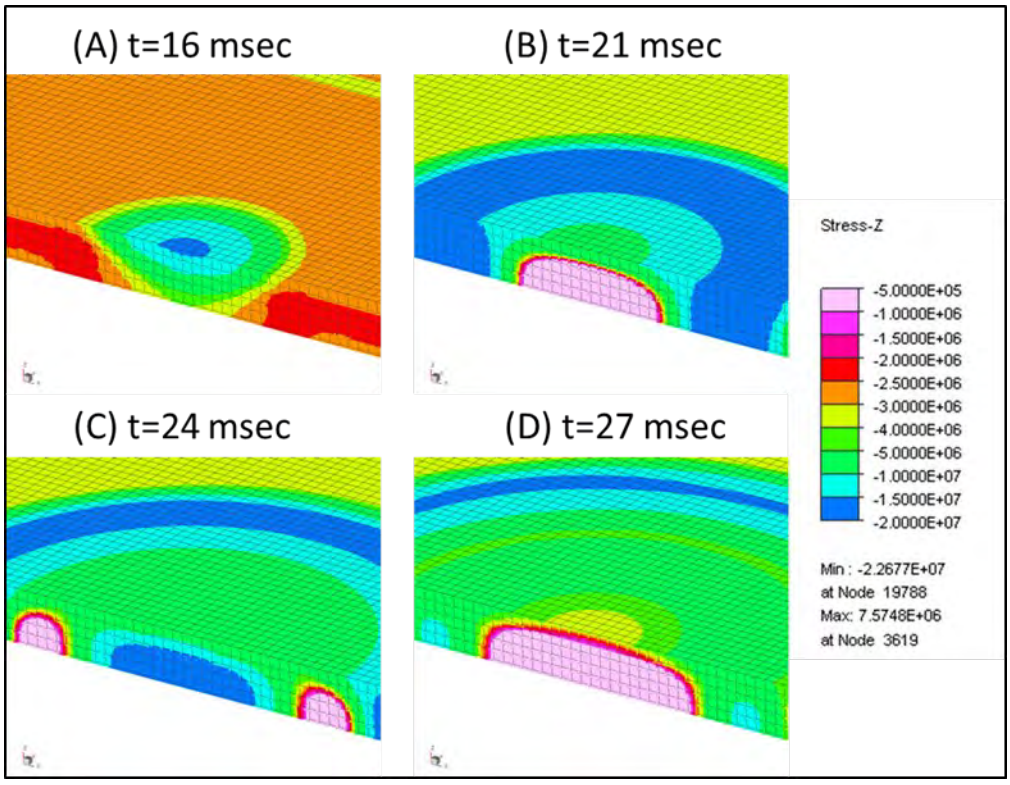

Figure 15. Timeline of Vertical (Z) Stress through Center of Lagrangian Solid Bottom with Nodal Constraints

As previously discussed, this wave is the retransmission wave. A review of the vertical (Z) stress field in the Lagrangian solid bottom in Figure 15 gives a better understanding of this effect. The impact of the initial shockwave (Figure 15(A)) causes an increase in compressive stress (blue region). As the wave travels through the material it is reflected off the nodal constraints (Figure 15(B)) back up thru the model causing a decrease in the compressive stress (pink region). The expanded portion of the structure then causes the retransmission of the initial shockwave back into the fluid domain. The Lagrangian solid bottom then continues to compress and expand as it attempts dissipate the shock

energy. In nature, once the shockwave had entered the soil it would propagate through the infinite soil medium until the wave dissipated or reached a different medium, like bedrock. Due to the finite dimensions of the model, as the shockwave reaches the boundaries, it is reflected off of the fixed nodal constraints and causes a retransmission to the fluid domain. Simply removing the nodal constraints on the bottom surface will only serve to make the bottom side of the structure behave as a free surface and retransmit a rarefaction wave.

2. Reducing Retransmission

Figure 14(B) makes it apparent that the pressure of the retransmission is less than that of the initial reflection. This is a result of energy dissipation as the wave passes through the thickness of the model. Therefore to minimize the retransmission the initial solution was to increase the distance through which the wave must travel. By increasing the bottom thickness the retransmission could be reduced to a negligible level.

A follow-on simulation was run in which the bottom thickness was increased from five to ten meters. The remainder of the simulation input parameters were held constant with Table 10. The pressure-time histories for both simulations at a point five meters above the bottom are in Figure 16. By doubling the thickness, the retransmission was delayed by three milliseconds and decreased in pressure by 2.5×10^5 Pa. In order for the retransmission to be considered negligible, the wave pressure should be nearly equal to the hydrostatic pressure the bottom would normally feel, which is approximately 4.5

x 10^5 Pa. Assuming a linear relationship between bottom thickness and pressure decrease, the bottom would have to be 20 meters thick for the retransmission pressure to be considered negligible. This relationship only holds for a 60lb charge of HBX-1. An increase in charge size would result in a corresponding increase in bottom thickness. The extraordinary number of additional structural elements required to increase the thickness would require a significant increase in computational resources and time.

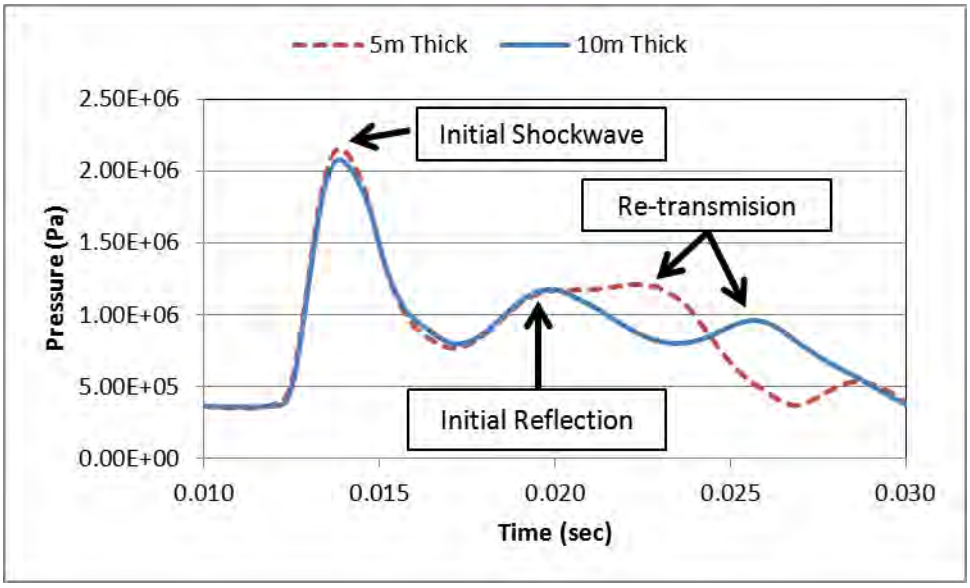

Figure 16. Pressure-Time History 5 Meters above Bottom (x=-5cm, y=-5cm, z=-3022cm)

3. Non-Reflecting Boundary Segments

The boundary condition solution had to not only keep the Lagrangian solid bottom in position, but also allow the structure to behave as a semi-infinite domain. The problem of modeling a semi-infinite soil medium has been encountered previously in structural dynamic analyses on dams and free-standing structures. The approach used by O'Shea utilized LS-DYNA's transmitting boundary segments in

order to simulate a semi-infinite soil domain around the Parker Dam. Dyna_N contains an identical function listed as non-reflecting boundary (NRB) segments [26].

According to the Dyna_N User's Guide, the NRB segments are to be applied to the exterior boundaries of infinite domains in order to prevent artificial stress wave reflections generated at the model boundaries from re-entering the model and contaminating the results. This is done through the use of impedance matching functions that apply normal and shear stresses of the form:

$$\sigma_{normal} = -\rho c_d V_{normal} \quad \& \quad \sigma_{shear} = -\rho c_s V_{\tan},$$

which utilize the material density (ρ), the dilatational wave speed (c_d), and the shear wave speed (c_s). This makes the magnitude of these stresses proportional to the normal and tangential particle velocities at the boundary [27].

The application of NRB segments allows the passage of shockwaves out of the material. Unfortunately, due to their nature as Neumman, or flux, boundary conditions they directly conflict with the application of fixed nodal constraints. Nodal displacements constraints are set through enforcement of zero acceleration of the nodes [19]. Since the applied nodal forces are simply mass multiplied by acceleration, the application of both boundary conditions simultaneously is not feasible. It is unclear from the theoretical manuals for Dyna_N, which boundary condition is given precedent when both conditions are applied. The research by Zhenxia proved that the transmitting boundary segments in LS-DYNA are insufficient to handle low-frequency loading, including static loads.

The result of applying solely NRB segments to a static problem is a permanent translation of the structure. This result is confirmed by analysis of the NRB segments governing equations. When the object is at rest, the particle velocities are zero, thus the flux boundary conditions exert zero force on the object. Not until the object has displaced will the NRB segments fully support the static loading [28].

4. Application of Nodal Forces

O'Shea overcame this error through the application of static forces to the structure. Initially, the model was statically loaded with the semi-infinite edges set as fully constrained nodes. A static solution was found for the reaction force at each constrained node. These static forces were then applied to the dynamic model to act as the static nodal constraints. Thus, O'Shea applied two flux boundary conditions to his structure: the NRB segments for the shockwaves, and static nodal forces to replace the nodal constraints [26].

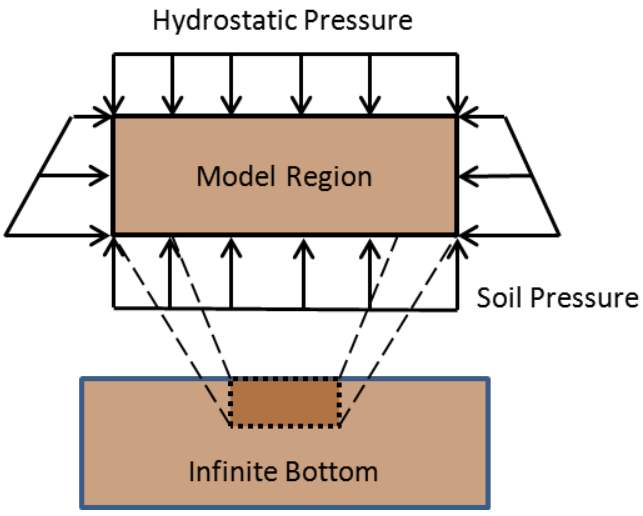

Figure 17. Soil Structure Free Body Diagram

Table 11. Soil Nodal Forces

Nodal Forces (x 10^{10} dynes)	Interior Node	Edge Node	Corner Node
F_z	5.4130	2.7065	5.4130
F_xy_1	2.2489	1.1244	n/a
F_xy_2	4.6285	2.3142	n/a
F_xy_3	4.8246	2.4123	n/a
F_xy_4	5.0207	2.5104	n/a
F_xy_5	5.2169	2.6084	n/a
F_xy_6	2.6738	1.3369	n/a

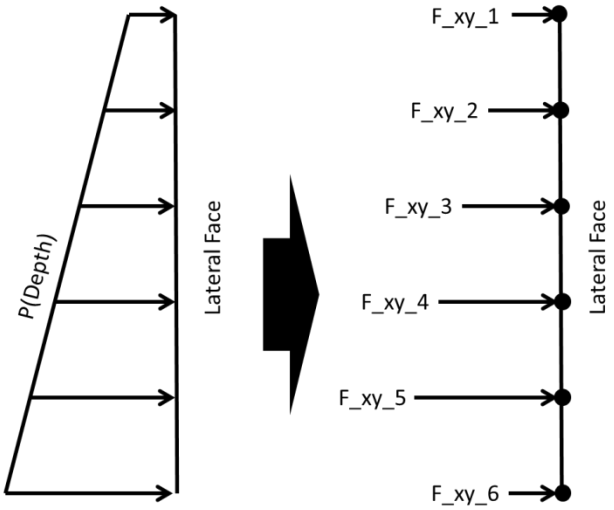

Figure 18. Diagram of Lateral Node Force Locations associated with Table 11

A simulation was conducted using a five meter thick Lagrangian solid bottom with the application of the nodal force method used by O'Shea. The parameters of the simulation are located in Table 12. In addition to NRB segments on the lateral and bottom sides, the nodal forces from Table 11 were applied to the model. These nodal forces were calculated based upon the application of in-situ soil hydrostatic pressures depicted in Figure 17. Figure 19 demonstrates that this combination of boundary conditions showed almost no signs of retransmission as compared with the nodal constraints simulation. Based upon these results,

the combination of NRB segments and nodal forces will be utilized in all subsequent models investigating additional bottom modeling parameters.

Table 12. Input Parameters for Run ID 4-07

Charge		Fluid		Target	
Type	HBX-1	**X Width**	84 m	**Position**	N/A
Weight	60 lbf	**Y Width**	84 m	**Separation**	N/A
Depth	10 m	**Z Depth**	35 m		
Bottom					
Dimensions			**Material**		
Shape	Parallelepiped		**Type**	Elastic	
X Width	84.02 m		**Density**	2.0 gram/cm^3	
Y Width	84.02 m		**Elastic Modulus**	2 x 10^{11} dyne/cm^2	
Thickness	5 m		**Poisson's Ratio**	0.3	
# Elements	35,280		**EOS Type**	None	
Boundary Conditions					
All nodes on lateral faces and underside of the Lagrangian solid bottom have nodal forces normal to its surface, which are the reaction forces of the static solution of the structure. The same faces have NRBs applied.					

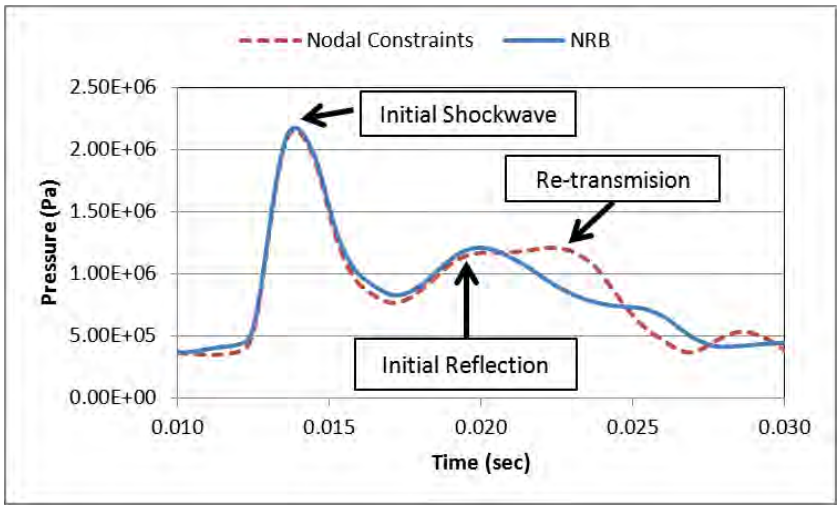

Figure 19. Pressure Time History 5 meters above Ocean Bottom, Euler Coordinates (x=-5cm, y=-5cm, z=-3022cm) for RunID_4_01 & _07 Highlighting Effectiveness of NRB

The initial method used to determine the nodal forces was a rough estimate for a simple geometric shape in order to validate the use of NRB segments and nodal forces. In order to accurately determine the true nodal forces, a static solution of the structure needed to be solved. This was accomplished through the use of the ANSYS 12.1 Structural APDL Software Package. For the nodal forces to be easily input into Dyna_N it was critical that ANSYS use the exact same finite element model that was generated for Dyna_N. This required converting the node and element files generated by the DYSMAS processor into a format that ANSYS could read. Conversely, the reaction forces for the nodal constraints had to be converted into the required Dyna_N format. Both of these tasks were accomplished through the development and application of MATLAB script files. MATLAB was utilized due to the author's familiarity with it, though this perhaps not the only means to convert and transfer the data and results. Additionally the MATLAB script generated the necessary script files to run the ANSYS solution with minimal input from the user. Once the node and element file had been read into ANSYS, the hydrostatic pressure curve was generated and then applied to the interface surfaces. The script then constrained the remaining boundary nodes in the direction normal to the surface on which they were located. For example, if the node lay on a lateral face of the structure that was normal to the X axis, then ANSYS constrained that node from moving in the X direction. ANSYS then determined the static solution and displayed the reaction forces at the constrained nodes.

A note of caution is attached to the use of NRB segments. The viscous equations the NRB segments use assume that the structure is composed of an isotropic, linear elastic material. All simulations to this point have utilized a perfectly elastic material. This limitation could prove problematic depending upon the selection of the most accurate material model for soil [27].

C. INITIAL BOTTOM WAVE ELIMINATION

Analysis of all of the previous simulations shows that at the start of the simulation a pressure wave emanates at the water-soil interface. This wave formation is demonstrated in Figure 20. Figure 20(A) is the state of the simulation at the start time. Figure 20(B) shows the initial wave formation with the pressure dropping 0.5×10^5 Pa at the wave crest within the first 1.5 milliseconds of the simulation. After another three milliseconds, the pressure has increased to 0.5×10^5 Pa above the expected hydrostatic value in Figure 20(C). The variations in the contour plots in Figures 20(A-C) demonstrate that this wave is present along the entire water-soil interface. Just before the initial explosive shockwave interacts with this bottom wave, the explosive shockwave's pressure is approximately 3×10^6 Pa. With the pressure differential across the bottom wave of a third the magnitude of the explosive shockwave, this flow field cannot be considered negligible and must be corrected.

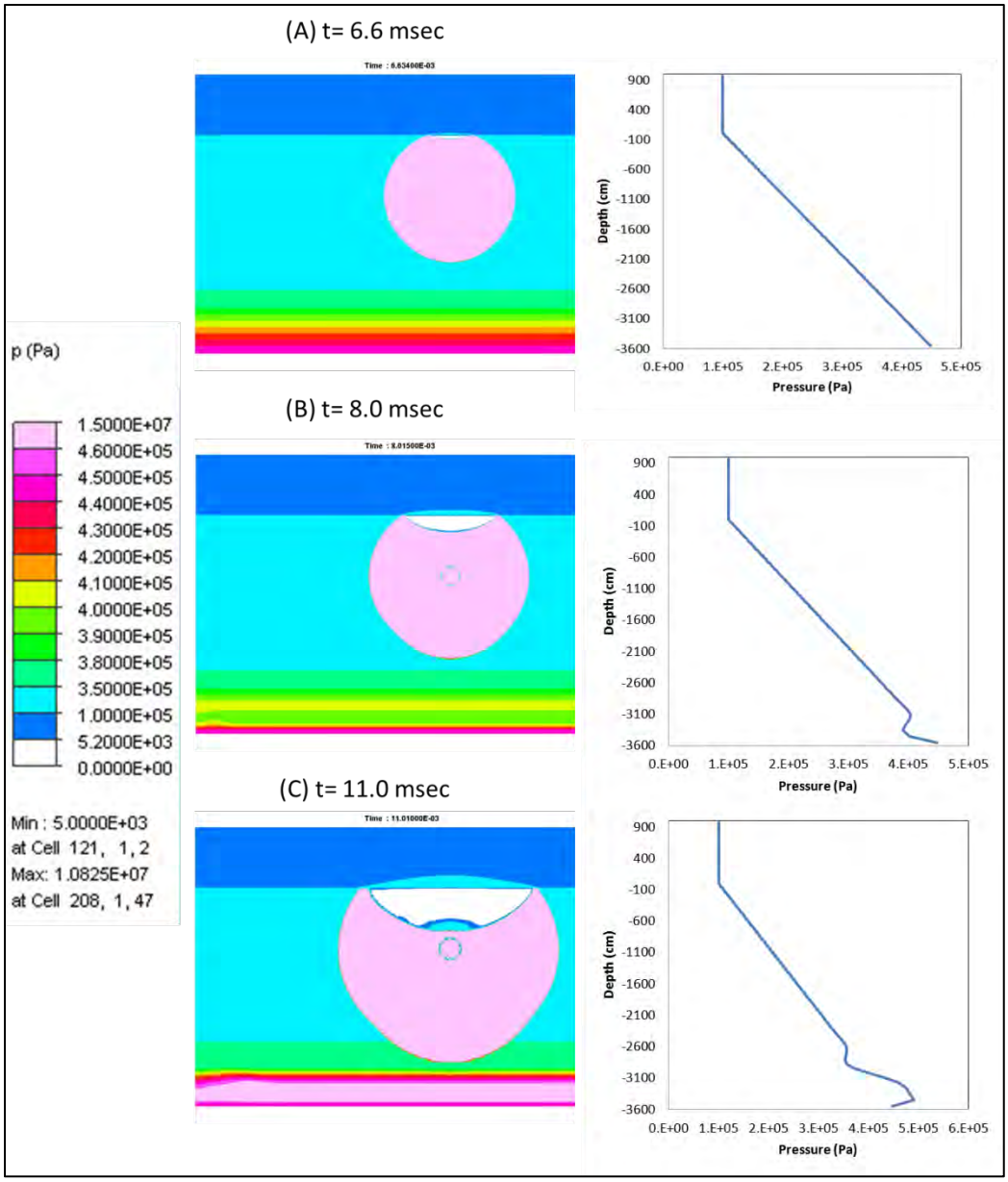

Figure 20. Initial Bottom Wave Formation

This initial bottom wave is the result of the structural deformation of the interface. When the simulation starts, the previously unloaded Lagrangian solid bottom is instantaneously loaded with the hydrostatic pressure from the fluid domain and the nodal forces developed in Section IV.B.4 to act as nodal constraints.

The compressive loading of the structure in all three dimensions causes the structure to volumetrically strain. This strain is the cause of the displacement of the water-soil interface. As the interface displaces downward, the water is "pulled" down as well in order to maintain the interface. Thus the initial bottom wave takes the form of a tensile pressure wave. As with any elastic material, the structure does not simply deform directly to its equilibrium position. Instead, it will oscillate like spring about its equilibrium position until it settles out [29]. This oscillation of the interface in the vertical direction causes the subsequent pressure rise above hydrostatic after the initial tensile wave. This motion was observed by tracking the vertical position of a node in the Lagrangian solid bottom, which lay on the water-soil interface (Figure 21). Points A, B, and C in Figure 21 correspond to the same times as those in Figure 20. An additional factor that contributes to the pressure increase at the water-soil interface is the presence of back pressure on the singly-wetted interfaces by the Gemini solver.

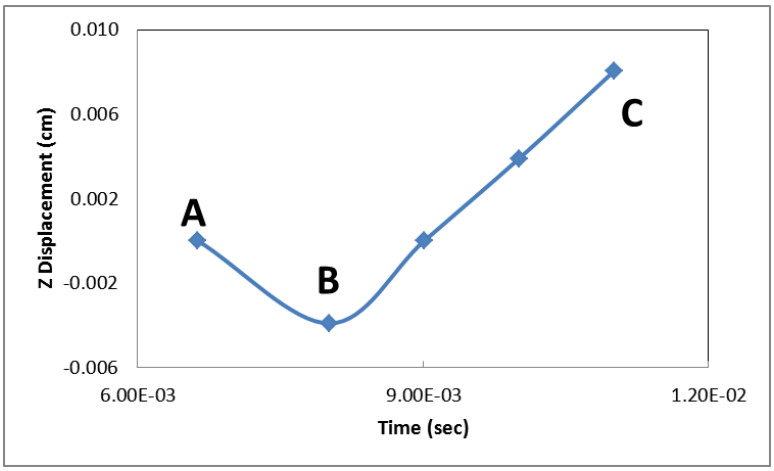

Figure 21. Displacement of Water-Soil Interface

In order to eliminate the initial bottom wave, the Lagrangian solid bottom must be in a deformed state in equilibrium with the hydrostatic pressure at the water-soil interface and the applied nodal forces developed in Section IV.B.4 when the simulation begins. The following sections discuss the multiple options the user has in accomplishing this task.

Two of the methods to reduce the initial bottom wave require the restart of a DYSMAS simulation. Thus an understanding of the abilities and limitations of restarting simulations is required. Coupled DYSMAS simulations can be restarted with the addition of two lines of code to the Dyna_N input file. During a restart several features of a given model can be modified from the original simulation. Among the modifiable features are changes in termination time, deletion of materials, deletion of elements, and modifications to the translational or rotational boundary conditions of nodes. The restart simulations utilized restart dump files created at specific time intervals throughout normal simulations and at the conclusion of various other Dyna_N processes [27].

1. Long-Time Static Simulations

Since the goal is to establish an equilibrium state of the model, one possible solution is to allow the structure to interface with a static water column for a significantly long duration of time. At the conclusion of this static simulation, the restart file produced by Dyna_N is then used as the starting structural model in the transient analysis with the desired UNDEX event.

a. Instantaneous Loading

The first simulation was conducted with a Lagrangian solid bottom and fluid domain with the parameters in Table 13. Nodal displacement constraints were used instead of nodal forces to prevent possibly significant structural movement over the long duration of the simulation. The nature of the Dyna_N restart capability allows the user to reinsert the forces during the UNDEX simulation. The differences in the fluid domain were the lack of an explosive charge, the application of wall boundary conditions on the lateral sides, and setting the back pressure for the singly-wetted interfaces to zero. The wall boundary conditions were applied after previous simulations with free boundary conditions and a static water column had shown the water level falling several meters over the course of the simulations. The rational for setting the back pressure to zero is thoroughly discussed in Section IV.C.2.d. This simulation was run out to 2.5 seconds with the expectation that the structure would achieve equilibrium within that time span.

The results of this instantaneously-loaded, long-time simulation are displayed in Figure 22. On the left side of Figure 22, it is important to note that the maximum vertical deformation occurred at the water-soil interface with a value of -0.0072 centimeters. This closely agrees with an ANSYS Structural APDL static solution for the same structure and loading conditions where the deformation of the top surface was -0.007 centimeters. The right hand side of Figure 22 demonstrates the layered nature of the vertical stresses. The stresses decrease in magnitude going

from the interface to the bottom of the structure. This behavior is consistent with the uniaxial compression of an object that is prevented from expanding in the other two principal directions. The ANSYS solution concurred with this stress pattern as well. While this method appears to be reasonably accurate, a quick examination of the vertical velocity of the water-soil interface in Figure 23 shows that small oscillations are still occurring. This will cause some small distortions to the fluid field.

Table 13. Run ID 3-01 and 3-02 Simulation Parameters

Charge		**Fluid**		**Target**	
Type	N/A	**X Width**	84 m	**Position**	N/A
Weight	N/A	**Y Width**	84 m	**Separation**	N/A
Depth	N/A	**Z Depth**	35 m		
Bottom					
Dimensions		**Material**			
Shape	Parallelepiped	**Type**	Elastic		
X Width	84.02 m	**Density**	2.0 gram/cm^3		
Y Width	84.02 m	**Elastic Modulus**	2 x 10^{11} dyne/cm^2		
Thickness	5 m	**Poisson's Ratio**	0.3		
# Elements	35,280	**EOS Type**	None		
Boundary Conditions					
All nodes on lateral faces and underside of the Lagrangian solid bottom have displacement constraints normal to the surface on which they lie. NRB segments were applied to the same faces.					

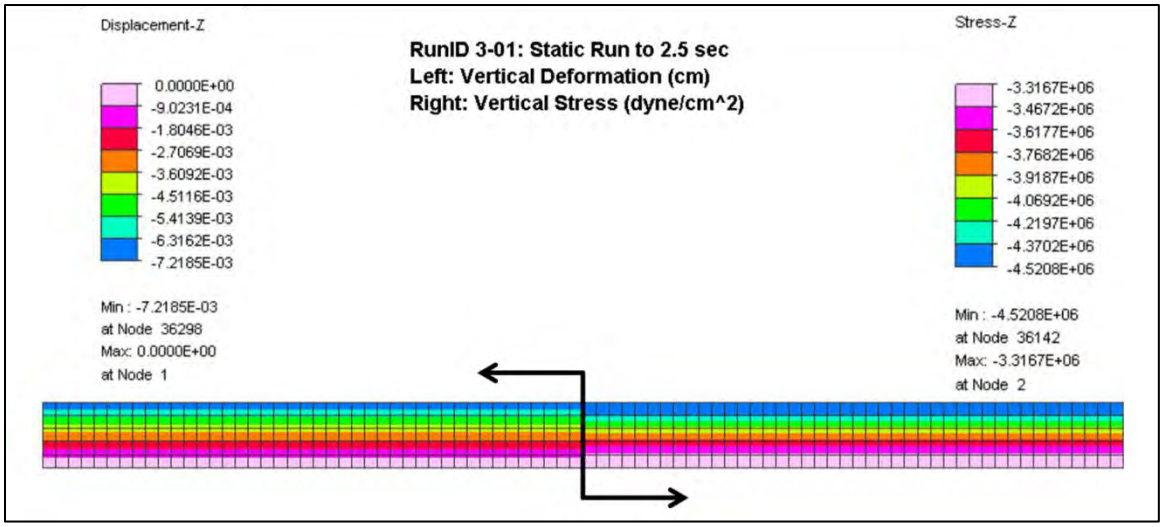

Figure 22. Instantaneously Loaded, Long-Time Static Solution

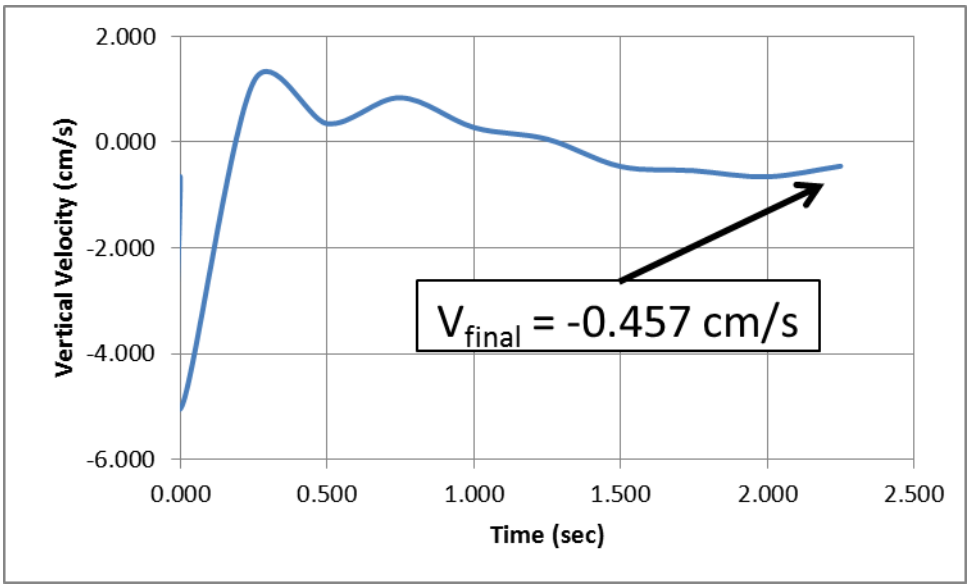

Figure 23. Interface Vertical Velocity for Run ID 3-01

b. Ramped Loading

The second long-time simulation was conducted with conditions applied to minimize the frequency and magnitude of the oscillations the model experiences prior to equilibrium. This was accomplished by gradually

increasing the gravity and hydrostatic pressure loads on the structure over the first 1.25 seconds of the simulation. Implementing this effect in the pre-processor was relatively straightforward. The load curve for the gravitational acceleration was modified from its original constant value to a curve, which began at zero magnitude at time zero and increased linearly to its full value at 1.25 seconds where it remained. The gradual increase in pressure required a slightly different approach because the hydrostatic loading from the water-soil interface could not be directly modified. A pressure loading in addition to the hydrostatic pressure was applied to the interface surface in the pre-processor. This pressure was set to be of equal magnitude, but opposite direction to the hydrostatic loading. This pressure loading was given a load curve that started at full magnitude at time zero and decreased linearly to zero pressure at 1.25 seconds where it remained.

Ramping the loading of the structure demonstrated a significant increase in accuracy. The maximum deflection and vertical stress layers in Figure 24 are nearly identical to those in Figure 22. The true benefit of the ramped loading is the final velocity of the interface surface is only 0.001 cm/s in Figure 25 vice the -0.457 cm/s at the end of the instantaneously loaded structure in Figure 23.

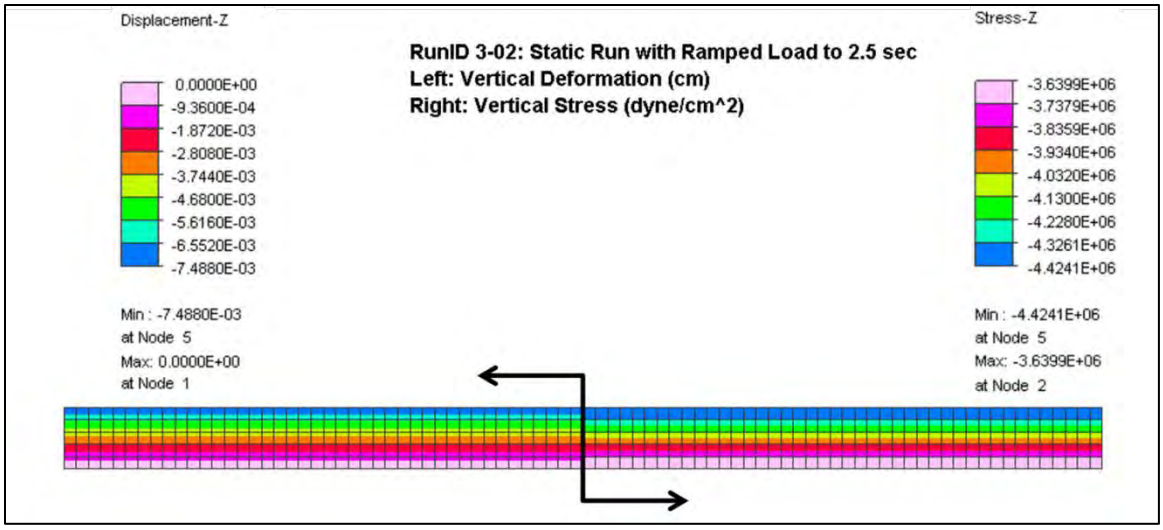

Figure 24. Ramp Loaded, Long-Time Static Solution

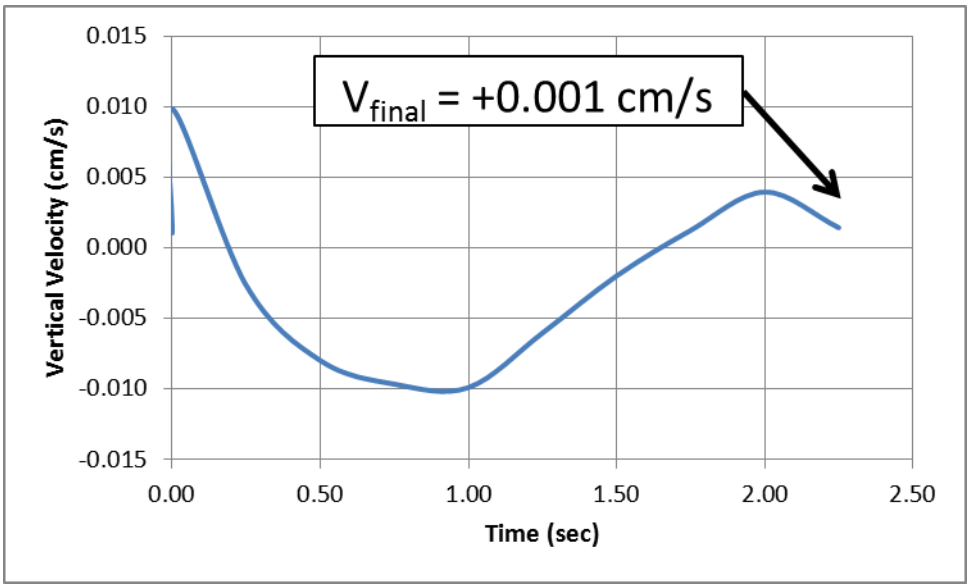

Figure 25. Interface Vertical Velocity for Run ID 3-02

c. Summary

Even though Dyna_N is not the most suitable solution for static problems, the method of long-time simulations to achieve a deformed static structure is viable. The primary advantage of this method is that there are no direct conflicts with any material models or

combination of structures. The obvious drawback is that is computationally expensive to statically simulate large structural models over a long time. This computational expense led to the examination of additional techniques that would eliminate the initial bottom wave [27].

2. Dynamic Relaxation

The Dynamic Relaxation (DR) tool in Dyna_N and the associated Prestress program in Gemini were specifically designed for the problem of finding the deformed shape and the associated stresses of a finite element model in static equilibrium prior to the start of an UNDEX simulation [18], [27]. The DR algorithm is based upon the fact that the solution of a damped dynamic solution converges on a quasi-static solution as time approaches infinity. After applying the defined static and interface loads, the solver steps through the algorithm determining the kinetic energy of the structure and tracking the maximum total kinetic energy. Once the solver determines that the current kinetic energy of the system is a user-defined percentage of the maximum total kinetic energy the system has seen, the solver stops the algorithm and writes a Dyna_N restart file containing the final deformed shape and internal stresses at the last solution step. The default percentage of maximum kinetic energy is 0.1 percent [27]. In order for a Dyna_N restart file to be coupled with a dynamic fluid simulation, the restart file must be created as a coupled run. For DR solutions this coupling is accomplished through the application of the Gemini Prestress function, which provides the hydrostatic pressure loading for the interface segments. Unlike a normal Gemini fluid simulation, Gemini

Prestress is more computationally efficient because it does not create and solve an entire fluid domain [18].

a. Limitations

The use of DR and Gemini Prestress is not without limitations. The DR algorithm is incompatible with non-zero displacement or any velocity boundary conditions. This is in direct conflict with the application of NRB segments, as they are velocity-based boundary conditions. Additionally, the nature of restart files does not allow the addition of NRB segments after the DR solution. This conflict was proven valid after no DR simulation could be started when the structure contained NRB segments. The solver returned an error of excessive deformation or improper definition of a solid element. As the material used was a perfectly elastic material it is not possible to have excessive deformation [19].

A second limitation noted in the literature is the potential for overshoot. If the loads are applied too rapidly, the structure may oscillate about the solution several times prior to achieving the minimum kinetic energy. This can have a severe impact upon materials that are history-dependent. Soils that can experience compaction are prime examples of history-dependent materials. While this research solely utilizes perfectly elastic material, this fact is important to understand prior to the application of more accurate soil material models. The result of the overshoot would be that the soil is over-compacted prior to the UNDEX simulation [27].

Several Lagrangian solid bottoms with varying boundary conditions were dynamically relaxed. The results,

in some cases were promising, but ultimately proved unfeasible for application to Lagrangian solid bottoms. The following is a discussion of the parameters and results of each variation attempted.

b. With Nodal Forces

A DR simulation utilizing only static nodal forces at the boundaries was computationally achieved, but physically inaccurate. The lack of nodal displacement constraints allowed the structure to translate vertically nearly 60 centimeters before a solution was converged upon in Figure 26. Further examination of the results showed that the model was not at rest, but moving vertically with a velocity of four centimeters per second.

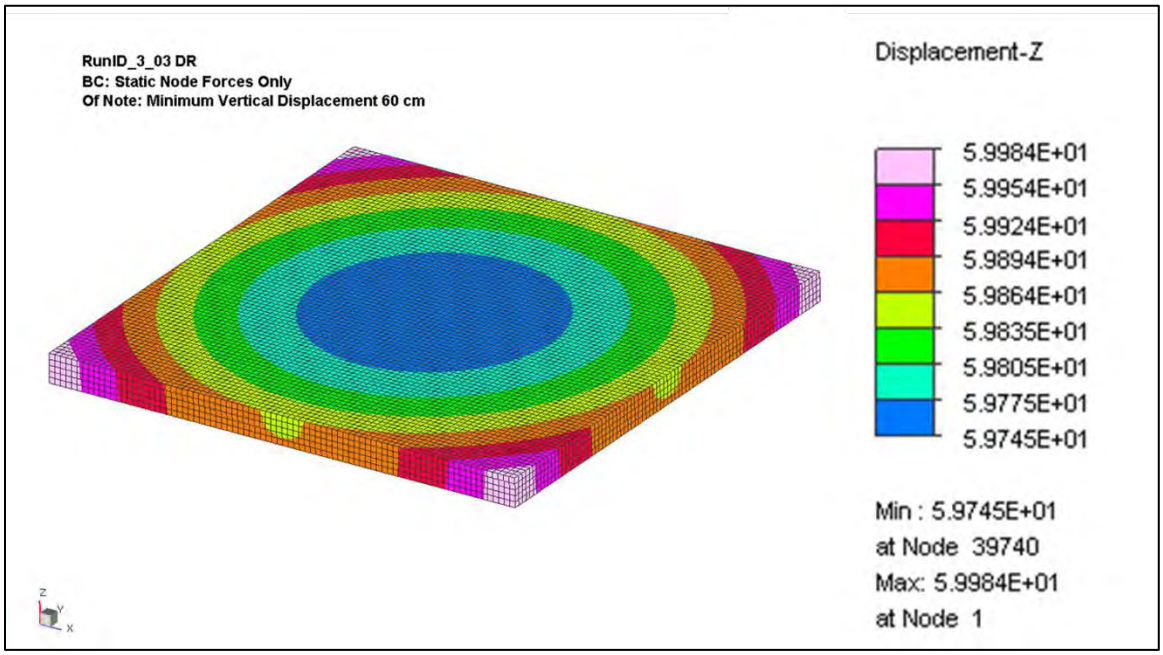

Figure 26. DR with Static Nodal Forces Only

c. With Displacement Constraints

While the application of nodal forces failed, the ability to modify nodal forces and constraints in a restart file, allows the user to dynamically relax a structure with displacement constraints and then replace them with nodal forces in the restart of the transient analysis. The displacement constraints were applied on the lateral and underside of the Lagrangian solid bottom. The nodal constraints prevented movement in the direction normal to the surface where the node was located. Once again, a DR solution was computationally achieved, but physically inaccurate. Observing the vertical displacement through the structure in Figure 27, the bottom surface is fixed at zero displacement as expected. The inaccuracy is noted in the near-zero displacement of the top surface, which should have the greatest displacement. After discussions with a DYSMAS subject matter expert, it was determined that this was likely due to the back pressure applied to the singly-wetted interfaces (SWI) by the Prestress software. During a transient analysis, the user has the ability to adjust the back pressure. The Gemini Prestress function does not give the user this option. The back pressure defaults to 1×10^6 dyne/cm^2 [30].

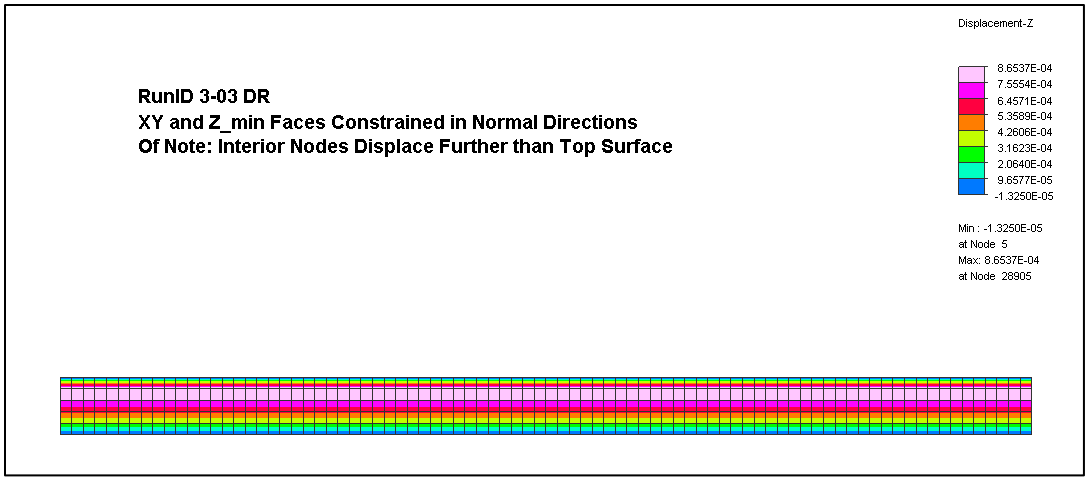

Figure 27. DR with Nodal Constraints

d. Application of Counter Pressure

The final DR simulation utilized the nodal displacement constraints with the addition of a pressure loading to counteract the effects of the Gemini Prestress back pressure. The counter pressure was applied through the application of compressive pressure loading on the singly-wetted interface of 1 x 10^6 dyne/cm^2. A profile of the vertical deformation through the thickness of the model is shown in Figure 28. In this case, the interface surface displaced the most at -0.0018 centimeters. The ANSYS static solution determined that the displacement of the surface should be -0.007 centimeters. This set of boundary conditions provided the closest representation of the static structure.

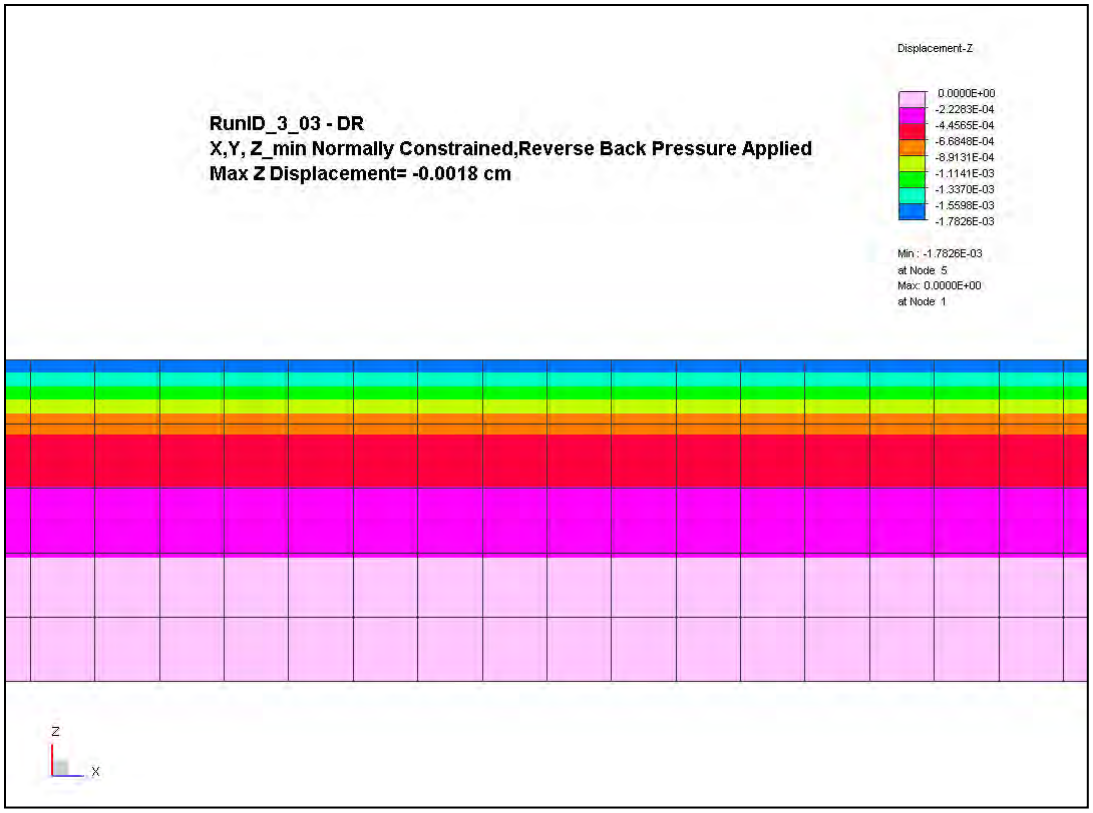

Figure 28. DR with Nodal Constraints and Counter Pressure

e. Summary

While the application of nodal displacement constraints and counter pressure gives a reasonable DR solution, the conflict with the NRB segments significantly diminishes the benefits of using dynamic relaxation in Lagrangian solid bottom modeling. An even greater failure of dynamic relaxation is its apparent inability to successfully relax two separate structures, such as the ocean floor and the FSP. A DR simulation containing two structures failed to converge on a solution. While the runs experienced no errors, the kinetic energy requirement was simply never met. Dynamic relaxation appears to be a semi-

effective tool when modeling the ship structure or the bottom, not both simultaneously.

3. Dyna_N Prestress

The application of the Dyna_N Prestress function offered the best method to reduce the effect of the initial bottom wave. The Prestress/Prestrain function in Dyna_N allows the user to define the stress tensor (σ_{xx}, σ_{yy}, σ_{zz}, σ_{xy}, σ_{yz}, σ_{zx}) and the equivalent plastic strain ($^{P}\varepsilon_{v}$) at the simulation start time for any element in the structure [27]. This function is only briefly mentioned in the Dyna_N User's Manual and the pre-processor does not have an input interface for the user to utilize the function. After discussions with subject matter experts, this function was added to the code by the DYSMAS/P co-developer IABG, and not the Dyna_N code owners at Lawrence Livermore National Laboratory. IABG designed the Dyna_N Prestress function to assist in simulations involving metal forming. As it was designed for use with metal, the function only works correctly when applied to elastic or elastic-plastic material models [31]. While the exact algorithm was not available for reference, it is theorized that the stress tensor serves as the starting point for the elemental stress calculations in Dyna_N at the first step. It does not appear that this stress tensor is translated into an initial elastic strain tensor.

The initial stress tensors utilized were initially calculated by hand in order to test the application of the Dyna_N Prestress function. The stress tensors were made on the assumption that the only stress in the soil was hydrostatic. With the generic flat Lagrangian solid bottom,

which was five meters thick with one meter thick elements, a simple pressure calculation was done at the center of each element to determine the pressures of each row in Table 14. The input card for the Dyna_N Prestress function was generated using a MATLAB script. All shear portions of the stress tensor were assumed to be zero.

Table 14. Bottom Hydrostatic Pressure Distribution

Layer	Depth From Air-Water Interface (cm)	Depth From Water-Soil Interface (cm)	Pressure At Min. Depth ($dyne/cm^2$)	Pressure At Max. Depth ($dyne/cm^2$)	Average Layer Pressure ($dyne/cm^2$)
1	3500-3600	0-100	4.4323×10^6	4.6285×10^6	4.5303×10^6
2	3600-3700	100-200	4.6285×10^6	4.8246×10^6	4.7265×10^6
3	3700-3800	200-300	4.8246×10^6	5.0207×10^6	4.9227×10^6
4	3800-3900	300-400	5.0207×10^6	5.2169×10^6	5.1188×10^6
5	3900-4000	400-500	5.2169×10^6	5.4130×10^6	5.3149×10^6

The average layer pressure in Table 14 was used as the normal stress for the Dyna_N Prestress inputs. A prestresed simulation was conducted with all of the same parameters as the simulation in Table 13. The results in Figure 29 were promising. The application of prestress significantly reduced the initial pressure drop. Even though the prestress function does not deform the structure prior to problem start, it does appear to stiffen the structure. This added stiffness allows the structure to settle at a slower rate, which diminishes the initial pressure drop.

Even with the prestress, the bottom still emits a wave at simulation start. This is due to the use of simple hydrostatic calculations to determine the prestress tensor and the presence of back pressure on the singly-wetted interface (SWI). In order to more accurately represent the

prestress tensor, the static solution in ANSYS was once again utilized. The stress tensor for every element in the structure was printed from the ANSYS static solution. A MATLAB script was used to convert the ANSYS output into the format of the Dyna_N Prestress input. Follow-on simulations that utilized the ANSYS-generated Dyna_N Prestress inputs yielded results consistent with Figure 29(B).

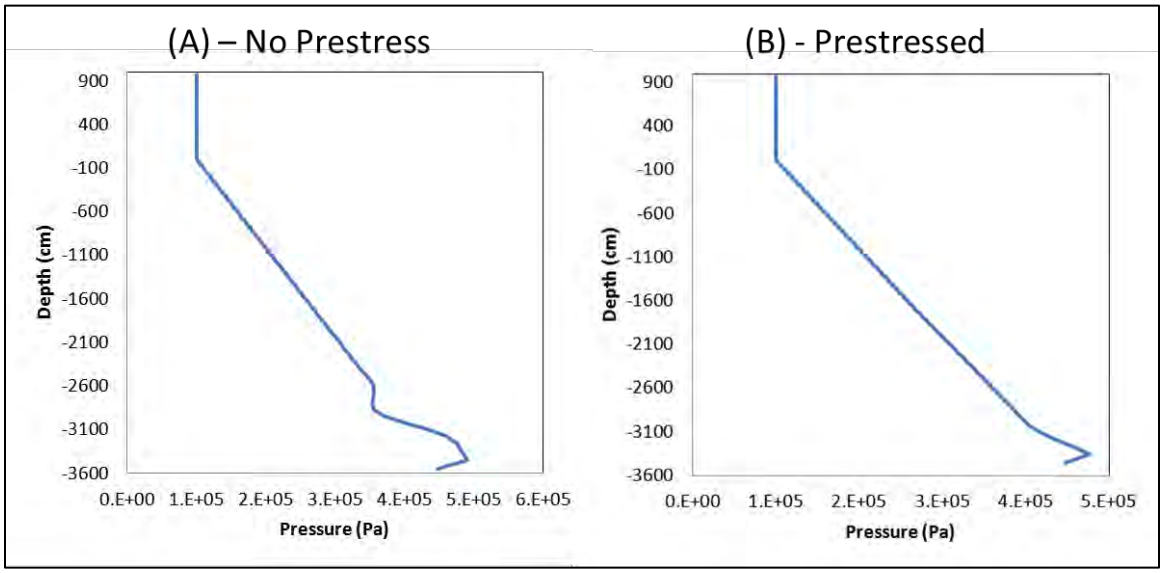

Figure 29. Effect of Dyna_N Prestress on Bottom Wave

4. Back Pressure Elimination

The remaining portion of the initial bottom wave in Figure 29(B) is due to the presence of back pressure on the singly-wetted interface. The back pressure is skewing the transient results in the same fashion in which it distorted the dynamic relaxation solution. There are two solutions to this problem. The simplest to apply is the elimination of back pressure in the Gemini input. This only requires the modification of a single line of code. A drawback occurs with the addition of a ship model. The FSP model was turned

into a singly-wetted interface by adding an artificial roof. This freed the user from establishing interfaces in the interior of the model. The elimination of the back pressure would necessitate a change in the ship model.

A second method to eliminate the back pressure is to apply a pressure that is of equal magnitude but opposite direction to the back pressure. This is done through the application of pressure loading on the interfaces, which is easily accomplished in the preprocessor. Conveniently, the pressure loading is applied on a separate input file from the nodal forces. This ensures there is no input conflict between the pressures and the nodal reaction forces. This method of back pressure elimination was applied to all further simulations.

5. Benefits of Decreased Bottom Thickness

The final recommendation on minimizing the bottom wave is to decrease the thickness of the model. The cause of the initial bottom wave was the movement of the top surface of the Lagrangian solid bottom. This is the byproduct of the structural volumetric strain due to the initial hydrostatic loading. While the hydrostatic pressure will always control the amount of strain, the range of the displacement of the structure can be minimized by decreasing the thickness of the structure. Thus the magnitude of the initial bottom wave is diminished. This concept was validated by running two sets of simulations in which the only variable was the thickness of the model. The first set used all of the parameters developed in this chapter. The only difference in the second set was that the Dyna_N Prestress inputs were not included. Figure 30 is a graph of the pressure

deviation from hydrostatic as a function of distance from the bottom for the first set of simulations. In both cases, three bottom thickness of two, five, and ten meters were applied. Figure 31 graphs the same results for the set without Dyna_N Prestress inputs. In all cases the individual element sizes were kept constant at one cubic meter.

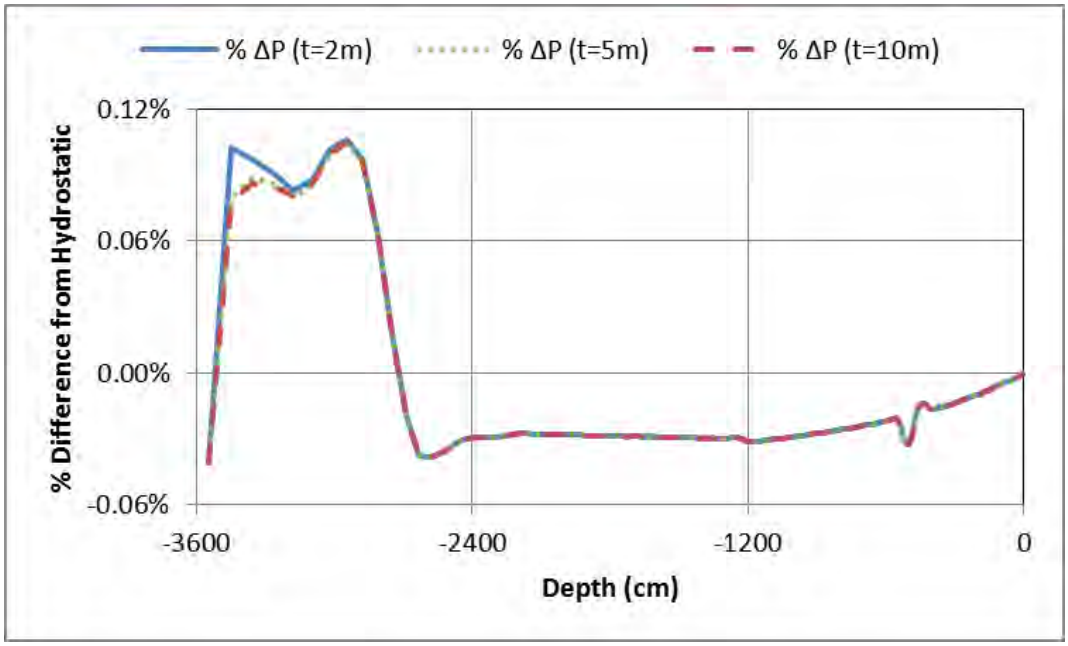

Figure 30. Effect of Bottom Thickness on Initial Bottom Wave with Dyna_N Prestress

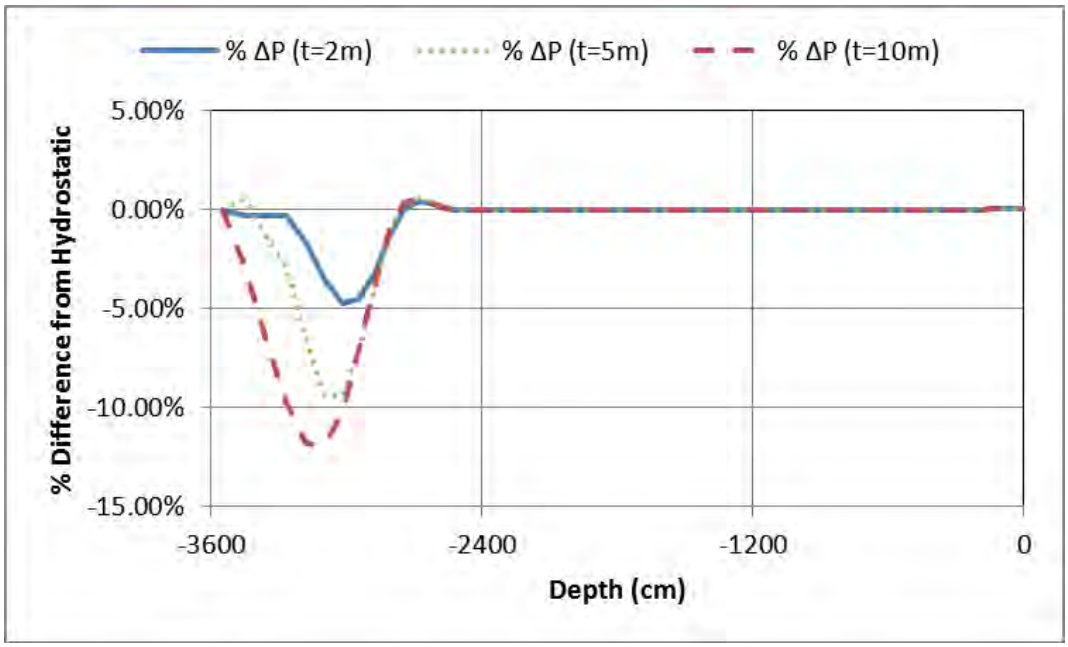

Figure 31. Effect of Bottom Thickness on Initial Bottom Wave without Dyna_N Prestress

From Figure 30, it is apparent that when the Dyna_N Prestress inputs are provided the initial bottom wave is only 0.1% greater than hydrostatic pressure. Therefore, the Lagrangian solid bottom can be made a thin as possible in order to minimize the number of elements and decrease the simulation time. Figure 31 highlights the benefit of minimizing the thickness when Dyna_N Prestress inputs cannot be provided. As the thickness decreases, the relative magnitude of the initial bottom wave is decreased.

D. RECOMMENDED METHOD FOR LAGRANGIAN SOLID BOTTOM MODELING

Constructing the Lagrangian solid bottom outside of the fluid domain, as diagrammed in Figure 13, encompasses most of the potential hurdles to implementing a Lagrangian solid bottom. With the correct application of initial and boundary conditions, this approach offers a more computationally efficient method of Lagrangian solid bottom modeling than completely containing the bottom within the fluid domain.

This chapter has explored several variations of initial and boundary conditions for the Lagrangian solid bottom model. The best combination of these parameters is listed in Table 15. The significant exception to this study is the material model used for to simulate the soil. A perfectly elastic material with parameters roughly similar to soil was utilized in order to minimize material model specific errors. Further research will be required to determine the best material model to use. The remainder of this parametric study in the effects of an explicitly modeled structural ocean floor on a shallow water UNDEX event will apply these parameters.

Table 15. Best Lagrangian Solid Bottom Modeling Parameters

Parameter	Best Choice
Lateral Dimension	Just greater than lateral dimensions of fluid domain.
Vertical Dimension	Thinner is more computationally efficient and required if use of Dyna_N Prestress inputs is not feasible.
Fluid-Soil Vertical Overlap	Overlap must be large enough to ensure that the vertical deformation of the Lagrangian solid bottom does not shift the water-soil interface out of the fluid domain.
Boundary Conditions	Nodal Forces that correspond to the reaction forces required for nodal displacement constraints on surfaces not interfaced with the fluid. Non-reflecting Boundary Segments on surfaces not interfaced with the fluid domain. Counter Pressure on the singly-wetted interfaces is necessary if the ship model utilizes singly-wetted interfaces as well.
Initial Condition	Dyna_N Prestress input for every solid element derived from the element stress tensors of the static solution, if and only if the material model used in the Lagrangian solid bottom is elastic or elastic plastic. Use restart file from a long-time, ramp loaded static simulation if the material model is not elastic or elastic-plastic.

V. COMPARISON OF LAGRANGIAN SOLID BOTTOM TO CURRENT BOTTOM MODELS

A. CURRENT MODELING METHODS AND LIMITATIONS

There are two currently accepted ways in which to model the ocean bottom in the DYSMAS software suite. All of these methods are implemented through the Eulerian fluid solver, Gemini. The first is the imposition of a perfectly reflective boundary condition on the fluid domain. The second is the use of a soil-like material layer at the bottom of the fluid domain. Both have their own unique limitations.

1. Wall Boundary Condition

The simplest method is to enforce a perfectly reflective, wall boundary condition on the bottom face of the fluid domain. The pre-process for this method is a simple one line input in the Pregemini input. When conducting simulations involving gravity, a wall boundary condition is already required in order to keep the water from draining out of the bottom of the fluid domain. The only boundary condition adjustment available is the modification of the amount of the reflection from zero to 100 percent of the incident pressure. While this option is the easiest to implement, the limitations are obvious. The wall condition acts as a perfectly rigid boundary, unlike a soil whose response to pressure loading can range from elastic to plastic. The creation of a three dimensional Cartesian fluid domain requires that the bottom surface be flat. This prevents this boundary condition from being able to form contoured bottom structures [18].

2. Euler EOS Material Layer

The bottom modeling method which is currently the accepted standard when using DYSMAS in a shallow water environment utilizes various Euler EOSs. During the creation of the fluid domain, in addition to air and water, a layer of soil is created at the bottom of the fluid domain. The EOSs for this soil are either a Mie-Grüneisen or a P-alpha form. The Mie-Grüneisen is an EOS relating the pressure, energy, and density of the material through the shock speed versus particle speed profile of the material. The P-alpha EOS combines the Mie-Grüneisen EOS with an air EOS in order to more accurately simulate a material with collapsible porosity [18]. This method of bottom modeling has been validated and used extensively in previous UNDEX simulations conducted in DYSMAS to date [8], [9], [10], [11]. While it is the standard, there are obvious drawbacks. As an Eulerian fluid, the soil material cannot support shearing forces, whereas actual soil does support shear loading. A new version of the Gemini code which allows for the application of a viscous fluid is in development, but was not available at the time of this research. Creating a contoured bottom using an Euler EOS is not accurate. The reason for this limitation is explained further in Chapter VI.

B. COMPARISON OF BOTTOM MODELING METHODS

A set of simulations were conducted to compare the effects that each accepted bottom modeling method and the Lagrangian solid bottom method developed in Chapter IV had on the fluid domain. Each simulation used the standard charge size and FSP placement location from Chapter III.

The first simulation utilized a Gemini wall boundary condition with a 100 percent reflection. The second bottom model was a Mie-Grüneisen EOS for a clay soil. This soil layer was five meters thick, with a wall boundary condition applied on the underside of the soil. The final model was generated from the best practices developed in Chapter IV. The model was five meters thick and consisted of an elastic material model whose properties were consistent with a clay soil provided by Bangash [23]. While the FSP was included in each simulation, this initial comparison was solely focused on the fluid domain response to each model. Each simulation was run out to one second.

1. Effect on Initial Bottom Reflection

The first comparison point was taken at 35 milliseconds after the charge was detonated. Figures 32 thru 34 represent the pressure distribution through the water column for the wall condition, Euler soil, and Lagrangian solid bottom models respectively. This particular time was chosen because it captures the entire bottom reflection response of each model prior to the reflected shockwave impacting the bulk cavitation zone (seen in white). The black line across the bottom of the plot in Figure 33 is interface between the water and the Euler soil. A similar line in Figure 34 is the interface between the water and Lagrangian solid bottom. Of significance in Figure 33 is the presence of a double reflection. The pressure wave closest to the surface is the true bottom reflection. The second reflection is a result of the wall condition placed beneath the soil layer. In all

cases the timing of the initial bottom reflection appears to be consistent. None of the models appears to delay the reflection.

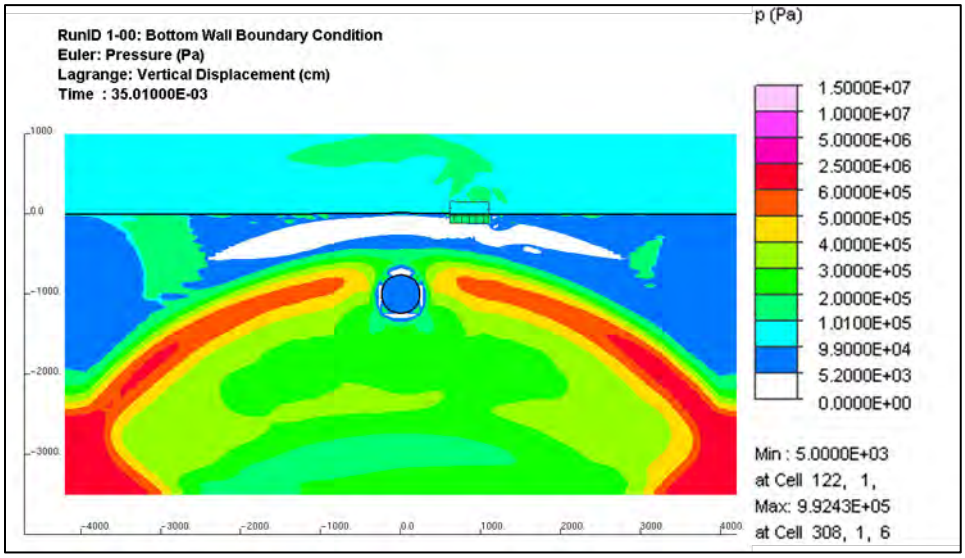

Figure 32. Pressure at 35 msec for a wall boundary

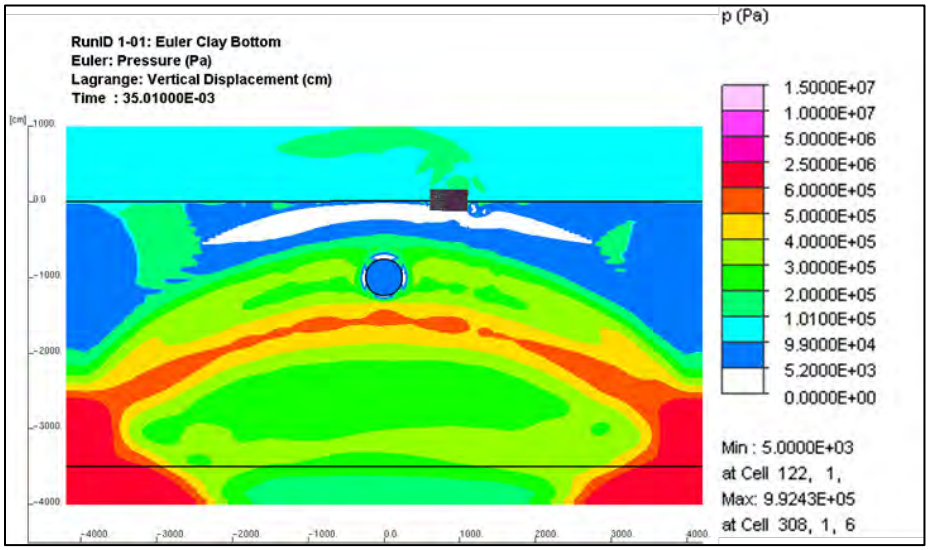

Figure 33. Pressure at 35 msec for an Euler soil

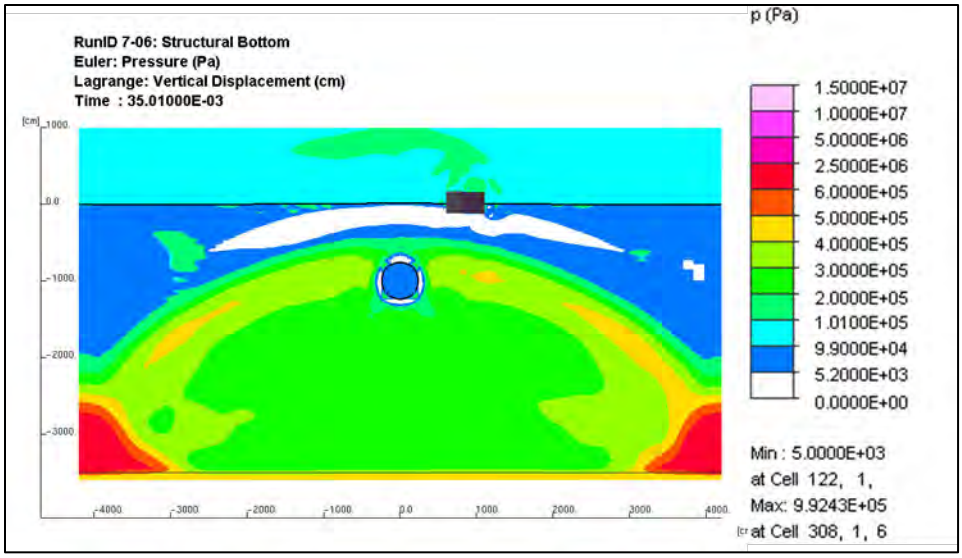

Figure 34. Pressure at 35 msec for Solid Bottom

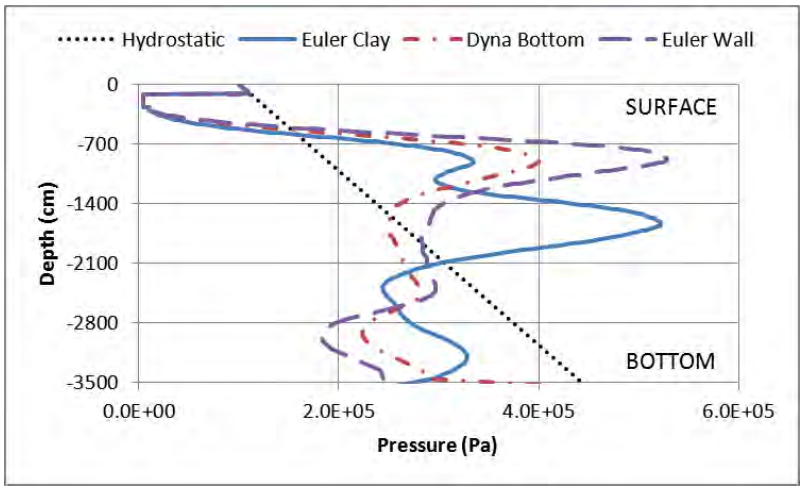

Figure 35. Bottom Reflection Pressure Comparison

A more accurate comparison was drawn by plotting the pressure versus depth at 35 milliseconds for all three cases in Figure 35. Of note is the clear correlation in shape between the wall boundary condition and the Lagrangian solid bottom. The only difference between the two appears to be the magnitude of the reflected pressures. The Euler soil looks to follow the same pattern from the surface to -1000 centimeters. At that point the response

becomes skewed by the second reflection. The influence of the second reflection can be reduced to negligible values with an increase in thickness of the Euler clay layer [32]. This reduction would come at the cost of increased computational resources. Comparing the magnitudes of the initial reflections, the wall condition provides the greatest reflection and the Euler soil provides the least. The elastic material model used in the Lagrangian solid bottom could be adjusted in order to reflect a pressure wave of equal magnitude to that of the Euler soil. Replacing the elastic material with a more representative soil model could also improve upon this response.

2. Effect on Gas Bubble

The bottom model type also affected the bubble response. Table 16 compares the response of each simulation's bubble and associated first pulse. Once again the Lagrangian solid bottom closely follows the wall boundary condition in all areas. The significant outlier is the incident pressure of the Euler soil's first pulse, which is nearly double the incident pressure of the other two models.

Table 16. Max Radius and First Pulse Comparison

Model	Max Bubble Radius (cm)	1^{st} Pulse on FSP (msec)	1^{st} Pulse Pressure (Pa)
Empirical	418	552	N/A
Wall B.C. (Run 1-00)	475	563	6×10^5
Euler Soil (Run 1-01)	482	576	12×10^5
Lag. Solid Bottom (Run 7-06)	475	563	7×10^5

VI. EFFECT OF BOTTOM CONTOURS ON UNDEX EVENT

Modeling the bottom as a structure in Dyna_N provides the capability to create bottoms which are not flat. When modeling the bottom in Gemini, it is not possible to establish three dimensional bottom shapes that are in equilibrium. It is possible to fill an arbitrary shape in the Euler grid with a soil material. Two limitations prohibit the soil from staying in the arbitrary shape. The first is the density mismatch between the soil and water EOS. Since the soil is treated as an inviscid Eulerian fluid, over time the denser soil will settle to the bottom of the fluid geometry. Several simulations without explosive charges were run to determine if this effect was visible. After only 100 milliseconds, the soil was observed to be settling in Figure 36. The left side of Figure 36 is the density profile for the domain. The right side of Figure 36 is the vertical velocity profile at 100 milliseconds. The blue region indicates that the soil columns are moving down at a rate of nearly two centimeters per second. The pink region is water moving upward at two centimeters per second. The actual displacement over the course of one second is negligible to the overall geometry. The root cause of this movement is an uneven pressure distribution through the fluid domain. This pressure distortion has severe consequences for the simulation and cannot be avoided when using Euler soil.

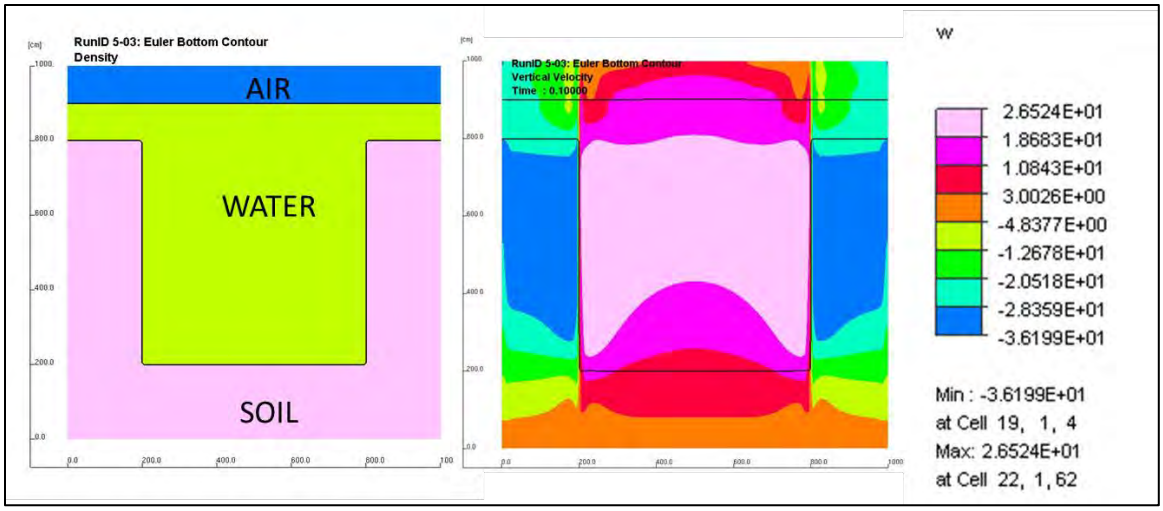

Figure 36. Density and Vertical Velocity Profile of Euler Contoured Bottom

In order to create a three dimensional bottom in Gemini, the user must utilize the BODYFILL command. BODYFILL allows the user to fill an arbitrary shape in the fluid domain with a given material [18]. Once the shape has been filled, Gemini applies gravitational forces to the filled material. The complication is that Gemini cannot equalize the pressure in the fluid domain with the filled shape. This results in the fluid domain pressure distribution depicted in Figure 37. The pressure gradient in the soil is much greater than the water due to the difference in density. The pressure mismatch on the vertical faces and at the bottom of the channel creates considerably large pressure waves when the simulation begins. Just as the initial bottom wave in Section IV.C distorts the explosive shockwave, so too does this pressure mismatch. Unlike the Lagrangian solid bottom, there is no method to correct this distortion in the Eulerian solver.

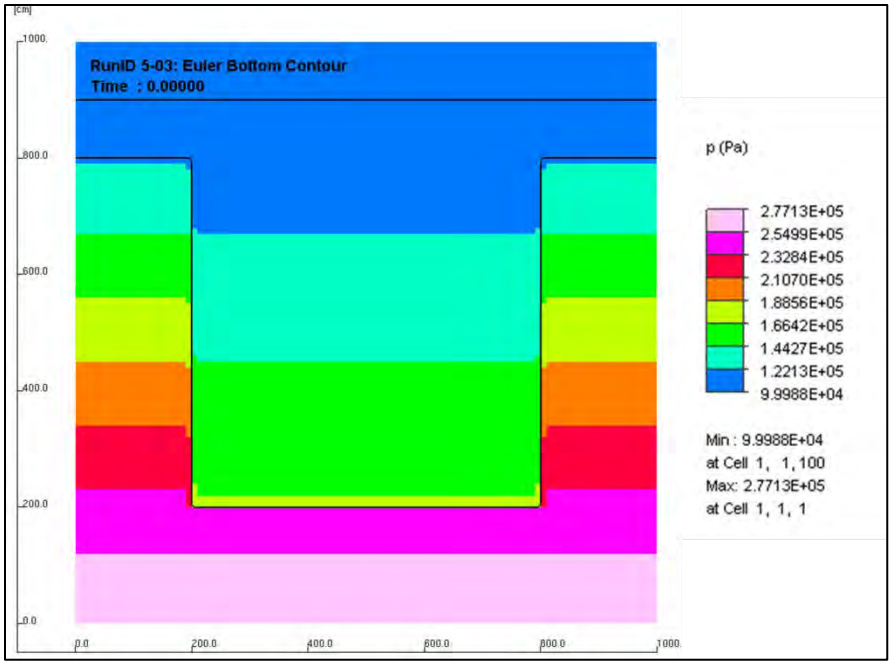

Figure 37. Pressure Gradient in Euler Contoured Bottom

In Chapter IV, this thesis explored the various methods, distortions, and corrections involved in modeling the ocean floor as a flat Lagrangian solid bottom in Dyna_N. This method of bottom modeling has a distinct advantage over Gemini in that the application of a contoured Lagrangian solid bottom model is has no difference from that of a flat solid bottom. In most deep water UNDEX events the contour of the ocean bottom is trivial as the bottom reflection of the shockwave is of minimal magnitude. This assumption is not true for littoral waters. The ability to model contoured shallow water environments could prove vital in determining the true nature of UNDEX effects on ships operating in these waters. With this in mind, five different bottom contours and one flat bottom model were developed and simulated with the FSP

serving as the ship model. The goal was to determine the effect which bottom geometry had upon the response of both the fluid domain and the FSP.

A. DESCRIPTION OF BOTTOM SHAPES

The profiles of each of the bottom contours used are displayed in Figure 38. Table 17 contains the values of the variables referenced in Figure 38. In all cases the standard charge of 60 pounds of HBX-1 at a depth of ten meters was placed with six meters of lateral separation from the FSP. As discussed in Section III.E, the dimensions of the fluid domain were 84 meters in both the X and Y directions with the charge placed in the center. The depth of the fluid extended to one meter beyond the lowest point of the water-soil interface for each contoured model. Every simulation was run out to a full second to ensure that the response beyond the first bubble pulse was captured.

Table 17. Values of Contoured Bottom Shapes

Figure	X1 (m)	X2 (m)	Y (m)	Z1 (m)	Z2 (m)	Z3 (m)
A: Deep V	42.01	42.01	84.02	25.00	20.00	5.00
B: Inv. V	42.01	42.01	84.02	25.00	20.00	5.00
C: U Channel	21.01	42.01	84.02	10.00	25.00	5.00
D: Ramped	84.02	N/A	84.02	25.00	20.00	5.00
E: Anechoic	84.00	N/A	84.00	30.00	10.00	5.00
F: Flat	84.02	N/A	84.02	35.00	5.00	N/A

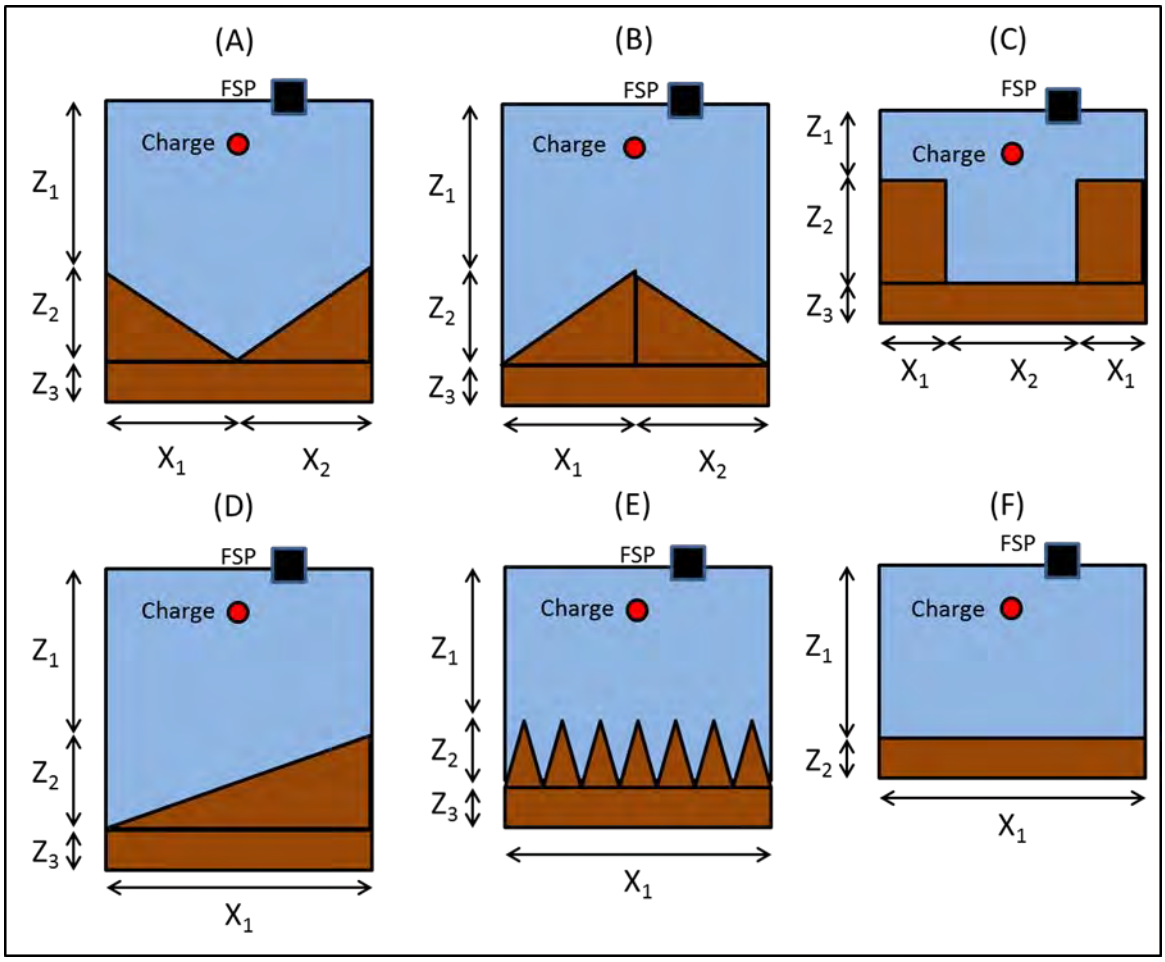

Figure 38. Profile Views of Contoured Bottoms

B. BOTTOM CONTOUR EFFECT ON FSP RESPONSE

The first point of comparison between the six bottom types is the vertical velocity response of the closest point of the FSP for the first 800 milliseconds in Figure 39. The velocity response has been filtered to eliminate the all of the response data which had a frequency greater than 250 Hz. Initially the velocities rise sharply as the initial shockwave impacts the FSP. After approximately 50 milliseconds the initial transient response subsides, resulting in a velocity which steadily decreases. Near 550 milliseconds, the first bubble pulse impacts the structure

causing a sharp increase in vertical velocity. This trend is expected in nearly all surface ship responses to UNDEX events. On the whole, every bottom contour causes a nearly similar FSP response. The lone exception is the anechoic pyramid bottom that demonstrates a vertical velocity noticeably lower than the rest.

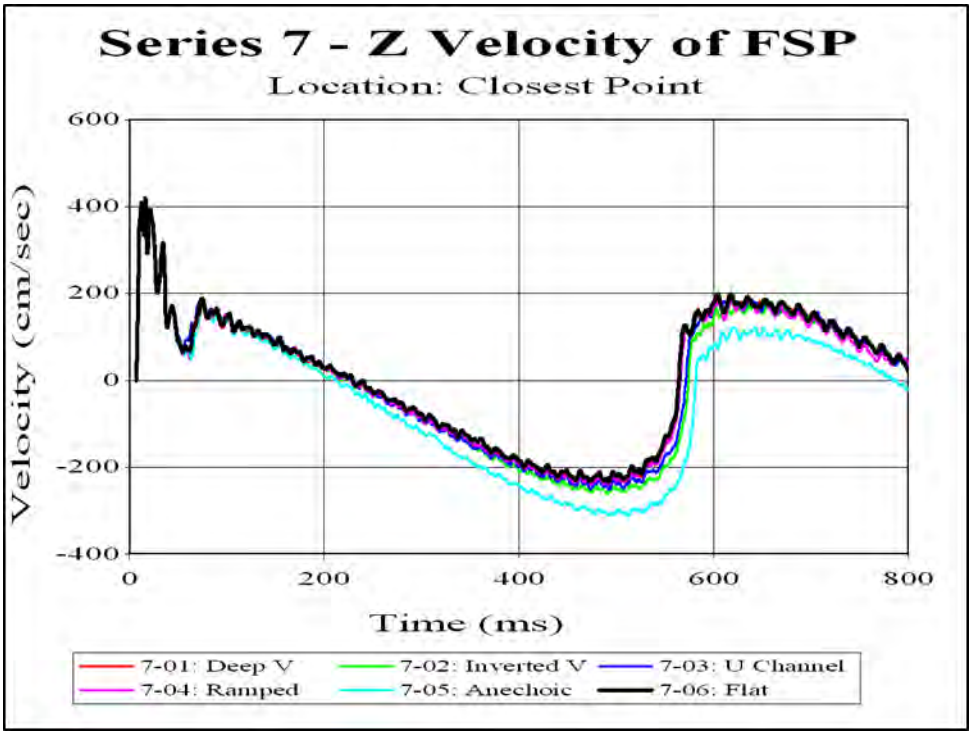

Figure 39. Velocity Response of FSP Closest Point to Charge for Each Contoured Bottom (0-800msec)

The primary concern in all of the simulations is the effect that the bottom reflection has upon the FSP. In all six cases, the bottom reflection should reach the FSP within the first 50 milliseconds. With this in mind, a closer examination was conducted of the early vertical velocity time-history in Figure 40. The initial velocity responses are identical in all cases for the first 50 milliseconds. Thus the bottom reflections in all cases

appear to have very little effect on the initial velocity response of the FSP. Even after 50 milliseconds the responses show very little separation.

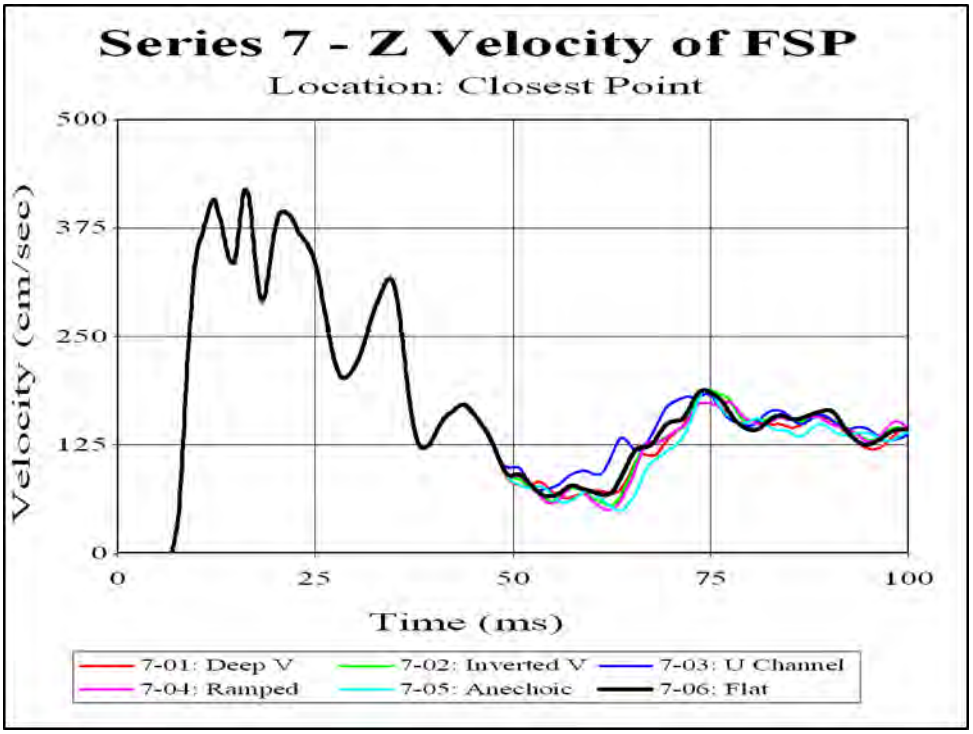

Figure 40. Velocity Response of FSP Closest Point to Charge for Each Contoured Bottom (0-100msec)

The lack of velocity differences indicates that there must be only minor differences in the incident pressure the FSP feels in all cases. Before examining the pressure history of the fluid below the FSP, a brief understanding of the entire pressure history response is required. Figure 41 shows the pressure time history for the first second of the UNDEX simulation and is representative of nearly every UNDEX event. Initially, there is a large pressure rise from the initial shockwave. Assuming a bulk cavitation zone forms, when the cavitation zone collapses it emits a smaller pressure wave known as the cavitation closure. This

normally occurs within the first hundred milliseconds. All of the subsequent pressure spikes are a result of bubble pulses.

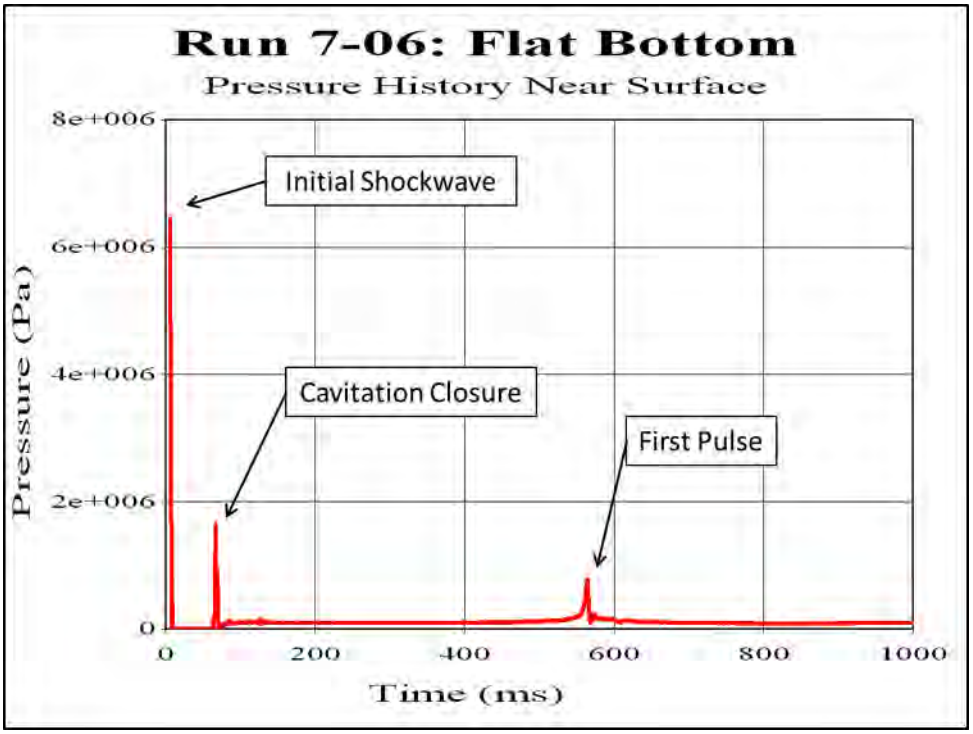

Figure 41. Example UNDEX Pressure History

The pressure time histories for a point directly below the center of the FSP for all cases was plotted in Figure 42 for the first hundred milliseconds of the simulation. Indeed, there are no outliers in the pressure data. All of the cases followed the same pressure time history until approximately 45 milliseconds, before they began to diverge. Even after 45 milliseconds, the differences were only minimal and contained no spikes in the pressure.

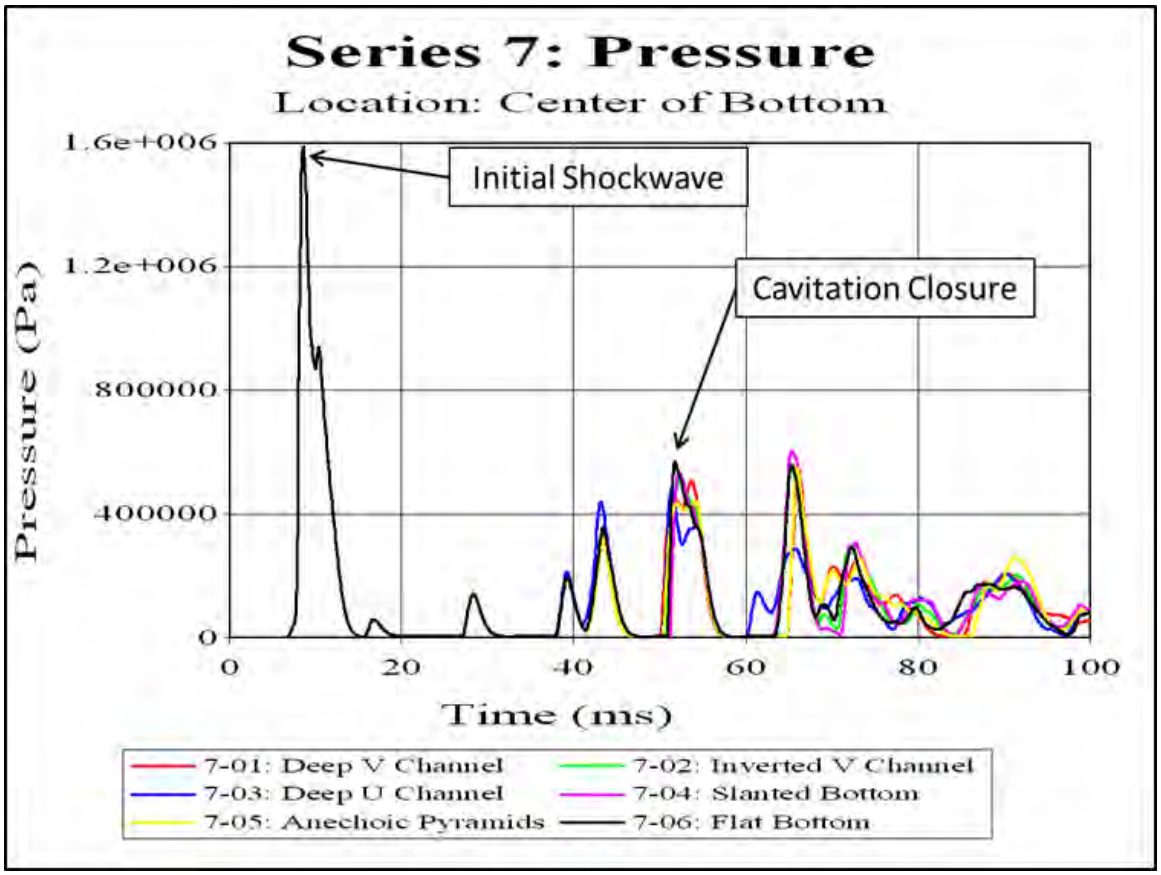

Figure 42. Bottom Contour Effect on Pressure Directly Beneath FSP

While it appears from the analysis of the FSP response that the bottom contour has little effect, further investigation of the fluid domain response highlighted the differences and provided an explanation for its lack of effects on the FSP.

C. BOTTOM CONTOUR EFFECT ON FLUID DOMAIN AND BUBBLE DYNAMICS

The lack of pressure and velocity differences directly below the FSP between the different bottom contours does not imply that there were no differences in the fluid domain response. A study of the pressure history at a point

five meters beneath the FSP was conducted. Figure 43 is focused on the time period of the initial shockwave propagation. Figure 44 is centered on the first bubble pulse response.

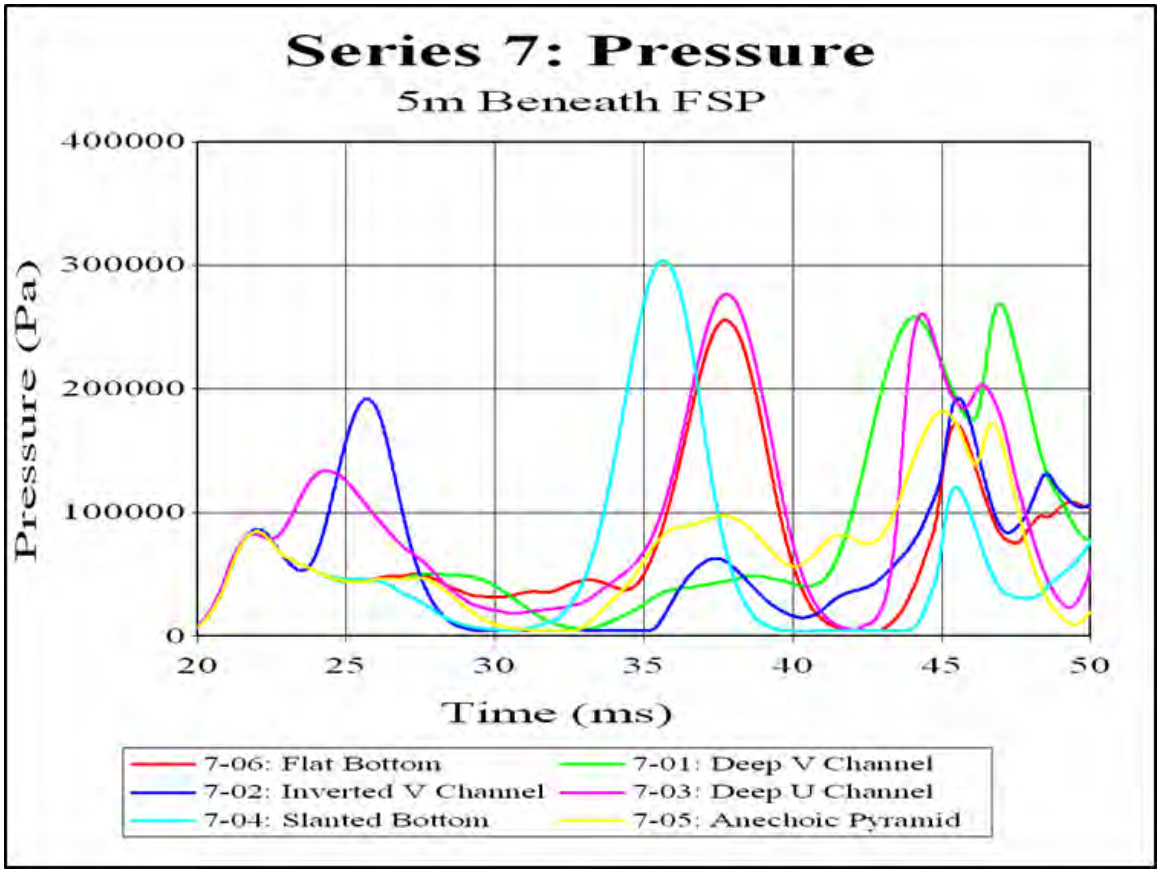

Figure 43. Bottom Contour Effect on Pressure 5m Below FSP (20-50msec)

The two most similar responses are the flat bottom (7-06) and the Deep U Channel (7-03). These two contours provided nearly identical bottom reflections of 2.7 x 10^5 Pa at 37.5 milliseconds. This is expected since the point of reflection on the bottom in both cases was at the same depth and same zero inclination. The Slanted bottom (7-04) reflection returned slightly earlier at 36 milliseconds with a greater magnitude of 3 x 10^5 Pa. As the point of

reflection in this case was slightly shallower than the flat bottom, the reflection should be sooner and of greater magnitude. This same principle applies for the Deep V Channel (7-01), where the point of reflection is at a greater depth. As expected the reflection was delayed. Its pressure should have been smaller than the flat bottom, but was of equal magnitude instead. The Inverted V Channel (7-02) had the shallowest reflection point and returned the reflection the quickest at 26 milliseconds. Unexpectedly, even with the shortest distance to travel, the Inverted V Channel gave the second lowest pressure magnitude. Lastly, the Anechoic Pyramid bottom returns the smallest reflection wave, whose magnitude is less than hydrostatic pressure. The lack of a bottom reflection of significance explains why this simulation had the lowest vertical velocity through the simulation in Figure 39.

The pressure peaks from 45 to 50 milliseconds were verified to be the result of cavitation closure with the exception of the Deep V Channel bottom reflection at 44 milliseconds. The pressure peak in the Deep U Channel response at 24 milliseconds is the shockwave reflection from the vertical face of the channel. Its motion was primarily horizontal and did not propagate towards the FSP.

The fluid domain analysis additionally examined the differences in the first bubble pulse due to the bottom contour. The resulting pressure histories are shown in Figure 44. While the magnitude appears unaffected, the timing of the pulse shows significant differences for the various contours. Once again, the two contours that showed the most significant difference from the flat bottom were

the Anechoic Pyramids (7-05) and the Inverted V Channel (7-02). These differences in pulse timing can have significant impact on the total effect of a charge on a target. The majority of UNDEX weapons are designed such that their bubble pulses are timed to excite the natural bending frequency of the ship thereby causing resonance and increased damage [21]. While the variation in frequency of the bubble response of a 60 pound charge is small due to the bottom contour, most UNDEX threats are one or two orders of magnitude larger which have the potential for a wider variation in pulse frequency.

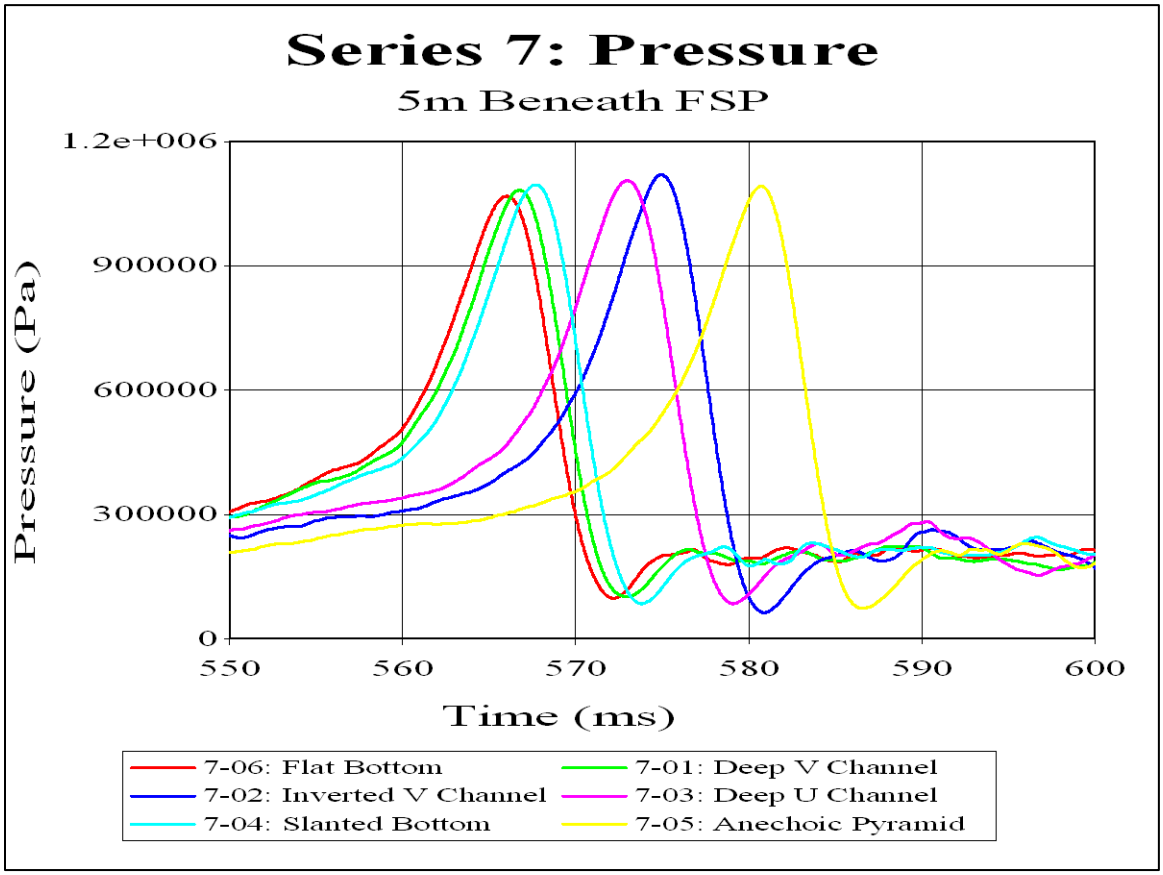

Figure 44. Bottom Contour Effect on Pressure 5m Below FSP (550-600msec)

Table 18. Contoured Bottom Effect Characterization at 5m below FSP

	Initial Bottom Reflection		1st Bubble Pulse		
Contour (Run #)	Pressure (% of Max)	Path Distance (cm)	Pressure (Pa)	Arrival Time (msec)	Frequency (Hz)
Flat Bottom (7-06)	12.6	7037	1.07E+06	566	1.77
Deep V Channel (7-01)	12.6	8620	1.08E+06	567	1.76
Inverted V Channel (7-02)	9.2	5460	1.12E+06	575	1.74
Deep U Channel (7-03)	13.6	7037	1.11E+06	573	1.75
Slanted Bottom (7-04)	14.6	6835	1.10E+06	568	1.76
Anechoic Pyramids (7-05)	4.9	7037	1.09E+06	581	1.72

The findings in this section have been summarized in Table 18. For the initial bottom reflection the pressure is given as a percentage of the maximum shockwave pressure that the test point received from the initial blast. The path distance is the length of the bottom reflection propagation path. The second section of the table includes the pertinent data regarding the first bubble pulse.

D. INDIVIDUAL BOTTOM CONTOUR ANALYSIS

This section investigates each bottom contour response individually to determine why the initial FSP response is unaffected by the bottom contours that have been shown to significantly affect the fluid domain.

1. Flat Bottom

Examining Figure 45, a clear picture of the bottom reflection along with the bulk cavitation zone at 28 milliseconds is formed. A black dashed contour line was added to the figure to highlight the wave front. The bottom reflection should have impacted the FSP at approximately 40 milliseconds. Figure 46 shows that this is not the case and provides a better understanding of why the bottom reflection has little effect on the FSP initially. As the bottom reflection travelled vertically through the water column, it impacted the existing bulk cavitation zone. Recall that bulk cavitation is created when a compressive wave is incident on a free surface. Here the low pressure bulk cavitation zone serves as the free surface for the bottom reflection. The result is the formation of a second cavitation zone beneath the first. This indicates that the bulk cavitation zone acts as a buffer for the FSP.

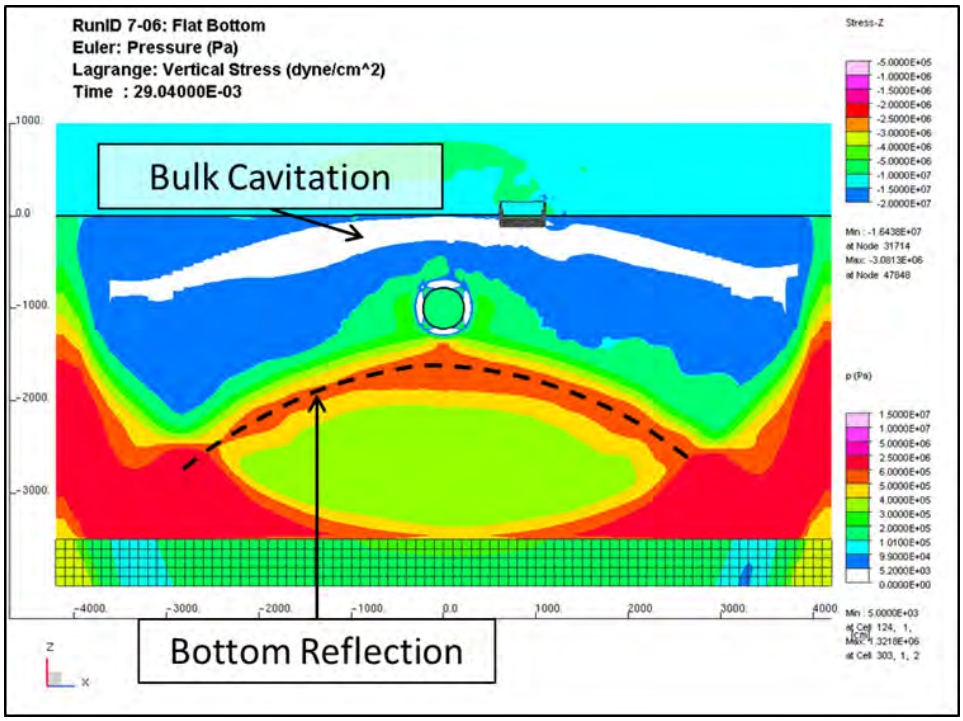

Figure 45. Pressure Distribution for Run 7-06: Flat Bottom at 29 msec

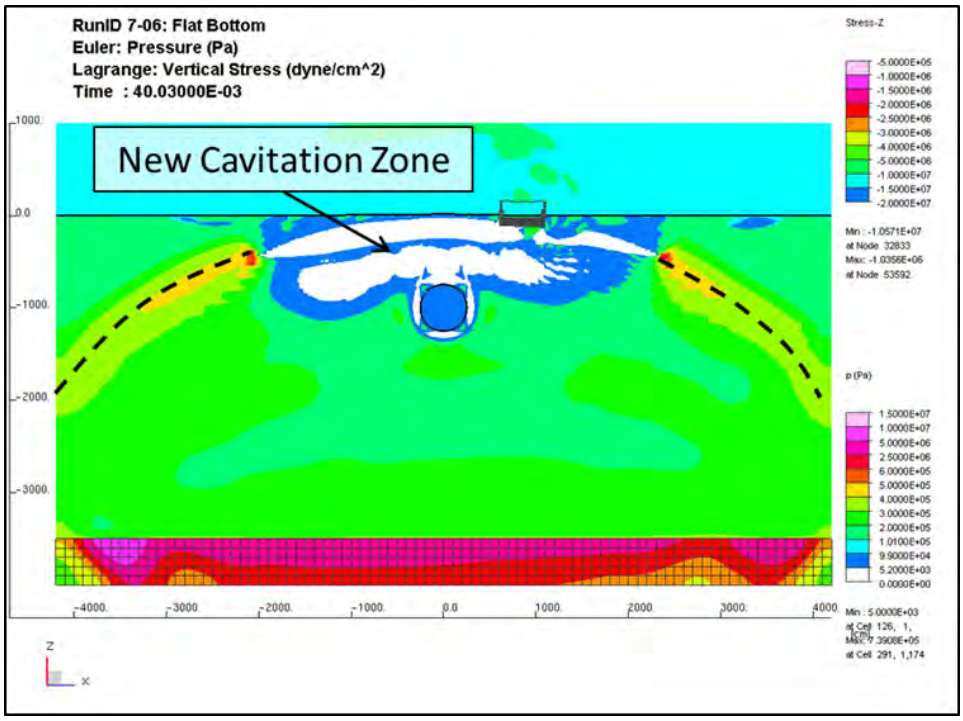

Figure 46. Pressure Distribution for Run 7-06: Flat Bottom at 40 msec

2. Deep V Channel

The fluid response at 32 milliseconds in the Deep V Channel showed significant differences from the flat bottom. In this case the contour created two bottom reflections seen in Figure 47. At the convergence of these two reflections, a vertically-moving, high pressure zone formed. Due to the symmetry of the bottom contour about the charge location, this high pressure zone collided with the gas bubble in Figure 48, which dissipated its energy, and did not immediately affect the FSP. In this case there is no evidence of a second bulk cavitation zone forming.

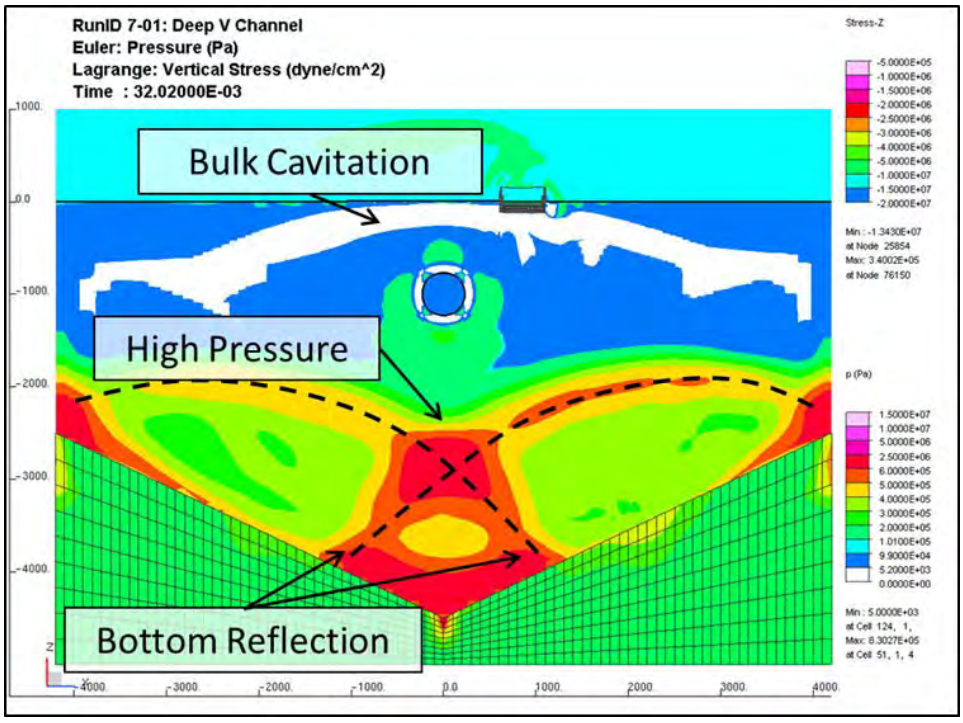

Figure 47. Pressure Distribution for Run 7-01: Deep V Channel at 32 msec

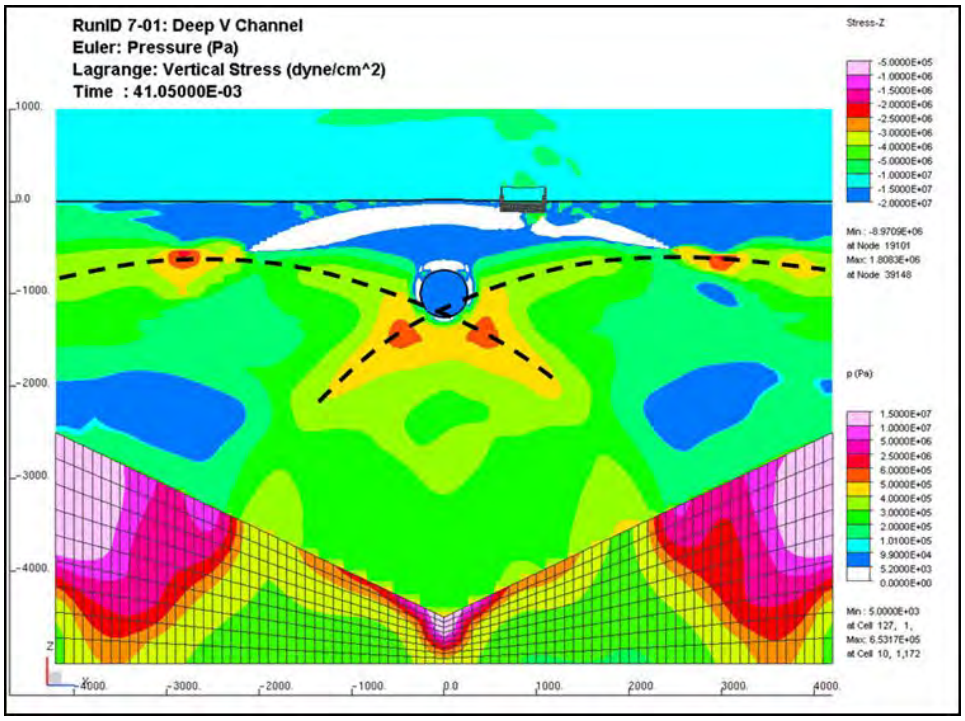

Figure 48. Pressure Distribution for Run 7-01: Deep V Channel at 41 msec

3. Inverted V Channel

Unlike the Deep V Channel where high pressure convergence zones were created, the Inverted V Channel causes the bottom reflection in Figure 49 to spread after only 20 milliseconds. The dispersion of the bottom reflection helps explain the reduced pressure noted in Figure 43. Once again, a new bulk cavitation zone is observed after the bottom reflection is incident on the original cavitation zone in Figure 50.

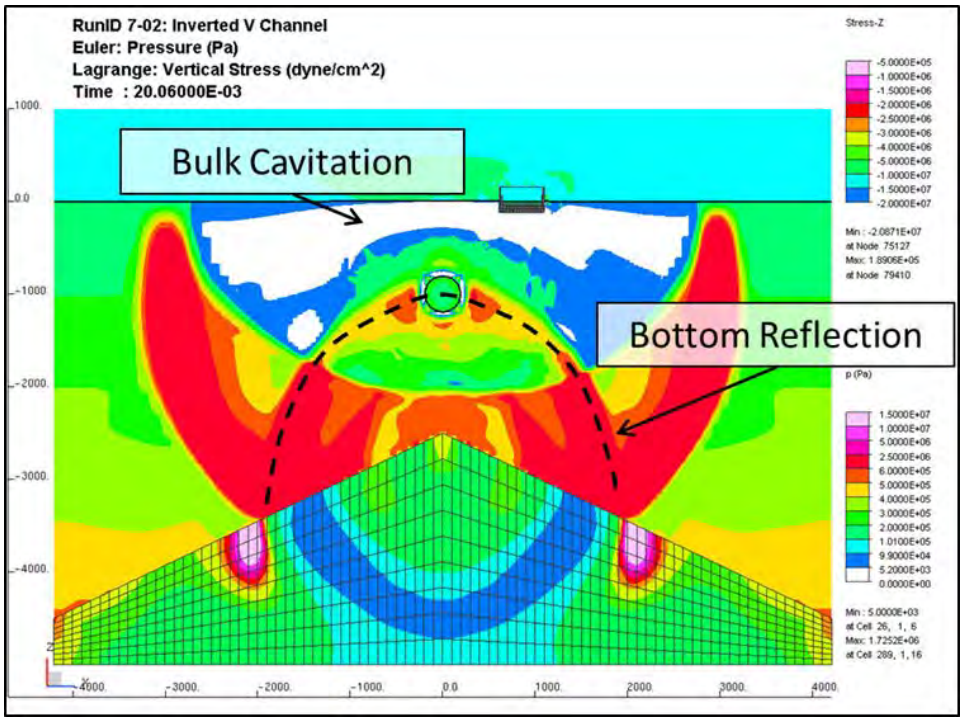

Figure 49. Pressure Distribution for Run 7-02: Inverted V Channel at 20 msec

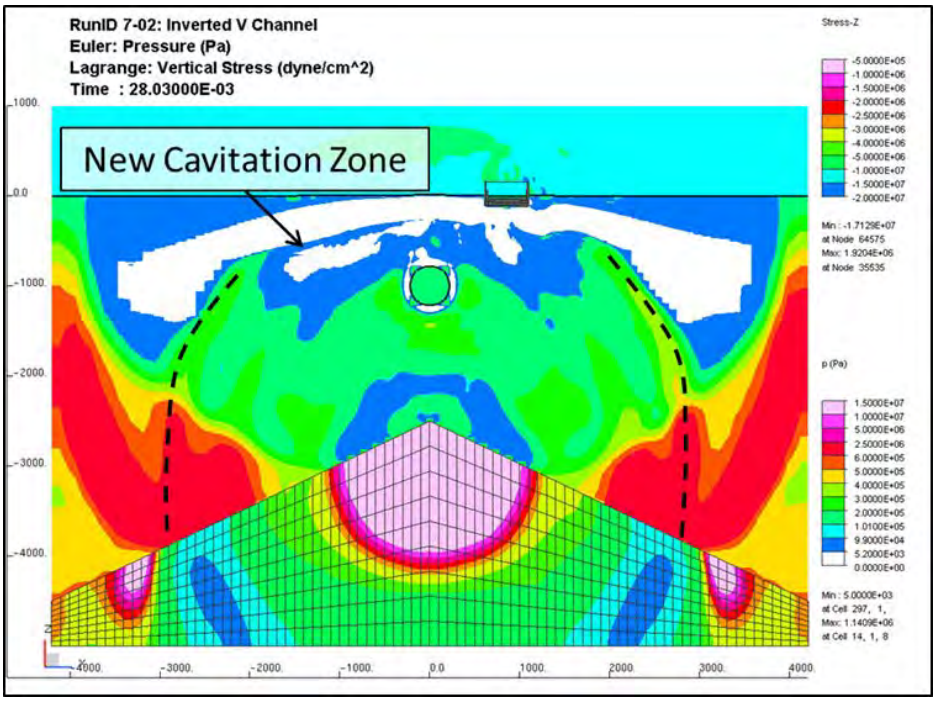

Figure 50. Pressure Distribution for Run 7-02: Inverted V Channel at 28 msec

4. Deep U Channel

The pressure contour plot for the Deep U Channel at 25 milliseconds is provided in Figure 51. The view of the bottom reflection is ambiguous due to the presence of reflections from the vertical sidewalls. Unlike the previous three cases where the bulk cavitation zone acted as a buffer, it appears in Figure 52, that the cavitation zone disappeared just prior to or as a result of the bottom reflection. This allowed an increase in pressure, shown in green, to be seen just below the hull of the FSP. Though it is present, this pressure is less than twice the value of hydrostatic pressure.

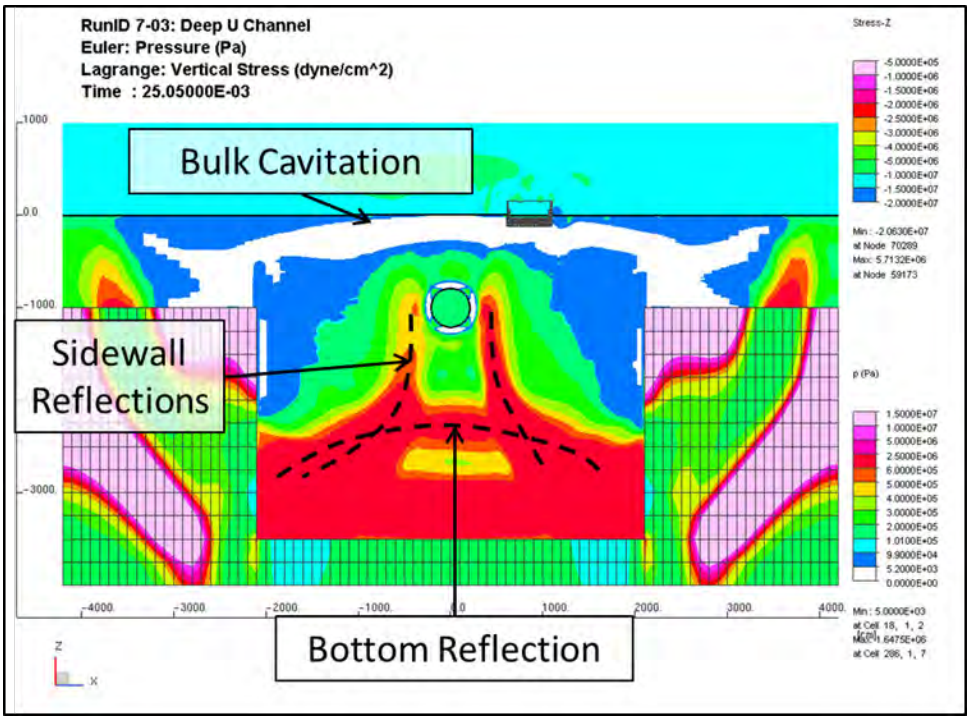

Figure 51. Pressure Distribution for Run 7-03: Deep U Channel at 25msec

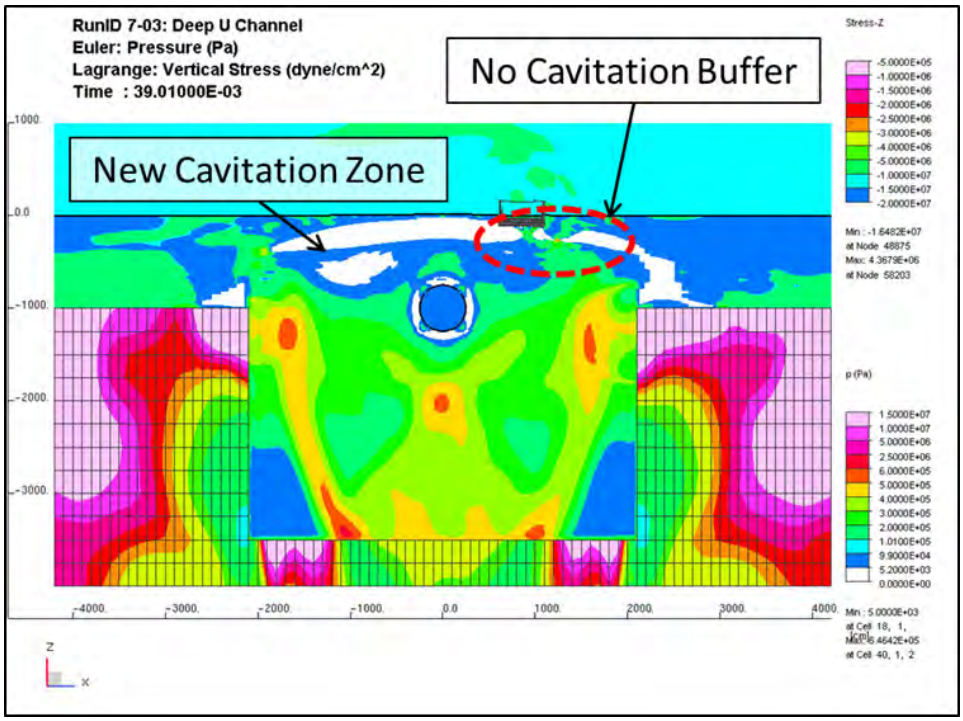

Figure 52. Pressure Distribution for Run 7-03: Deep U Channel at 39 msec

5. Slanted Bottom

Figure 53 is the pressure contour response for the Slanted Bottom simulation at 28 milliseconds. The bottom reflection looks similar to that of the flat bottom with no areas of convergence or dispersion. In Figure 54, the formation of a second bulk cavitation zone indicates that the bottom reflection does not impact the FSP.

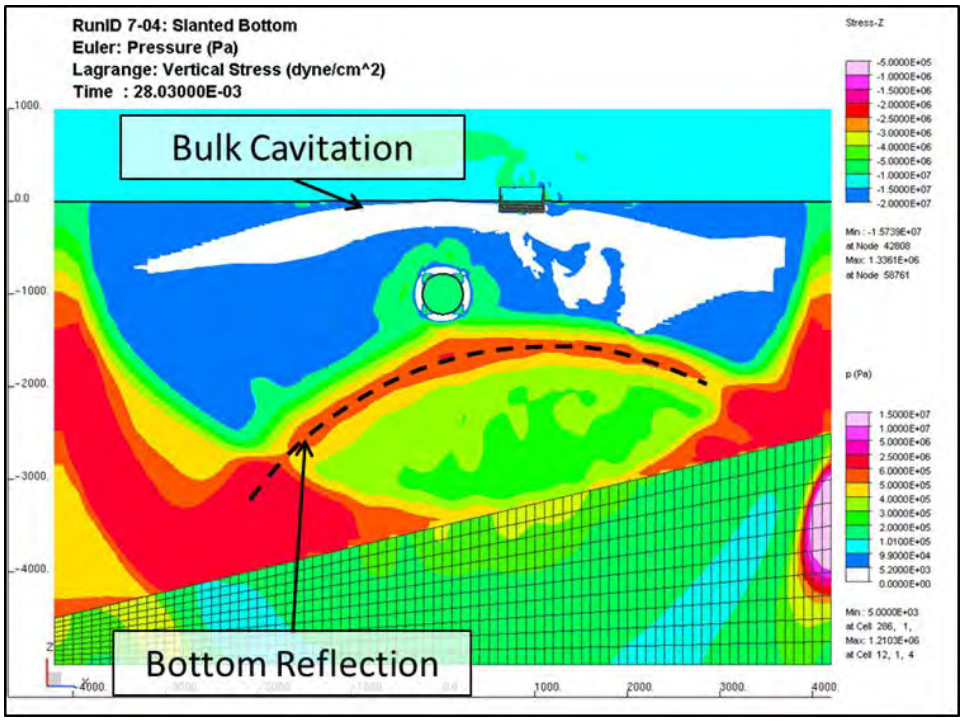

Figure 53. Pressure Distribution for Run 7-04: Slanted Bottom at 28 msec

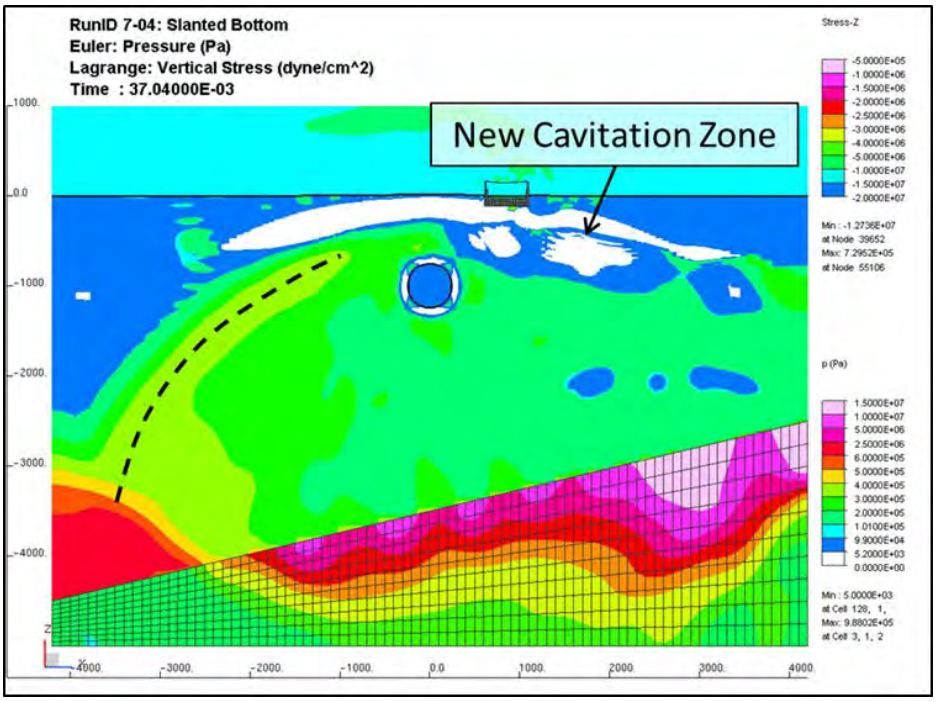

Figure 54. Pressure Distribution for Run 7-04: Slanted Bottom at 37 msec

6. Anechoic Pyramids

The purpose of an anechoic surface is to minimize or eliminate reflections. The use of a bottom contour of anechoic pyramids accomplished this function. Figure 55 highlights that the bottom reflections created by the anechoic surface were weak and scattered. By 40 milliseconds in Figure 56, there are no distinct pressure waves remaining in the fluid domain. This corresponds well to the minimal pressure wave response that was noted in Figure 43.

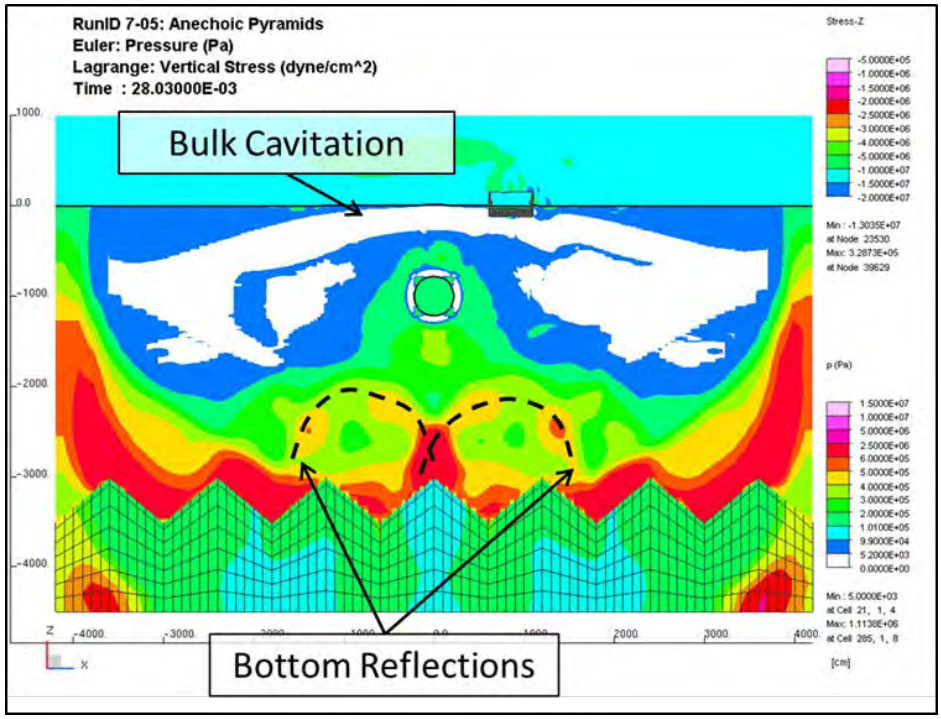

Figure 55. Pressure Distribution for Run 7-05: Anechoic Pyramids at 28 msec

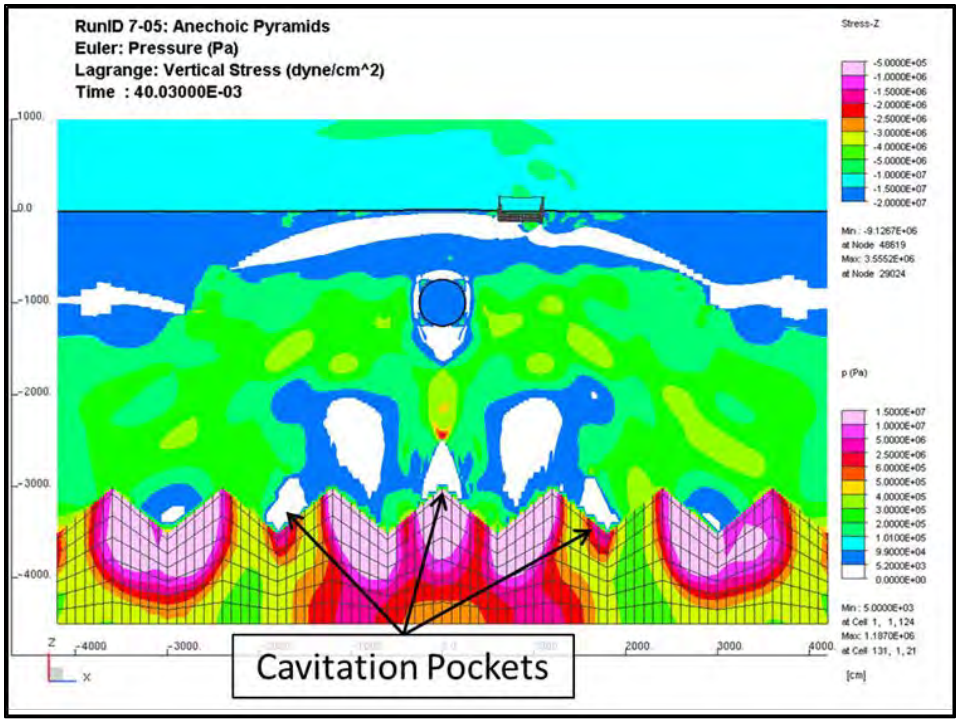

Figure 56. Pressure Distribution for Run 7-05: Anechoic Pyramids at 40 msec

The anechoic surface demonstrates a unique fluid response where pockets of cavitation form at the water-soil interface. A review of the animated pressure contour response shows that over time these cavitation pockets migrate from the bottom upward around the bubble. These low pressure cavitation zones do not slow the bubble expansion at the same rate as the normal fluid domain. This allows the bubble to expand over a longer time, thereby delaying the first pulse.

E. BULK CAVITATION AS A BUFFER ZONE

It is now clear that the lack of initial FSP response to the different bottom contours was due to the buffer provided by the bulk cavitation zone. This effect is strictly a by-product of this particular simulation

geometry, upon which every simulation was based. The charge weight, depth, target, and lateral separation between the two were chosen to mimic the MIL-S-901D testing that utilizes the FSP as a shock test platform for shipboard equipment [5]. The chosen bottom depth was an average of several shallow water environments.

Several factors can be varied in order to diminish the buffer effect of the bulk cavitation zone. As noted in Figure 43, the cavitation closure for this particular charge occurs at approximately 50 milliseconds. An increase in bottom depth would allow the bottom reflection to return to the surface after the cavitation zone closed. Thus the bottom reflection would reload the structure. The draft of the FSP is only 1.2 meters. If the Littoral Combat Ship (LCS) with a draft of 4.5 meters were used the keel would be below the buffer zone. A lateral shift of the target to a point outside the bulk cavitation zone, it would feel the full effect of the bottom reflection no matter the ocean depth. As charge size and depth increase, the lateral extent of the bulk cavitation zone does as well to a point. Lastly, while the cavitation zone acted as a buffer for the bottom reflection of a 60 pound charge, a larger charge with a larger bottom reflection might be able to collapse the bulk cavitation zone and still be energetic enough to significantly impact the FSP.

VII. FINAL REMARKS

A. CONCLUSIONS

A method to model the ocean bottom as a Lagrangian solid was developed for comparison to the current Euler fluid bottom modeling approaches. Several sets of boundary and initial conditions were simulated to determine which combination introduced the least artificiality to the fluid domain solution. If an elastic or elasto-plastic model was used, it was then possible to apply non-reflecting boundary segments and nodal reaction forces at the boundaries along with Dyna_N Prestress. The non-reflecting boundary segments allowed the Lagrangian solid bottom to act as a semi-infinite domain, thereby eliminating retransmission waves. The Dyna_N Prestress imposed the hydrostatic loading and deformation on the bottom in order to minimize the magnitude of the initial bottom wave. This combination provided an accurate and efficient solution. However, the non-reflecting boundary segments and Dyna_N Prestress have limitations that prohibit their application to more complicated soil material models.

The validation of the Lagrangian solid bottom model was completed by comparing its fluid domain response to two existing bottom modeling methods. The first bottom modeling method was a purely reflective Eulerian boundary condition. The second method was the use of an Eulerian equation of state for a generic clay soil. The simulation geometry was consistent with the MIL-S-901D shock testing utilizing the Floating Shock Platform. Although the magnitude was greater, the bottom reflection of the Lagrangian solid

bottom model had the same characteristic shape of the clay soil reflection. The first bubble pulse occurred 13 milliseconds sooner with the solid bottom than with the Euler clay soil. Overall, the fluid response of the simulation with a Lagrangian solid bottom was consistent with the Euler bottom modeling method.

One of the distinct advantages of using a Lagrangian solid bottom is the ability to model contoured bottom shapes. Six contoured solid bottom models were developed to investigate bottom contour effects on shallow water UNDEX events. The initial analysis of the FSP response showed only slight differences between the various contour models. This was caused by the buffer created by the bulk cavitation zone. The effect was specific only to the particular geometry selection. Modifications of the charge size, target separation, or bottom depth could diminish the effect, but it was left for future study. Further investigation of the fluid domain response revealed that there were indeed significant differences between the initial bottom reflections for the different contours. The most important bottom contour effect was the distortion to the gas bubble and its associated first pulse timing. These changes could have severe implications in the case of undersea weapons designed to take advantage of ship whipping.

B. FURTHER RESEARCH

While the preprocess required to implement the Lagrangian solid bottom model can be time-intensive, the potential benefits are considerable.

Application of Dyna_N material model types 16, 45, and 65, which were created to model geologic material, to the Lagrangian solid bottom should be investigated. A more accurate soil model could further improve the accuracy of the fluid domain response.

A recent DYSMAS code revision, which was unavailable during this research, allows for the use of viscous fluids. This viscous code was developed in order to more accurately model the ocean bottoms. A comparison of capabilities could be conducted between this new code and the Lagrangian solid bottom model, especially in the case of charges placed close to the sea floor where the effects of cratering are highly likely.

Although it was designed for application in shallow water simulations, the Lagrangian solid bottom model has potential applications in deep water simulations. Currently, all fluid domain simulations in which gravity is present require the application of a reflective bottom boundary condition. In deep water simulations, a sufficient fluid depth is added to the domain in order to minimize the effect of this reflective boundary. Recalling that the behavior of waves at an interface is determined by the ratio of the product of each materials density and sound speed, it could be possible with an elastic material model to create an interface ratio of one. This would allow the wave energy to be completely absorbed into the Lagrangian solid bottom. The use of NRB segments would then allow for the dissipation of the wave. Thus the depth of the fluid could be decreased to only the area of interest around the gas bubble and target. If the material properties could not

be matched, then creating a contoured, anechoic bottom surface could also eliminate the bottom reflection and provide a more accurate deep water solution.

APPENDIX. INDEX OF SIMULATIONS

The following table is an index of the UNDEX simulations that were conducted in the course of this research. The pertinent data for the charge, fluid geometry, FSP position, solid bottom dimensions, and solid bottom boundary and initial conditions are listed for each simulation. For additional simulation input data and results, contact the Shock and Vibration Computational Laboratory at the Naval Postgraduate School.

	Run ID #	1-00	1-01	3-01	3-02	3-03	3-07	3-08	4-01	4-02	4-04	4-07	5-03
	Description	Wall Boundary Condition for Ocean Bottom	Gemini Soil EOS for Ocean Bottom	Long-Time Steady-State Simulation (2.5 secs)	Long-Time Steady-State Simulation w/ Ramped Load	DR of Structural Bottom	DR of Structural Bottom and FSP	Dyna_N Prestress of Structural Bottom	Retransmission of Nodally Constrained Bottom 5m	Retransmission of Nodally Constrained Bottom 10m	Effect of NRB Segments on Retransmission	Effect of NRBs and Nodal Forces on Retransmission	Bottom Contour in Euler (2D) Proof of Concept
	Simulation Time (sec)	1.000	1.000	2.500	2.500	N/A	N/A	0.100	0.100	0.100	0.100	0.100	0.100
Charge	Mass (kg)	27.2	27.2	N/A	N/A	N/A	N/A	27.2	27.2	27.2	27.2	27.2	N/A
	Depth (m)	10.0	10.0	N/A	N/A	N/A	N/A	10.0	10.0	10.0	10.0	10.0	N/A
Fluid Domain Extent	X (m)	84.0	84.0	84.0	84.0	N/A	N/A	84.0	84.0	84.0	84.0	84.0	10.0
	Y (m)	84.0	84.0	84.0	84.0	N/A	N/A	84.0	84.0	84.0	84.0	84.0	N/A
	Z (m)	45.0	50.0	46.0	46.0	N/A	N/A	46.0	46.0	46.0	46.0	46.0	10.0
	Max. Water Depth + Overlap (m)	35.0 + 0.0	35.0 + 5.0*	35.0 + 1.0	35.0 + 1.0	35.0 + 0.0	35.0 + 0.0	35.0 + 1.0	35.0 + 1.0	35.0 + 1.0	35.0 + 1.0	35.0 + 1.0	8.0 + 1.0*
FSP Position	X (m)	853.4	853.4	N/A	N/A	N/A	853.4	N/A	N/A	N/A	N/A	N/A	N/A
	Y (m)	0.0	0.0	N/A	N/A	N/A	0.0	N/A	N/A	N/A	N/A	N/A	N/A
	Z (m)	-121.9	-121.9	N/A	N/A	N/A	-121.9	N/A	N/A	N/A	N/A	N/A	N/A
Solid Bottom Size	X (m)	N/A	N/A	84.00	84.00	84.00	84.00	84.00	84.00	84.00	84.00	84.00	N/A
	Y (m)	N/A	N/A	84.00	84.00	84.00	84.00	84.00	84.00	84.00	84.00	84.00	N/A
	Z (m)	N/A	N/A	5.00	5.00	5.00	5.00	5.00	5.00	10.00	5.00	5.00	N/A
Solid Bottom Boundary Conditions	Interface Segments	N/A	N/A	Yes, Zmax	Yes, Zmax	Yes, Zmax	Yes, Zmax	Yes, Zmax	Yes, Zmax	Yes, Zmax	Yes, Zmax	Yes, Zmax	N/A
	Fixed Nodes	N/A	N/A	Yes, X/Y/Zmin	Yes, X/Y/Zmin	No	Yes, X/Y/Zmin	No	Yes, X/Y/Zmin	Yes, X/Y/Zmin	No	No	N/A
	Reaction Forces	N/A	N/A	No	No	Yes, ANSYS	No	Yes, Manual	No	No	No	Yes, Manual	N/A
	NRB Segments	N/A	N/A	Yes	Yes	No	No	Yes	No	No	Yes	Yes	N/A
	Counter Back Pressure	N/A	N/A	Yes	Yes	Yes	No	No	No	No	No	No	N/A
Solid Bottom Initial Conditions	Dyna_N Prestress	N/A	N/A	No	No	No	No	Yes, Manual	No	No	No	No	N/A

* indicate overlap was actual euler clay material

** indicates average depth, See Table 17 and Figure 38 for more accurate description

	Run ID #	7-01	7-02	7-03	7-04	7-05	7-06	8-01	8-02	8-03	8-04	8-05	8-06
	Description	Contoured Structural Bottom - Deep V	Contoured Structural Bottom - Inverted V	Contoured Structural Bottom - Deep U Channel	Contoured Structural Bottom - Slanted	Contoured Structural Bottom - Anechoic Pyramids	Flat Bottom	Effect of Bottom Thickness w/ Prestress 2m	Effect of Bottom Thickness w/ Prestress 5m	Effect of Bottom Thickness w/ Prestress 10m	Effect of Bottom Thickness w/o Prestress 2m	Effect of Bottom Thickness w/o Prestress 5m	Effect of Bottom Thickness w/o Prestress 10m
	Simulation Time (sec)	1.000	1.000	1.000	1.000	1.000	1.000	0.100	0.100	0.100	0.100	0.100	0.100
Charge	Mass (kg)	27.2	27.2	27.2	27.2	27.2	27.2	27.2	27.2	27.2	27.2	27.2	27.2
	Depth (m)	10.0	10.0	10.0	10.0	10.0	10.0	10.0	10.0	10.0	10.0	10.0	10.0
Fluid Domain Extent	X (m)	84.0	84.0	84.0	84.0	84.0	84.0	84.0	84.0	84.0	84.0	84.0	84.0
	Y (m)	84.0	84.0	84.0	84.0	84.0	84.0	84.0	84.0	84.0	84.0	84.0	84.0
	Z (m)	56.0	56.0	46.0	46.0	41.0	46.0	46.0	46.0	46.0	46.0	46.0	46.0
	Max. Water Depth + Overlap (m)	45.0 + 1.0	45.0 + 1.0	35.0 + 1.0	35.0 + 1.0	40.0 + 1.0	35.0 + 1.0	35.0 + 1.0	35.0 + 1.0	35.0 + 1.0	35.0 + 1.0	35.0 + 1.0	35.0 + 1.0
FSP Position	X (m)	853.4	853.4	853.4	853.4	853.4	853.4	N/A	N/A	N/A	N/A	N/A	N/A
	Y (m)	0.0	0.0	0.0	0.0	0.0	0.0	N/A	N/A	N/A	N/A	N/A	N/A
	Z (m)	-121.9	-121.9	-121.9	-121.9	-121.9	-121.9	N/A	N/A	N/A	N/A	N/A	N/A
Solid Bottom Size	X (m)	84.02	84.02	84.02	84.02	84.00	84.02	84.02	84.02	84.02	84.02	84.02	84.02
	Y (m)	84.02	84.02	84.02	84.02	84.00	84.02	84.02	84.02	84.02	84.02	84.02	84.02
	Z (m)	** 15.00	** 15.00	** 15.00	** 10.00	10.00	5.00	2.00	5.00	10.00	2.00	5.00	10.00
Solid Bottom Boundary Conditions	Interface Segments	Yes, Zmax	Yes, Zmax	Yes, Zmax	Yes, Zmax	Yes, X/Y/Zmax	Yes, Zmax	Yes, Zmax	Yes, Zmax	Yes, Zmax	Yes, Zmax	Yes, Zmax	Yes, Zmax
	Fixed Nodes	No	No	No	No	No	No	No	No	No	No	No	No
	Reaction Forces	Yes, ANSYS	Yes, ANSYS	Yes, ANSYS	Yes, ANSYS	Yes, ANSYS	Yes, ANSYS	Yes, ANSYS	Yes, ANSYS	Yes, ANSYS	Yes, ANSYS	Yes, ANSYS	Yes, ANSYS
	NRB Segments	Yes	Yes	Yes	Yes	Yes	Yes	Yes	Yes	Yes	Yes	Yes	Yes
	Counter Back Pressure	No	No	No	No	No	No	Yes	Yes	Yes	Yes	Yes	Yes
Solid Bottom Initial Conditions	Dyna_N Prestress	Yes, ANSYS	Yes, ANSYS	Yes, ANSYS	Yes, ANSYS	Yes, ANSYS	Yes, ANSYS	Yes, ANSYS	Yes, ANSYS	Yes, ANSYS	No	No	No

* indicate overlap was actual euler clay material

** indicates average depth, See Table 17 and Figure 38 for more accurate description

THIS PAGE INTENTIONALLY LEFT BLANK

LIST OF REFERENCES

[1] A. Arons and D. Yennie, "Energy partition in underwater explosion phenomena," *Reviews of Modern Physics*, vol. 20, no. 3, pp. 519-536, July 1948.

[2] R. H. Cole, *Underwater Explosions*, Princeton: Princeton Press, 1948.

[3] H. G. Snay, "Hydrodynamics of underwater explosions," in *Symposium on Naval Hydrodynamics*, 1957, pp. 325-352.

[4] G. I. Taylor, "The pressure and impulse of submarine explosion waves on plates," in *Aerodynamics and the Mechanics of Projectiles and Explosions*, vol. III, G. Batchelor, Ed., Cambridge, Cambrdige University Press, 1941, pp. 287-303.

[5] Department of the Navy, "Requirements for shock tests, high impact shipboard machinery, equipment and systems," Department of the Navy, MIL-S-901D, 1989.

[6] Naval Sea Systems Command, "Shock design criteria for surface ships," Naval Sea Systems Command, NAVSEA 0908-LP-000-3010A, 1994.

[7] Department of the Navy, "Shock hardening of surface ships," Department of the Navy, OPNAVINST 9072.2, 1987.

[8] R. Ilamni, "Analyses of the Baltic Sea test site UNDEX shock environment," Naval Surface Warfare Center Indian Head, Indian Head, Report IHTR 2785, 2006.

[9] A. B. Wardlaw, R. McKeown and H. Chen, "Implementation and application of the p-alpha equation of state in the DYSMAS code," NSWC Dahlgren, Dahlgren, Report NSWCDD/TR-95/107, 1996.

[10] R. Buxton, "The effects of porous sea bottoms on the propagation of underwater shock waves using the p-alpha equation of state," M.S. thesis, The Pennsylvania State University, State College, 2009.

[11] W. Howey, "Parametric study of LCS-1 shock response resulting from shallow water environment UNDEX," M.S. thesis, Naval Postgraduate School, Monterey, 2011.

[12] H. G. Snay, "Underwater explosion phenomena: the parameters of migrating bubbles," U.S. Naval Ordnance Laboratory, White Oak, NAVORD 4185, 1962.

[13] A. Arons, D. Yennie and T. J. Cotter, "Long range shock propagation in underwater explosion phenomena II," in *Underwater Explosion Research: Volume I – The Shock Wave*, 1949, pp. 1473-1584.

[14] "Naval ship shock design and analysis." Class notes for ME4525, Department of Mechanical and Aerospace Engineering, Naval Postgraduate School, 2004.

[15] B. M. Das, *Principles of Geotechnical Engineering*. Pacific Grove: Brooks/Cole, 2002.

[16] N. Lu, T. H. Kim, S. Sture and W. J. Likos, "Tensile strength of unsaturated sand," in *Journal of Engineering Mechanics ASCE*, vol. 135, pp. 1410-1419, 2009.

[17] A. B. Wardlaw, J. A. Luton, J. R. Renzi, K. C. Kiddy and R. M. McKeown, "The Gemini euler solver for the coupled simulation of underwater explosions," NSWC Indian Head, Indian Head, Report IHTR 2500, 2003.

[18] Naval Surface Warfare Center Indian Head Division, *Gemini: The DYSMAS Eulerian Solve: User's Manual*, Naval Surface Warfare Center, 2010.

[19] J. O. Hallquist, *LS-DYNA Theoretical Manual*, Livermore Software Technology Corporation, 1998.

[20] Naval Surface Warfare Center Indian Head Division, *DYSMAS/P 2010: A Pre- and Postprocessor for DYSMAS/ELC*, Naval Surface Warfare Center, 2010.

[21] G. R. Prendergast, "Underwater explosion whipping response of monohull versus trimaran vessels," Ph.D. dissertation, Naval Postgraduate School, Monterey, 2010.

[22] J. Didoszak, private communication, 06 June 2011.

[23] M. Bangash, *Impact and Explosion: Analysis and Design*, Oxford: CRC Press, 1993.

[24] R. Koltuniuk, private communication, 04 August 2011.

[25] Y. Kwon, private communication, 06 June 2011.

[26] K. O'Shea and R. Koltuniuk, "Structural dynamic analysis of Parker dam with spillway," in *The Role of Dams in the 21st Century*, San Antonio, 2006.

[27] Naval Surface Warfare Center Indian Head Division, *DYNA_N(3D): A Nonlinear, Explicit, Three-Dimensional Finite Element Code for Solid and Structural Mechanics*, Naval Surface Warfare Center, 2009.

[28] S. Zhenxia and D. Haiping, "The analyses of seismic response for base-isolated structure by LS-DYNA," Indian Institute of Technology Kanpur, Available from: http://www.iitk.ac.in/nicee/wcee/artical/14_14-0204.pdf.

[29] W. T. Thomson and M. D. Dahleh, *Theory of Vibration with Applications*, Upper Saddle River: Prentice-Hall, 1998.

[30] R. Ilamni, private communication, 01 August 2011.

[31] R. McKeown, private communication, 02 August 2011.

[32] J. Didoszak and Y. Shin, "Parametric study in the modeling and simulation of fully coupled eulerian-lagrangian fluid structure interaction ship shock problems: floating shock platform," presented at *79th Shock and Vibration Symposium*, Orlando, 2008.

THIS PAGE INTENTIONALLY LEFT BLANK

INITIAL DISTRIBUTION LIST

1. Defense Technical Information Center
   Ft. Belvoir, Virginia

2. Dudley Knox Library
   Naval Postgraduate School
   Monterey, California

3. Mechanical & Aerospace Engineering Department
   Chairman, Code MAE
   Naval Postgraduate School
   Monterey, California

4. Naval/Mechanical Engineering Curriculum Code 74
   Naval Postgraduate School
   Monterey, California

5. Distinguished Professor Young Kwon, Code MAE/Kw
   Department of Mechanical & Aerospace Engineering
   Naval Postgraduate School
   Monterey, California

6. Research Assistant Professor Jarema Didoszak, Code MAE/Di
   Department of Mechanical & Aerospace Engineering
   Naval Postgraduate School
   Monterey, California

7. Director of Science and Technology
   Program Executive Office, Ships
   Washington Navy Yard
   Washington, DC

8. Erica Hansen
   Program Executive Office Ships
   Washington Navy Yard
   Washington, DC

9. Deputy Director, Live Fire Test and Evaluation
   Office of Operational Test and Evaluation
   Washington, DC

10. Thomas Julian
    Office of the Secretary of Defense
    Washington, DC

11. Christopher Moosmann
    Office of the Director of Test and Evaluation
    Washington, DC

12. Clifford Campbell
    ICI Services, LLC
    Washington, DC

13. Gregory S. Harris
    Naval Surface Warfare Center, Indian Head Division
    Indian Head, Maryland

14. Roger Ilamni
    Naval Surface Warfare Center, Indian Head Division
    Indian Head, Maryland

15. Reid McKeown
    Naval Surface Warfare Center, Indian Head Division
    Indian Head, Maryland

16. Frederick A. Costanzo
    Underwater Explosion Research Department (UERD)
    Naval Surface Warfare Center, Carderock Division
    West Bethesda, Maryland

17. Steven Rutgerson
    Underwater Explosion Research Department (UERD)
    Naval Surface Warfare Center, Carderock Division
    West Bethesda, Maryland

18. Barbara Mills-Bria
    Structural Analysis Group (86-68110)
    U.S. Bureau of Reclamation, Technical Service Center
    Denver, Colorado

19. Roman Koltuniuk
    Structural Analysis Group (86-68110)
    U.S. Bureau of Reclamation, Technical Service Center
    Denver, Colorado